

GROWTH AND CHARACTERIZATION OF ZINC OXIDE THIN FILMS FOR LIGHT  
EMITTING DIODES

By

HYUN-SIK KIM

A DISSERTATION PRESENTED TO THE GRADUATE SCHOOL  
OF THE UNIVERSITY OF FLORIDA IN PARTIAL FULFILLMENT  
OF THE REQUIREMENTS FOR THE DEGREE OF  
DOCTOR OF PHILOSOPHY

UNIVERSITY OF FLORIDA

2008

© 2008 Hyun-Sik Kim

To our LORD, Jesus Christ

## ACKNOWLEDGMENTS

I would like first to express my sincere appreciation to my advisor, Dr. David P. Norton for his invaluable guidance and support. It would be impossible to give enough thank to him. He is a role model both academically and personally. I would also like to thank my committee members, Dr. Stephen J. Pearton, Dr. Fan Ren, and Dr. Cammy R. Abernathy for their advice on my research.

I would like to express my great thanks to all my colleagues in Dr. Norton's group, Dr. Mat Ivill, Dr. George Erie, Dr. Yuanjie Li, Dr. Seemant Rawal, Dr. Li-Chia Tien, Patrick Sadik, Daniel Leu, Charlee Callender, Ryan Pate, Fernando Lugo, Joe Cianfrone, Seon-Hoo Kim, and Kyeong-Won Kim. I feel fortunate to work with them. I am especially grateful to my collaborators in Dr. Ren's group including Dr. Jau-Jiun Chen, Dr. Hung-Ta Wang, and Yu-Lin Wang. They were willing to help me in fabricating LED devices. I would have never finished my research projects without them.

I appreciate my Korean church community and pastors, Joong-Soo Lee, Hee-Young Sohn, Min-Seok Sohn, and Byeong-Ok Kim. They guided me to Jesus Christ more closely.

I would like to express my deepest appreciation and love to my parents for their infinite love. They have visualized God's unconditional love to me.

I thank my fiancé, Dr. May Kim, for her immeasurable love and support. She was always with me and encouraged me. I always found God's wisdom and love inside her.

Finally, I deeply thank and praise to my Lord, Jesus Christ.

## TABLE OF CONTENTS

	<u>page</u>
ACKNOWLEDGMENTS .....	4
LIST OF TABLES .....	7
LIST OF FIGURES .....	8
ABSTRACT .....	12
1 INTRODUCTION .....	14
1.1 Motivation for ZnO-Based LEDs .....	14
1.2 Objectives .....	15
2 LITERATURE RIVIEW .....	17
2.1 General Properties of ZnO .....	17
2.2 Doping of ZnO .....	17
2.2.1 Intrinsic Defects .....	18
2.2.2 N-type Doping .....	18
2.2.3 P-type Doping .....	19
Nitrogen doping .....	20
Phosphorus doping .....	21
Other dopants .....	21
2.2.4 Persistent Photoconductivity and Surface Passivation .....	22
Persistent photoconductivity .....	22
Surface passivation .....	24
2.3 ZnO Based Ternary Alloys .....	25
2.4 ZnO Based Light Emitting Diodes .....	25
3 EXPERIMENTAL TECHNIQUES .....	33
3.1 Growth Technique .....	33
3.2 Analytical Techniques .....	34
3.2.1 X-Ray Diffraction (XRD) .....	34
3.2.2 X-Ray Photoelectron Spectroscopy (XPS) .....	35
3.2.3 Atomic Force Microscopy (AFM) .....	36
3.2.4 Hall Effect Measurement .....	36
3.2.5 Photoluminescence (PL) .....	37
4 ZINC OXIDE THIN FILMS GROWN WITH O <sub>2</sub> /O <sub>3</sub> MIXTURE GAS .....	42
4.1 Introduction .....	42
4.2 Experimental .....	43
4.3 Results and Discussion .....	44

4.3.1 Electrical and Optical Properties of ZnO Thin Films Grown with O <sub>2</sub> /O <sub>3</sub> Gas Mixture.....	44
4.3.2 Post-Annealed ZnO Thin Films Grown with O <sub>3</sub> .....	47
4.4 Summary.....	50
5 ZINC OXIDE THIN FILMS GROWN WITH ZnO HOMO-BUFFER LAYER.....	61
5.1 Introduction.....	61
5.2 Experimental.....	62
5.3 Results and Discussion.....	63
5.3.1 Effects of Buffer Growth Parameters on the Properties of Heteroepitaxial ZnO Films.....	63
5.3.2 High Quality ZnO Films Using a High Temperature Deposited ZnO Buffer Layer.....	65
5.4 Summary.....	68
6 PHOSPHORUS DOPED ZnO AND ZnMgO THIN FILMS.....	81
6.1 Introduction.....	81
6.2 Experimental.....	83
6.2.1 Phosphorus Doped ZnO.....	83
6.2.2 Phosphorus Doped Zn <sub>1-x</sub> Mg <sub>x</sub> O.....	84
6.3 Results and Discussion.....	84
6.3.1 Behavior of Rapid Thermal Annealed ZnO:P films.....	84
6.3.2 Dependence of Zn <sub>1-x</sub> Mg <sub>x</sub> O:P Film Properties on Magnesium Concentration.....	92
6.4 Summary.....	96
7 ZINC OXIDE LIGHT EMITTING DIODES.....	112
7.1 Introduction.....	112
7.2 Experimental.....	112
7.3 Results and Discussion.....	114
7.4 Summary.....	115
8 CONCLUSION.....	121
8.1 Undoped ZnO Thin Films.....	121
8.2 Phosphorus Doped ZnO and ZnMgO.....	123
8.3 ZnO Based LEDs.....	124
LIST OF REFERENCES.....	125
BIOGRAPHICAL SKETCH.....	136

## LIST OF TABLES

<u>Table</u>		<u>page</u>
2-1	Valence and ionic radii of candidate p-type dopant atoms.....	28
5-1	Hall data of ZnO films grown with and without a high temperature deposited ZnO buffer layer.....	69
6-1	Hall data of 0.5% P-doped films grown at various temperatures and subjected to various post-annealing temperatures.....	98
6-2	Hall data of 1.0% P-doped films grown at various temperatures and subjected to various post-annealing temperatures.....	99
7-1	Resistivity for P-doped ZnO thin films before and after wet etching.....	116

## LIST OF FIGURES

<u>Figure</u>	<u>page</u>
2-1 Crystal structure of wurtzitic ZnO.....	29
2-2 Bandgap versus lattice constant of various semiconductors.....	29
2-3 Zinc oxide homostructural p-i-n junction A) Current-voltage characteristics B) Electroluminescence spectrum [8].....	30
2-4 Comparison of EL spectra of the <i>p-n</i> homojunction ZnO LED and the ZnO LED with Mg <sub>0.1</sub> Zn <sub>0.9</sub> O layers, operated at a forward current of 40 mA [11].....	31
2-5 The p-n junction ZnO-based LED A) current-voltage (I-V) characteristics B) EL spectrum of ZnO pn junction having a BeZnO active layer measured at room temperature [10].....	32
3-1 Pulsed-laser deposition system.....	39
3-2 Philips X'pert high resolution diffractometer using 4-circle goniometer.....	40
3-3 Optical detection mechanism in AFM.....	41
3-4 Radiative recombination mechanisms.....	41
4-1 Carrier density of ZnO films grown with pure O <sub>2</sub> and O <sub>2</sub> /O <sub>3</sub> mixture gas at various pressures.....	52
4-2 Ratio of donor defect density of the ZnO films grown with O <sub>2</sub> and O <sub>2</sub> /O <sub>3</sub> .....	52
4-3 Mobility of ZnO films grown with pure O <sub>2</sub> and O <sub>2</sub> /O <sub>3</sub> mixture gas at various pressures.....	53
4-4 Room-temperature PL spectra of ZnO films A) grown with pure O <sub>2</sub> and B) O <sub>2</sub> /O <sub>3</sub> mixture gas.....	54
4-5 Intensity of bandedge emission of ZnO films grown with pure O <sub>2</sub> and O <sub>2</sub> /O <sub>3</sub> mixture gas at various pressures.....	55
4-6 X-ray diffraction omega rocking curves for ZnO films grown with A) pure O <sub>2</sub> B) O <sub>2</sub> /O <sub>3</sub> mixture gas.....	56
4-7 Atomic force microscopy images for annealed ZnO films grown with A) pure O <sub>2</sub> B) O <sub>2</sub> /O <sub>3</sub> mixture gas.....	57
4-8 Carrier density of ZnO films grown with A) pure O <sub>2</sub> B) O <sub>2</sub> /O <sub>3</sub> mixture gas as a function of the annealing temperature.....	58

4-9	Mobility of ZnO films grown with A) pure O <sub>2</sub> B) O <sub>2</sub> /O <sub>3</sub> mixture gas as a function of the annealing temperature. ....	58
4-10	Room temperature PL spectra of ZnO films grown with A) pure O <sub>2</sub> B) O <sub>2</sub> /O <sub>3</sub> mixture gas as a function of the annealing temperature. ....	59
4-11	The intensity of bandedge emission of ZnO films grown with A) pure O <sub>2</sub> B) O <sub>2</sub> /O <sub>3</sub> mixture gas as a function of the annealing temperature. ....	60
5-1	Atomic force microscopy image of a 1 μm thick ZnO films grown on (0001) sapphire at 850°C and 10 mTorr without the use of a nucleating buffer layer. The scanned image size is 10 x 10 μm <sup>2</sup> .....	70
5-2	Atomic force microscopy image of 1 μm thick ZnO films deposited on (0001) sapphire at 850°C and 10 mTorr in which a nucleating ZnO buffer layer deposited in 1 mTorr O <sub>2</sub> /O <sub>3</sub> was employed with different buffer growth temperatures. The scanned image size is 10 x 10 μm <sup>2</sup> .....	70
5-3	Atomic force microscopy image of 1 μm thick ZnO films deposited on (0001) sapphire at 850°C and 10 mTorr in which a nucleating ZnO buffer layer deposited at 850°C was employed with different buffer growth O <sub>2</sub> /O <sub>3</sub> pressures. The scanned image size is 10 x 10 μm <sup>2</sup> . ....	71
5-4	RMS roughness of 1 μm thick ZnO films grown A) at 1 mTorr with different buffer growth temperatures or B) at 850°C with different buffer growth pressures.....	72
5-5	FWHM of ω-rocking curves of the ZnO (002) of 1 μm thick ZnO films grown A) at 1 mTorr with different buffer growth temperatures or B) at 850°C with different buffer growth pressures.....	73
5-6	Plots of A) carrier concentration and B) mobility for 1 μm thick ZnO films deposited on (0001) sapphire at 850°C and 10 mTorr in which a nucleating ZnO buffer layer deposited at 850°C was employed with different buffer growth O <sub>2</sub> /O <sub>3</sub> pressures. ....	74
5-7	Plots of A) carrier concentration and B) mobility for 1 μm thick ZnO films deposited on (0001) sapphire at 850°C and 10 mTorr in which a nucleating ZnO buffer layer deposited in 1 mTorr O <sub>2</sub> /O <sub>3</sub> was employed with different buffer growth temperatures.....	75
5-8	XRD ω-rocking curves of ZnO (002) grown A) with and B) without a high temperature deposited ZnO buffer. ....	76
5-9	XRD phi scan of ZnO (102) grown A) with and B) without a high temperature deposited ZnO buffer. ....	77
5-10	XRD ω-rocking curves of ZnO (102) grown A) with and B) without a high temperature deposited ZnO buffer. ....	78

5-11	PL spectra of ZnO films grown A) with and B) without a high temperature deposited ZnO buffer at room temperature. ....	79
5-12	AFM images of ZnO films grown A) with and B) without a high temperature deposited ZnO buffer in $5 \times 5 \text{ um}^2$ .....	80
6-1	X-ray diffraction omega rocking curves for A) undoped, B) 0.5 at.% P-doped, and C) 1.0 at.% doped ZnO films grown by pulsed laser deposition. Growth conditions were 700°C and 150 mTorr oxygen. ....	100
6-2	Hall data for as-deposited ZnO:P films, showing A) resistivity and B) carrier density. All films in this figure are n-type.....	101
6-3	Low temperature photoluminescence (PL) for a ZnO:P film showing an acceptor-associated peak at 3.313 eV. ....	102
6-4	Atomic force microscopy images for 0.5 at.% P-doped ZnO films grown at different substrate temperatures.....	102
6-5	Hall data for rapid thermal annealed ZnO films doped with 0.5 at.% P, grown at 700°C, showing A) resistivity and B) carrier density as a function of annealing temperature. Most films in this figure were n-type.....	103
6-6	Hall data for rapid thermal annealed ZnO films doped with 0.5 and 1.0 at.% P, grown at 700°C, 150 mTorr oxygen, showing A) resistivity and B) carrier density as a function of annealing temperature. ....	104
6-7	Plot of van der Pauw Hall voltage differences for a p-type 0.5 at.% P-doped ZnO film subjected to a 900°C RTA process. The voltage difference polarity for all measurements are consistent with p-type conduction.....	105
6-8	Room temperature photoluminescence data for A) 1.0 at.% and B) 0.5 at.% P-doped ZnO films that were post-annealed and p-type. ....	106
6-9	XRD spectra of as-grown ZnMgO:P films that contains 5 A) and 10 B) at. % of Mg....	107
6-10	Carrier concentration A) and resistivity B) of as-grown ZnMgO:P <sub>0.2</sub> films grown with different growth temperatures.....	108
6-11	PL spectra for as-grown ZnMgO:P <sub>0.2</sub> films that contains 5 A) and 10 B) at. % of Mg...109	109
6-12	Carrier concentration A) and resistivity B) of ZnMgO:P <sub>0.2</sub> films with the annealing temperature. ....	110
6-13	PL spectra for annealed ZnMgO:P <sub>0.2</sub> films that contains 5 A) and 10 B) at. % of Mg. ...111	111

7-1	I-V characteristics for a ZnO:P/Zn <sub>0.9</sub> Mg <sub>0.1</sub> O/ZnO/Zn <sub>0.9</sub> Mg <sub>0.1</sub> O/ZnO:Ga heterojunction diode both as-fabricated and after a 350°C anneal. Also show in the inset is a schematic of the device structure.....	117
7-2	Secondary ion mass spectrometry composition depth profile taken for a ZnMgO:P/ZnO multilayer both A) without and B) with a post-growth anneal. ....	118
7-3	Plot of A) light intensity and voltage as a function of drive current for an annealed ZnO:P/Zn <sub>0.9</sub> Mg <sub>0.1</sub> O/ZnO/Zn <sub>0.9</sub> Mg <sub>0.1</sub> O/ZnO:Ga heterojunction diode. Also shown B) is the spectra for the diode at two different bias voltages.....	119
7-4	Room temperature optical spectra of a ZnO:P/Zn <sub>0.9</sub> Mg <sub>0.1</sub> O/ZnO/Zn <sub>0.9</sub> Mg <sub>0.1</sub> O/ZnO:Ga heterojunction diode for A) electroluminescence and B) photoluminescence. ....	120

Abstract of Dissertation Presented to the Graduate School  
of the University of Florida in Partial Fulfillment of the  
Requirements for the Degree of Doctor of Philosophy

GROWTH AND CHARACTERIZATION OF ZINC OXIDE THIN FILMS FOR LIGHT  
EMITTING DIODES

By

Hyun-Sik Kim

May 2008

Chair: David P. Norton

Major: Materials Science and Engineering

ZnO and ZnMgO thin films were grown by pulsed laser deposition for light emitting diodes. Phosphorus was used as the dopant to achieve p-type conductivity in these films. The electrical and optical properties of ZnO thin films grown with O<sub>2</sub> /O<sub>3</sub> gas mixture are compared with samples grown with pure oxygen gas. The residual background carrier concentration is reduced by using a O<sub>2</sub> /O<sub>3</sub> gas mixture as compared to pure molecular oxygen. The lower donor defect density is attributed to the generation of acceptor defects compensating the residual donor defects. Also, annealing studies were performed on ZnO films grown by using either O<sub>2</sub> and an O<sub>2</sub>/O<sub>3</sub> gas mixture as the oxidant. The results confirmed the existence of acceptor states created via growth in ozone. The acceptor states are annihilated with post-annealing. This suggests that the ozone-related acceptor states are metastable.

Effects of buffer layer deposition conditions on subsequent ZnO epitaxy on sapphire (0001) were examined. An initial ZnO buffer layer improves surface roughness for a wide range of buffer layer growth temperatures and pressures. The conditions for buffer layer deposition have a large impact on crystallinity of subsequent films. High quality ZnO film growth on sapphire was achieved by using a high temperature deposited ZnO buffer layer. This high temperature deposited buffer layer remarkably improves crystallinity of subsequent films. In particular, the

full width at half maximum of X-ray diffraction  $\omega$ -rocking curves for ZnO films grown with the buffer is  $0.0076^\circ$  (27.36 arcsec) and  $0.1242^\circ$  (447.12 arcsec) for the out-of-plane (002) and in-plane (102), respectively.

The transport properties of as-deposited and rapid thermal annealed phosphorus-doped ZnO films are reported. As-grown ZnO:P samples showed n-type characteristics, presumably due to the formation of anti-site  $P_{Zn}$  defects. Rapid thermal annealing yielded a carrier type conversion from n- to p-type for the ZnO:P films grown at  $\sim 700^\circ\text{C}$ . The properties and behavior of the n-to-p conversion is most consistent with the formation of  $P_{Zn}-2V_{Zn}$  as the active acceptor state. The dependence of p-type conversion on Mg content in  $Zn_{1-x}Mg_xO:P$  films ( $x = 0.1, 0.05$ ) is examined. P-type  $Zn_{1-x}Mg_xO:P$  films were successfully achieved without post thermal annealing treatments for a Mg content of  $x = 0.10$ . Increasing magnesium content in the ZnMgO:P solid solution generally degrades the luminescence properties, suggesting the formation of non-radiative states.

ZnO-based light emitting diodes were fabricated on c-plane sapphire using ZnO:P/ $Zn_{0.9}Mg_{0.1}O/ZnO/Zn_{0.9}Mg_{0.1}O/ZnO:Ga$  p-i-n heterostructures. The p-i-n heterojunction diodes are rectifying and show light emission under forward bias. The electroluminescence spectra shows deep level emission at low bias, but near band edge ultraviolet emission at high voltage bias. A decrease in leakage currents in as-fabricated structures was achieved via low temperature oxygen annealing.

## CHAPTER 1 INTRODUCTION

### 1.1 Motivation for ZnO-Based LEDs

Light emitting diodes (LEDs) have numerous applications. Examples include traffic signals, displays, backlighting in the electronic displays, automobile brake lights, indicators on electronic devices, UV bio-detectors, and general lighting applications Solid-State Lighting(SSL). White-light SSL sources will eventually replace traditional incandescent and fluorescent lamps in many general illumination applications due to their higher power efficiencies compared to traditional incandescent sources. This could generate substantial energy savings. LEDs also do not generate heat which makes them preferable in medical use for surgical lighting.

Until now, the III-V compound semiconductor systems have dominated LED applications. GaN is the most widely utilized wide bandgap semiconductor in industry. However, ZnO has a number of advantages over GaN, and thus it is considered as an alternative to traditional III-V based materials for next-generation short wavelength optoelectronic devices. ZnO has several important properties that make it a promising semiconductor material for optoelectronic devices and applications. The following features of ZnO make it a very good replacement for GaN.

- A large exciton binding energy of 60 meV, compared with 26 meV for GaN [1]. This large exciton binding energy provides more efficient exciton emission at room temperature and elevated temperature.
- Exceptional resistant to radiation damage by high energy radiation [2]. High-energy radiation in semiconductors creates deep centers within the forbidden energy gap. These affect device sensitivity, response time, and read-out noise. Therefore, radiation hardness is very important as a device parameter for operation in harsh environments. From this point of view, ZnO is more suitable for space operation than other wide bandgap semiconductors.
- Large and high quality single-crystal wafers are commercially available. It is possible to grow homo-epitaxial ZnO-based devices that have low dislocation densities. Homo-epitaxial ZnO growth on ZnO substrates will alleviate many problems associated with

hetero-epitaxial GaN growth on sapphire, such as stress and thermal expansion problems due to the lattice mismatch.

- Wet chemical etching is possible. It provides many advantages in device processing for ultraviolet(UV) detectors, LEDs, laser diodes, field-effect transistors(FETs), and other optoelectronic devices.
- A tunable bandgap can be realized by alloying ZnO with CdO, MgO, or BeO [3-6]
- The bandgap can be changed from 3 to 4.0 eV in  $Zn_{1-x}Cd_xO$  and  $Mg_xZn_{1-x}O$  alloy films with a small change in lattice spacing [3-5]. This advantage makes it possible to realize strain-free and high quality multiple quantum well (MQW) device structures.
- A very high breakdown electric field of  $\sim 2 \times 10^6$  V/cm, which is about two times higher than the GaAs breakdown field. High operation voltage could be applied to ZnO-based devices for high power and gain.
- A large saturation velocity of  $3.2 \times 10^7$  cm/sec at room temperature. This makes ZnO-based devices better for high frequency applications.

## 1.2 Objectives

ZnO has attracted much attention for optoelectronic devices due to its direct wide bandgap of 3.37 eV at room temperature and high exciton binding energy of 60 meV. Furthermore, ZnO can form ternary solid solutions of CdZnO and MgZnO that have the same wurtzite structure as ZnO. This allows one to vary the bandgap from  $\sim 3$  to 4 eV before phase separation occurs while maintaining the same wurtzite structure as ZnO [3-5]. This makes possible the development of double heterojunction structures for injection lasers and light emitting diodes. However, the difficulty of getting robust p-type due to asymmetric doping characteristics has hindered the making of pn junction device [7]. Thus, p-type ZnO has been an issue for several years.

Recently, there have been several reports about electroluminescence (EL) emission from ZnO based LEDs [8-11]. However, the bandedge EL emission was not sufficiently strong for practical ZnO LED application. The reason for this problem is the absence of high quality and reliable p-type ZnO. There are several possible dopants, such as group-I (Li, Na, and K) and group V (N, P, and As) elements, for p-type doping. Until now it is unclear which dopant is the best for p-type

even though theoretically nitrogen is the most promising candidate [12]. In resolving these issues and realizing ZnO based LEDs, the growth of high quality ZnO film is the basic step prior to doping experiments. The residual donor defects in ZnO compensate the acceptor dopants and prevent stable p-type ZnO. Therefore decreasing background native donor density and getting high quality films are essential to getting robust p-type material. Also, high quality undoped ZnO can be used as an active layer between p- and n-type ZnO to improve emission. Controlling the residual donor density in high quality ZnO films is described. This study mainly focused on achieving reliable and robust p-type ZnO:P and ZnMgO:P films. In addition, it addressed the fabrication of heterostructural p-i-n junction devices.

## CHAPTER 2 LITERATURE RIVIEW

### 2. 1 General Properties of ZnO

ZnO is generally crystallized in the hexagonal wurtzite structure (Figure 2-1) although metastable zinblende and rocksalt structures can be observed when it is grown on cubic substrate or at the high pressure. In this wurtzite structure, each Zn cation is surrounded by four O anions, and vice versa. This yields a tetrahedral coordination. The lattice parameters of wurtzite ZnO are  $a=3.2495 \text{ \AA}$  and  $c=5.2069 \text{ \AA}$  [13]. These values can vary slightly with stoichiometry deviation. The ionic radii are  $0.60 \text{ \AA}$  and  $1.38 \text{ \AA}$  for  $\text{Zn}^{2+}$  and  $\text{O}^{2-}$ , respectively. The distance of the Zn-O bond is  $1.972 \text{ \AA}$ . As-grown undoped ZnO films typically shows non-stoichiometry and are usually n-type. The Hall mobility of ZnO single crystal is about  $100 \sim 200 \text{ cm}^2/\text{V}\cdot\text{s}$ .

The most characteristics of ZnO are optical and electrical properties. The high exciton binding energy provides a path to making exciton devices which can operate at or above the room temperature.

### 2. 2 Doping of ZnO

In order to realize ZnO based LEDs, it is necessary to synthesize both high-quality n- and p-type films. The n-type ZnO is easily achieved even without any doping. It is also easy to get high-quality n-type ZnO by intentionally doping III elements (Al, Ga, and In). In contrast, achieving p-type ZnO is difficult due to the self-compensation effect from residual donors. However, recently several groups have reported p-type ZnO doped with nitrogen, phosphorus, or arsenic. The formation of ZnO based light emitting diodes is also reported [8-11]. Even though these reports on ZnO homojunctions open a door for applications of ZnO material for light emitting diodes and lasers, research is still at an early stage. There remain obstacles to realizing

ZnO based optical devices. In particular, the stability of p-type conduction and the choice of the optimal dopant are still controversial. As a result, reliable and reproducible p-type doping is the most significant impediment to realizing practical applications of electronic and photonic devices based on ZnO materials.

### **2.2.1 Intrinsic Defects**

In order to achieve desired electrical properties in ZnO, an understanding of intrinsic defects is needed. ZnO is normally n-type due to dominant residual donors [14,15]. There are several native defects in ZnO material, namely vacancies ( $V_o$  and  $V_{zn}$ ), interstitials ( $Zn_i$  and  $O_i$ ), and antisites ( $Zn_o$  and  $O_{zn}$ ). The formation energy of these defects determining the defect concentration is strongly dependent on the growth conditions. Theoretical studies have predicted the formation energies of each point defect by using pseudopotential first-principle calculation [16, 17]. In Zn-rich conditions, oxygen vacancies are abundant; zinc vacancies are dominant in O-rich conditions.

D.C. Look *et al.* suggested that  $Zn_i$  rather than  $V_o$  is a dominant shallow donor in ZnO [18]. However, the origin of shallow donors in undoped ZnO is still a controversial issue even though it is often assumed that oxygen vacancies and zinc interstitials contribute to the n-type conductivity. In addition to these intrinsic defects, hydrogen has been suggested as another source of donors [19, 20]. It is difficult to prevent the incorporation of hydrogen during the growth. Hydrogen forms an OH bonding with oxygen atom and always plays the role of a shallow donor in ZnO [17].

### **2.2.2 N-type Doping**

ZnO shows naturally n-type due to residual donors. It is possible to get electron concentrations of  $10^{21}/\text{cm}^3$  even without extrinsic doping [21]. Group-III elements (Al, Ga, and In) and group-VII elements (Cl and F) can be used as controllable n-type dopants by substituting

Zn sites and O sites, respectively. Ko *et al.* reported Ga-doped ZnO by using GaN templates [23]. Miyazaki *et al.* obtained highly conductive and transparent Ga-doped ZnO films [24]. Also, highly conductive Al-doped ZnO films were successfully achieved with photo-assisted MOCVE technique [25]. The transparent and highly conductive n-type ZnO films can be used for transparent conducting oxides (TCO) in display application fields.

### 2.2.3 P-type Doping

Several dopants have been suggested and explored for achieving p-type conduction in ZnO. These include the group-I (Li, Na, and K), group-V (N, P, Sb, and As) and group-IB (Cu and Ag) elements. Some groups theoretically predict group-V elements, such as As, P, and Sb, to form deep acceptors rather than shallow levels, making it difficult to realize p-type conduction using these elements [26, 27]. Furthermore, it is difficult for these elements to substitute on the oxygen site and yield p-type behavior because of their large-size-mismatch with oxygen [Table 1]. In theory, group-I elements should be better p-type dopants than group-V based on atomic size and predicted acceptor state energies [28]. However, group-I elements tend to occupy the interstitial sites due to their small atomic radii rather than substitutional sites, and therefore act mainly as donors [29]. Furthermore, significantly larger bond length for Na and K than ideal Zn-O bond length (1.93 Å) induces lattice strain forming native defects and compensating acceptors [30]. Therefore, it has been believed that the most promising dopants for p-type ZnO are the group-V elements, although theory suggests some difficulty in achieving shallow acceptor levels [26]. Both P and As also have significantly larger bond lengths and therefore are more likely to form antisites to avoid the lattice strain. These antisite atoms play a role of donor compensating acceptors [28]. Due to the above reasons, attaining p-type doping in ZnO is still controversial even though several groups have reported the fabrication of ZnO p-n junctions by various means such as pulsed laser deposition, molecular beam epitaxy, excimer-laser doping, and sputtering.

## Nitrogen doping

Nitrogen has been considered as a most attractive candidate for acceptor doping for making p-type ZnO. The ionic radius of N is similar to that of O. Theoretically it is the best shallow acceptor dopant based on electronic band structure calculation [28, 31]. Therefore, a number of groups have focused on nitrogen with various nitrogen sources including N<sub>2</sub>, NO, N<sub>2</sub>O, NH<sub>3</sub>, and Zn<sub>3</sub>N<sub>2</sub>, depending on the growth technique [32-38]. However, the equilibrium solubility of N is expected to be low [39]. In order to increase the N solubility, the codoping method using acceptors and reactive donors (Al, Ga, and In) simultaneously has been applied [40-43]. High temperature or plasma techniques also have been used to assist N doping and activation [44, 45]. Due to these efforts, there are many reports for p-type ZnO doped with nitrogen. Look *et al.* achieved N-doped p-type ZnO on Li-diffused semi-insulating ZnO substrates by dissociating N<sub>2</sub> with RF plasma source [45]. Minegishi *et al.* obtained p-type ZnO by using NH<sub>3</sub> as a nitrogen doping source [46]. Ashrafi *et al.* achieved p-type conductivity with nitrogen and indicated the correlation of hydrogen to p-type achievement [47]. Lu *et al.* investigated the effect of NH<sub>3</sub>/O<sub>2</sub> ratio for p-type doping with sputter deposition and obtained p-type conductivity at 25% ammonia concentration [48]. Guo *et al.* obtained p-type ZnO having  $3 - 6 \times 10^{18} \text{ cm}^{-3}$  hole concentration by using an N<sub>2</sub>O plasma [49]. Li *et al.* used NO gas as a nitrogen source and achieved p-type doping without thermal or plasma treatment [50, 51]. Lin *et al.* achieved p-type ZnO by N-ion implantation method with ZnO films grown on Si substrates [52].

In order to enhance N incorporation, many researchers have used codoping technique [53-56]. Joseph *et al.* obtained  $5 \times 10^{19} \text{ cm}^{-3}$  hole concentrations by using N<sub>2</sub>O plasma and Ga codoping [41]. Indium and aluminum were also used for codoping elements [57, 58]. Despite

these achievements, however, the reliability in obtaining p-type ZnO doped with nitrogen is still less than optimal.

### **Phosphorus doping**

Theoretical calculation based on the density function theory suggested that phosphorus and arsenic yield deep acceptor levels. Hence, achieving p-type ZnO via phosphorus is perceived difficult [26, 27]. However, contrary to the theoretical prediction, there are several reports on p-type ZnO:P films [59, 60]. Kim *et al.* reported p-type conversion of phosphorus doped n-type ZnO films via rapid thermal annealing [59]. Aoki *et al.* irradiated  $Zn_3P_2$  films on ZnO by excimer laser, with the decomposed P atoms diffusing into the ZnO films [61]. Lee *et al.* also reported p-type ZnO by using laser annealing and a  $Zn_3P_2$  phosphorus source [62]. However, the p-type doping mechanism of phosphorus is still not clear even though p-type ZnO:P was achieved experimentally. Theoretically, P anions tend to occupy anti-site rather than oxygen sites in order to decrease lattice strain. These anti-site defects should play the role of acceptor-compensating donors [63, 64]. However, a  $P_{Zn}-2V_{Zn}$  complex has a shallow acceptor level. As a result, P anions may act as acceptors, not through substitution on the oxygen site, but by forming a P antisite and zinc vacancy complex (e.g.  $P_{Zn}-2V_{Zn}$ ).

### **Other dopants**

Arsenic (As) and antimony (Sb) can also be used as p-type dopants. Ryu *et al.* reported p-type ZnO by use of arsenic as the dopant element [65, 66]. There have also been recent reports of p-type doping using As implantation at low temperatures, followed by multiple step annealing [67]. Xiu *et al.* successfully obtained p-type ZnO by using Sb as a p-type dopant source [68].

Group I (Li, Na, and K) and IB (Cu, Ag, and Au) elements can play the role of acceptors in ZnO materials by substituting Zn sites. However, group I elements mostly occupy interstitial sites rather than substitutional sites and it is difficult to realize p-type conduction [29]. Recently,

Yan *et al.* suggested group IB as a p-type dopant using first principle calculations [69]. Kang *et al.* succeeded in getting p-type conductivity in ZnO with Ag as a p-type dopant [70]. However, the most promising p-type doping has been achieved via group V elements.

#### **2.2.4 Persistent Photoconductivity and Surface Passivation**

##### **Persistent photoconductivity**

Persistent photoconductivity (PPC) is an important issue for ZnO based optoelectronic devices. PPC is mainly due to 1) strong potential fluctuation separating electrons and holes and 2) high barrier centers capturing electron or holes [71-74].

Photogenerated electron-hole pairs are the main source of photoconductivity. In addition to this, photodesorption and adsorption of oxygen molecules on the surface and the grain boundaries also cause changes in conductivity [75-78]. In the absence of optical excitation, adsorption of oxygen on the surface occurs. It creates a depletion layer near the surface by capturing an electron from the conduction band [79]. As a result, the conductivity of the film decreases. Under UV irradiation, photogenerated holes near the surface discharge the negatively charged oxygen ions. This increases the conductivity of the film. The surface related process is significantly slower than the direct photoconduction response by electron-hole pair generation [77, 80, 81]. Tudose *et al.* reported on the relevance between surface morphology and photoconductivity [76]. Mridha *et al.* observed very slow decay processes in ZnO that can be attributed to the surface effects such as adsorption and desorption of oxygen [81]. Moazzami *et al.* suggested that hole traps in ZnO determine the photoconductive characteristics [82].

Photoconductivity is strongly determined by the presence of a high number of trap and defect levels in both the bulk and the surface of the material [83, 84]. If the probability of electron capture is greater than the probability of recombination, persistent photoconductivity

occurs [85]. In many cases, PCC is attributed to the metastable deep unknown (DX) center [83, 84].

A lattice relaxation process of surface states located within the bandgap induces the persistent photoconductivity [27]. Seghier *et al.* observed the persistent photoconductivity in ZnO materials which can be due to the strongly metastable deep defects [86]. Studenikin *et al.* explained the PPC as the capture of nonequilibrium holes by surface oxygen states [80]. This leaves an equivalent number of excess electrons in the conduction band. Transition of electrons to the oxygen surface states gives rise to PPC. Zhang *et al.* explained the PPC in ZnO by a charge neutral  $V_O$  capturing two holes due to its negative potential energy [27]. Lany *et al.* also suggested that PPC originates from a metastable oxygen vacancy in n-ZnO [84].

PPC is an important challenging topic to be understood because its n-type conductivity is an obstacle in realizing robust p-type ZnO materials. Claflin *et al.* observed that there is a persistent n-type photoconductivity in p-type ZnO and reported a significant influence of UV illumination on the p-type conductivity of ZnO films [87]. PPC effects were investigated in ZnO:N films grown by molecular beam epitaxy [88]. P-type samples show a strong PPC that masks the true dark conductivity, and thus the films often render n-type conductivity. Zeng *et al.* compared UV photoconductivity of p-type ZnO:N films and n-type ZnO epilayer [89]. P-type ZnO showed more significant non-equilibrium carrier effects on photoconductivity due to the deeper acceptor level. They claimed that surface adsorption of C and O in ZnO:N film resulting from the small crystalline grain with dense grain boundary on the surface is a major contribution to the UV photoconductivity. Yan *et al.* investigated photoconductivity of In-N codoped p-type ZnO films and found that P-type ZnO film is very sensitive to the UV illumination. Photo-induced conductivity is about 600 times larger than that in the dark [90]. Porter *et al.* also studied

nitrogen and tellurium co-doped ZnO films [91]. The photosensitivity of the films was enhanced and the resistivity increased by co-doping with tellurium and nitrogen.

There are several reports on the PPC of photoconductivity of phosphorus doped ZnO and ZnMgO. Heo *et al.* reported the enhancement of the UV photoconductivity in the P-doped ZnO annealed films [92]. Polyakov *et al.* suggested that the off-center P atoms on Zn sites are the origin of PPC [93]. These off-center P atoms form P-V<sub>Zn</sub> complexes to alleviate the lattice strain. The complex creates deep centers. Ghosh *et al.* investigated the correlation between the photoconductivity and microstructure with various Mg content [94].

### **Surface passivation**

The ZnO surface properties are sensitive to ambient and thus it has been used as a gas sensor. In most device applications, however, adsorption of unwanted impurities deteriorates device stability. In particular, hydrogen in ZnO is a shallow donor compensating acceptors and easily incorporated into ZnO [19, 95, 96]. Also, hydrogen could form conducting layers on the surface, coming either from the ambient or from the bulk [97]. Hydrogen could migrate in ZnO with the applied external electrical field [98, 99]. Wang *et al.* observed a significant degradation of electrical and optical properties of ZnO diodes due to hydrogen [100]. Therefore, unintentional doping of hydrogen and its conducting layers on the surface have been an issue in getting stable p-type ZnO and realizing ZnO based LEDs.

Due to these reason, passivation layers may be needed for ZnO based LEDs although hydrogen can be easily removed by thermal annealing or by irradiation with an electron beam [99, 101, 102]. Moazzami *et al.* used SiO<sub>2</sub> passivation layer to prevent surface interaction with ambient oxygen [82]. Hui *et al.* reported that AlO<sub>x</sub>-cap layer passivates oxygen deficiency sites and suppresses the detrimental surface states [103]. Schmidt *et al.* have investigated different dielectric materials (SiO<sub>2</sub>, Si<sub>3</sub>N<sub>4</sub>) to preserve or avoid the surface conducting [104].

### 2. 3 ZnO Based Ternary Alloys

In optoelectronic application, band-gap engineering is essential to getting highly efficient light emitting devices. The heterostructures provide barrier layers for quantum well formation, yields quantum confinement effects and improved device efficiency. Commercialized III-nitride semiconductors, such as GaN, AlN, InN, have band gap that vary with alloy composition, making band-gap engineering possible. Similar to nitride materials, the bandgap of ZnO can be varied by alloying with CdO, MgO, and BeO. The ternary system CdO-ZnO-MgO covers a large bandgap range, approximately 3 to 4 eV, while maintaining the wurtzite structure. Fig. 2-2 shows the bandgap and lattice constant of various semiconductors. There are many reports on  $Mg_xZn_{1-x}O$  films and ZnO-MgZnO heterostructures. Liu *et al.* grew  $Mg_xZn_{1-x}O$  thin films on sapphire substrates and investigated structural and optical properties [105]. Koike *et al.* reported ZnO/ $Zn_{0.7}Mg_{0.3}O$  multiple quantum wells grown with different layer thicknesses [106]. Also, there have been many attempts to achieve p-type ZnMgO films. Recently, heterojunction device with n-ZnMgO/ZnO/p-ZnMgO structure was achieved by using N-In codoped p-type ZnMgO layer [107]. Ye *et al.* reported p-type ZnMgO thin films codoped with Al and N via magnetron sputtering methods [108]. For monodoping, p-type conductivity in ZnMgO film have been achieved with P and Li dopants [109, 110]. Regarding to  $Cd_xZn_{1-x}O$  alloys, Makino *et al.* obtained single phase  $Cd_xZn_{1-x}O$  alloy films with 7% Cd [5]. Vigil *et al.* reported the bandgap decreasing from 3.28 eV for pure ZnO to 2.51 eV for  $Cd_xZn_{1-x}O$  alloys [111].

### 2. 4 ZnO Based Light Emitting Diodes

Prior to the recent achievements for p-type ZnO, most junction devices have been realized with heterojunctions that employ another p-type material instead of p-ZnO. Ohta *et al.* demonstrated p-SrCu<sub>2</sub>O<sub>2</sub>/n-ZnO heterostructures. The device showed the band-edge EL emission [112]. Alivov *et al.* have made heterojunction LED devices with p-Al<sub>0.12</sub>Ga<sub>0.88</sub>N/n-ZnO and p-

GaN/n-ZnO structures [38, 113]. EL emission was observed in both cases. Osinsky *et al.* obtained strong EL emission at 390 nm from n-Mg<sub>0.1</sub>Zn<sub>0.9</sub>O/n-ZnO/p-Al<sub>0.16</sub>Ga<sub>0.84</sub>N/p-GaN heterostructure LEDs [114].

Recently, there have been several promising reports on ZnO homojunction LEDs [8-11]. Until now most successful ZnO based light emitting diodes were fabricated by p-type ZnO using group V elements as a p-type dopant. Guo *et al.* fabricated a ZnO homostructural diode with the p-ZnO:N/n-ZnO junction grown on a ZnO wafer [115]. Lu *et al.* fabricated ZnO p-n homojunctions composed of a N-Al codoped p-type ZnO layer and an Al-doped n-type layer [116]. Tsukazaki *et al.* have fabricated a p-ZnO/i-ZnO/n-ZnO LED on a ScAlMgO<sub>4</sub> by using repeated-temperature-modulation epitaxy for p-type doping [8]. The current-voltage characteristics and EL results of the p-i-n structure are shown in Fig. 2-3. Most of the emission consisted of bands at 420 and 500 nm, with a small shoulder at 395nm assigned to radiative recombination in the p-ZnO through donor-acceptor pair transitions.

ZnO p-n homojunctions in n-ZnO bulk single crystal were reported by excimer-laser annealing a sample consisting of a p-type Zn<sub>3</sub>P<sub>2</sub> layer on bulk ZnO and by diffusion from a Zn<sub>3</sub>P<sub>2</sub> source, respectively [117, 118]. Recently, Lim *et al.* succeed in fabricating the UV light emitting ZnO homojunction LEDs by growing P-doped p-type ZnO on Ga-doped n-type ZnO [11]. They also used Mg<sub>0.1</sub>Zn<sub>0.9</sub>O as an energy barrier layer to confine the carriers to the high quality n-type ZnO and hence increase the intensity of near bandedge emission (Figure 2-4).

Arsenic also has been used as a p-type dopant for ZnO LEDs. Ryu *et al.* reported p-type ZnO by use of arsenic as the dopant element [65, 66], and recently fabricated ZnO-based ultraviolet light emitting diodes that employ a BeZnO/ZnO active layer comprised of seven quantum wells [10]. Figure 2-5 shows the IV characteristics and EL spectrum for a p-n junction

ZnO. The ZnO-based LEDs show two dominant electroluminescence peaks located in the ultraviolet spectral region between 360 and 390 nm, as well as a broad peak at 550nm.

Table 2-1. Valence and ionic radii of candidate p-type dopant atoms.

	Zn	Li	Na	K	Cu	Ag	O	N	P	As	Sb
Valence	+2	+1	+1	+1	+1	+1	-2	-3	-3	-3	-3
Radius (Å)	0.60	0.59	0.99	1.37	0.60	1.00	1.38	1.46	2.12	2.22	2.45

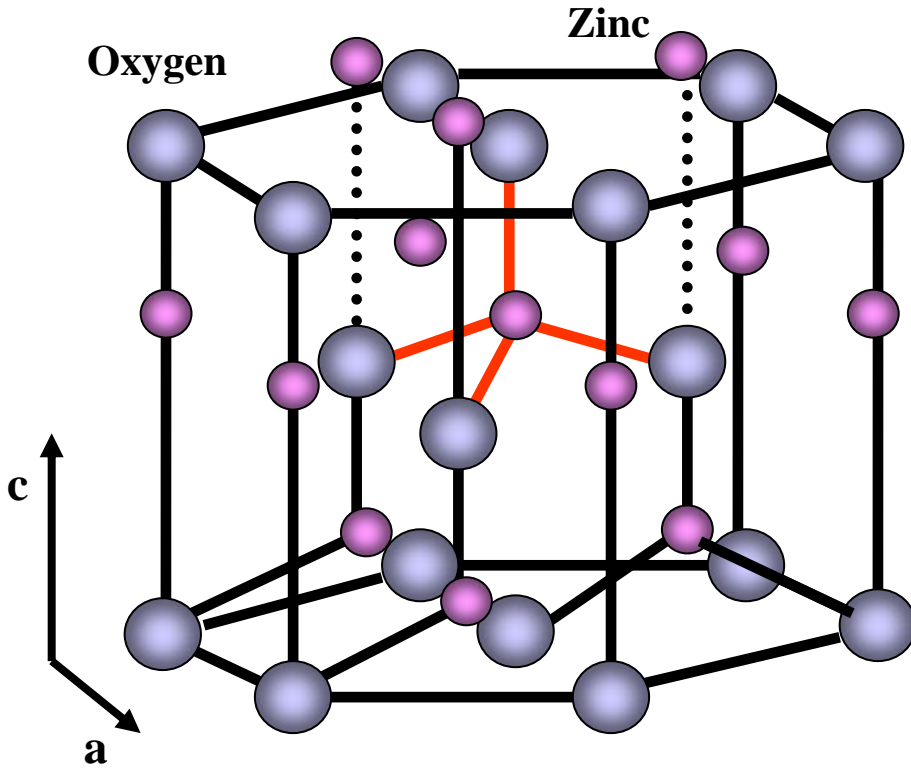


Figure 2-1. Crystal structure of wurtzitic ZnO.

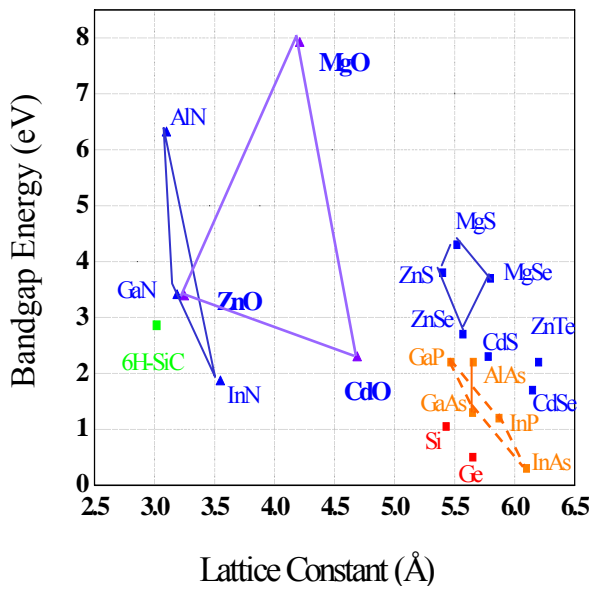


Figure 2-2. Bandgap versus lattice constant of various semiconductors.

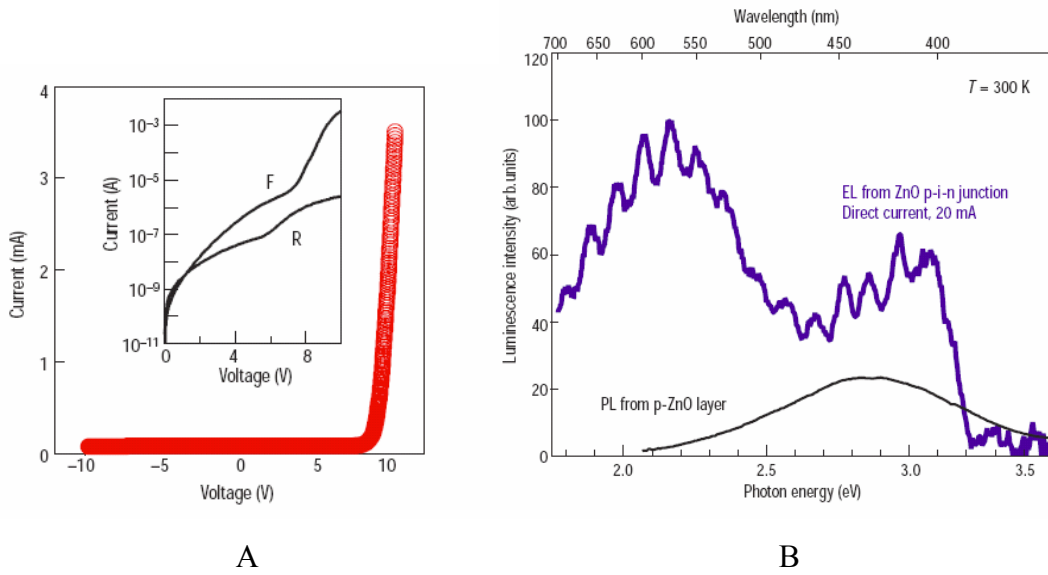


Figure 2-3. Zinc oxide homostructural p-i-n junction A) Current-voltage characteristics B) Electroluminescence spectrum [8].

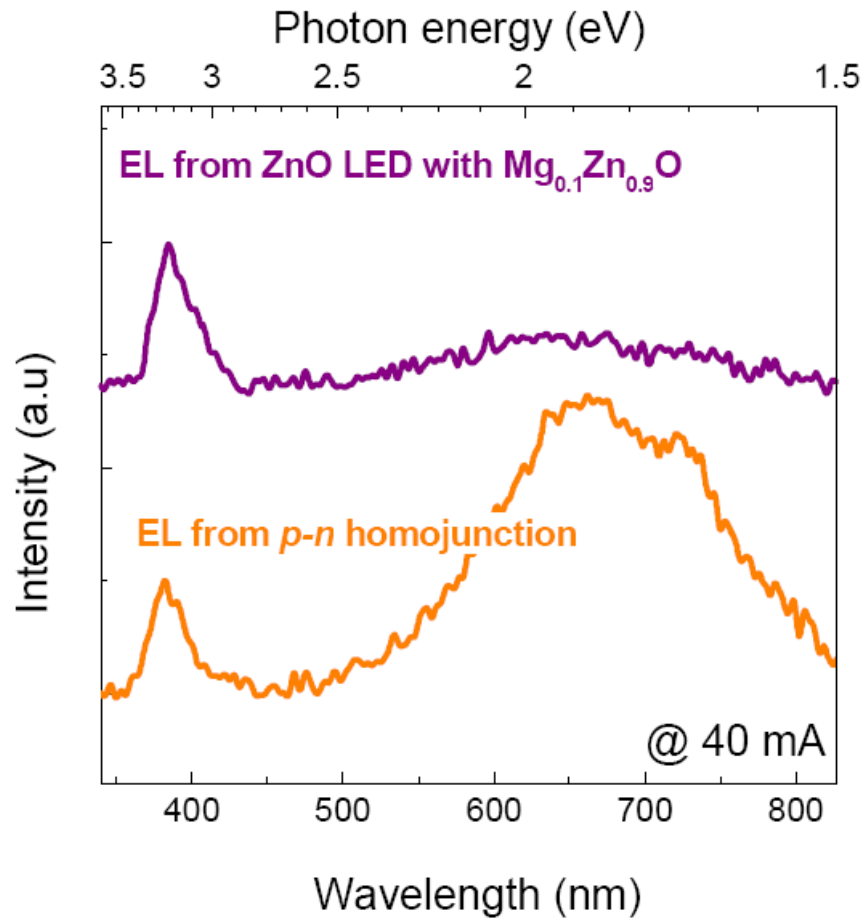


Figure 2-4. Comparison of EL spectra of the *p-n* homojunction ZnO LED and the ZnO LED with  $\text{Mg}_{0.1}\text{Zn}_{0.9}\text{O}$  layers, operated at a forward current of 40 mA [11].

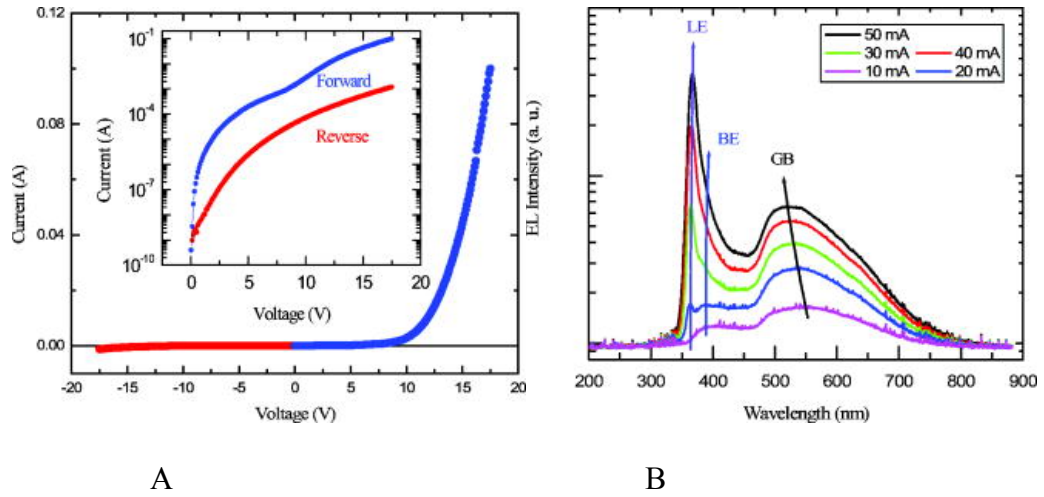


Figure 2-5. The p-n junction ZnO-based LED A) current-voltage (I-V) characteristics B) EL spectrum of ZnO pn junction having a BeZnO active layer measured at room temperature [10].

## CHAPTER 3 EXPERIMENTAL TECHNIQUES

This chapter will cover the experimental methods for thin film deposition and characterization of the ZnO films. All films discussed in this work were grown with pulsed laser deposition (PLD). Various analyzing tools were used to investigate the electrical, optical, structural properties of the films. The surface morphology and chemical bonding states were characterized as well. In order to test the device performance, current-voltage measurement and electroluminescence (EL) measurements were used. However, only the film deposition and the characterization techniques of these films will be described in this chapter.

### **3. 1 Growth Technique**

Pulsed laser deposition is one of the most widely used techniques in research laboratories to grow high quality oxide thin films. In this study, a KrF excimer laser was used as the ablation source. A focused laser pulse strikes a target of the desired composition in a vacuum chamber. This incident high power pulsed laser beam heats up the target materials well beyond the evaporation temperature and produces an ejected plasma or plume of atoms, ions, and molecules. The materials dissociated from the target surface are deposited as a thin film on a substrate. A schematic of pulsed-laser deposition system used in this work is shown in Fig. 3-1. The process is strongly dependent on following parameters: The laser fluence and wavelength, the structural and chemical composition of the target material, the chamber pressure and the chemical composition of the background gas, and the substrate temperature and the distance between the target and the substrate. The main advantages of pulsed laser deposition are its ability to produce a film with the same composition as the target, compatibility with a background gas, and atomic level control of the deposition rate. Multilayers or superlattices can be obtained by sequential PLD from various targets.

## 3. 2 Analytical Techniques

### 3.2.1 X-Ray Diffraction (XRD)

X-ray diffraction (XRD) is a non-destructive tool for studying material properties such as crystallinity, strain, and grain size. Also, the phase identification and orientation can be easily analyzed with this technique.

The incident X-rays interact with the periodic crystal planes and results in constructive and destructive interference. Only the condition satisfying the Bragg's Law gives the constructive interference.

$$\text{Bragg's Law : } n\lambda = 2d\sin\theta$$

where  $n$  is the order of diffraction,  $\lambda$  is the x-ray wavelength,  $d$  is the interplanar spacing of crystal planes, and  $\theta$  is the incident angle of x-ray.

In this research, Philips APD 3720 X-ray and Philips X'pert MRD high resolution diffractometers were used. The Philips APD 3720 system using Cu K $\alpha$  ( $\lambda = 1.5405\text{\AA}$ ) was employed for  $\Theta$ - $2\theta$  scans to check for preferred orientation of crystalline and identify any secondary phases induced in ZnO materials. The domain size can be obtained by using Scherrer's formula from  $\Theta$ - $2\theta$  scan:

$$\text{Scherrer's formula : } t = \frac{0.89\lambda}{B \cos \theta_B}$$

where  $t$  = thickness of crystallite,  $\lambda$  is the wavelength,  $B$  is FWHM (full width at half maximum), and  $\Theta_B$  is the Bragg angle. However, the APD 3720 system uses theta-2theta Bragg-Brentano setup and this hinders a geometric freedom. Thus, the Philips X'pert was used to get further information from the ZnO films. The Philips X'pert high resolution diffractometer uses 4-circle goniometer and gives various setting like omega, phi and Chi scan (Figure 3-2). At first,

the  $\omega$  rocking curve was used to study in-plane and out of plane crystalline quality. In ZnO materials, the edge and screw type dislocation density are obtained by  $\omega$  rocking for ZnO (002) and (102), respectively. In plane  $\phi$  scan gives the information about the crystalline symmetry. Regarding to epitaxial ZnO films, it shows a diffraction peaks with  $60^\circ$  interval indicating 6-fold symmetry and hexagonal structure. In order to investigate surface information, the grazing-incidence x-ray diffraction is used.

### 3.2.2 X-Ray Photoelectron Spectroscopy (XPS)

X-ray photoelectron spectroscopy (XPS) is an analytical technique used to investigate the chemical state, elemental composition, and electronic state at the sample surface. Monoenergetic X-rays irradiate a material and core electrons are ejected from the sample surface. These ejected electrons have characteristic binding energy which can be determined by the Rutherford equation.

$$E_{\text{binding}} = E_{\text{photon}} - E_{\text{kinetic}} - \Phi$$

Where  $E_{\text{photon}}$  is the characteristic energy of X-ray photon,  $E_{\text{kinetic}}$  is the kinetic energy of ejected photoelectron, and  $\Phi$  is the work function of the spectrometer. Each element can be identified with this specific binding energy of these ejected photoelectrons. The number of detected photoelectrons is related to the element concentration within the irradiated material surface.

Perkin-Elmer PHI 5100 ESCA system was used in the study. It consists of the X-ray source, the spectrometer, and a high vacuum. Al ( $E_{K\alpha} = 1.4866$  keV) or Mg ( $E_{K\alpha} = 1.2566$  keV) were used for the X-ray source. The chemical bonding of phosphorus in ZnO was examined to investigate the doping behavior of  $P_2O_5$  dopant source. The sample surface was sputtered with Argon gas to get accurate information by removing the surface contamination.

### 3.2.3 Atomic Force Microscopy (AFM)

Atomic force microscope (AFM) was used to characterize the surface topography and morphology of the films. AFM operates by measuring an interatomic force between a sharp tip at the end of the cantilever and the sample. The interatomic force contributes to the cantilever deflection. As the tip scans the sample surface, the cantilever bends by responding to the topography of the sample surface. The position of the laser beam on the detector reflecting the position of the cantilever, shifts with displacement. As a result, the position sensitive photodiode generates topographic data by sensing this cantilever deflection. A schematic of this mechanism is shown in Fig. 3-3.

An AFM Dimension 3100 (Digital Instrument, Inc.) was used in this study. This system can operate in both contact and tapping modes. In the contact mode, the probe scans across the surface while touching the surface. The contact mode can create a friction force and cause sample damage. On the other hand, the tapping mode uses a feedback loop. If the tip moves close to the surface it causes amplitude damping. This can be used for adjusting the tip-sample distance to maintain constant amplitude in the feedback loop. The surface damage would be suppressed in the tapping mode.

### 3.2.4 Hall Effect Measurement

The Hall effect is used to investigate the transport properties such as the carrier density, resistivity, mobility and carrier type. If a magnetic field is applied perpendicular to the current flow, an electric field is set up perpendicular to both the current direction and magnetic field due to the charge separation. This established potential difference is called the Hall voltage  $V_H$ . The Hall measurement gives the Hall coefficient. The Hall coefficient  $R_H$  can be written as

$$R_H = \frac{r(p - b^2n)}{q(p + bn)^2}, = \frac{r}{qp} \text{ (p} \gg \text{n, extrinsic p-type), } = -\frac{r}{qp} \text{ (n} \gg \text{p, extrinsic n-type)}$$

Where b and r are scattering factors, n and p are electron and hole density, respectively.

Also, it can be determined experimentally as

$$R_H = \frac{tV_H}{BI} = \frac{1}{qp} (p\text{-type}) = -\frac{1}{qn} (n\text{-type})$$

Where t is the sample thickness, B is the magnetic field, I is the current, and q is the magnitude of the electron charge. The carrier type and carrier density are determined with this Hall coefficient. Also, the resistivity and mobility can be simply calculated by following equations.

$$\text{Resistivity : } \rho(\Omega\text{-cm}) = \frac{Rwt}{L} = \frac{V/I}{L/wt}$$

where w is sample width and L is sample length.

$$\text{Mobility : } \mu_n = \frac{\sigma}{qn} = \frac{1/\rho}{q(1/qR_H)} = \frac{R_H}{\rho}, \mu_p = \frac{\sigma}{qp} = \frac{1/\rho}{q(1/qR_H)} = \frac{R_H}{\rho}$$

where  $\sigma$  is the conductivity.

The temperature dependent Hall measurements give important additional information. The dopant activation energy  $E_A$  can be extracted from the slope of a  $\log(p \text{ or } n)$  versus  $1/T$  plot.

### 3.2.5 Photoluminescence (PL)

Photoluminescence (PL) is a nondestructive technique identifying and investigating impurities in semiconductor materials. PL is the spontaneous light emission from recombining photo-excited electron-hole pairs. The optical excitation source, having greater energy than the bandgap of the semiconductors, moves an electron to a higher energy state. The electron returns to a lower energy state by radiating a photon. Only radiative recombination contributes to the light emission. The nonradiative recombination, the deep level in the bulk and surface recombination centers, does not generate PL signal.

Electron-hole pairs recombine with several possible paths and each recombination process determines the emitted photon energy. There are five most common recombination processes

(Figure 3-4).

- Band-to-band recombination (a)
- Free exciton recombination (b)
- Bound exciton recombination (free hole – neutral donor) (c)
- Bound exciton recombination (free electron – neutral acceptor) (d)
- Donor-acceptor recombination (e)

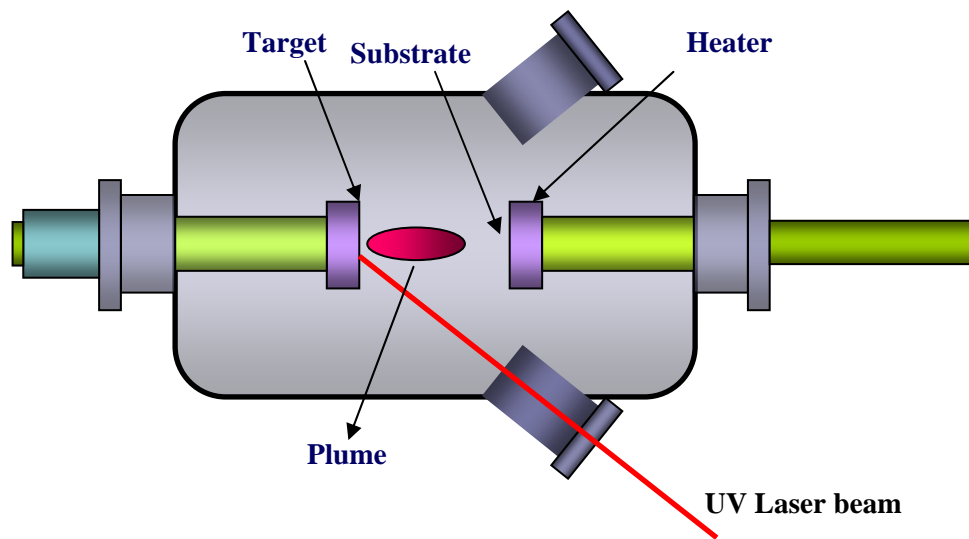


Figure 3-1. Pulsed-laser deposition system.

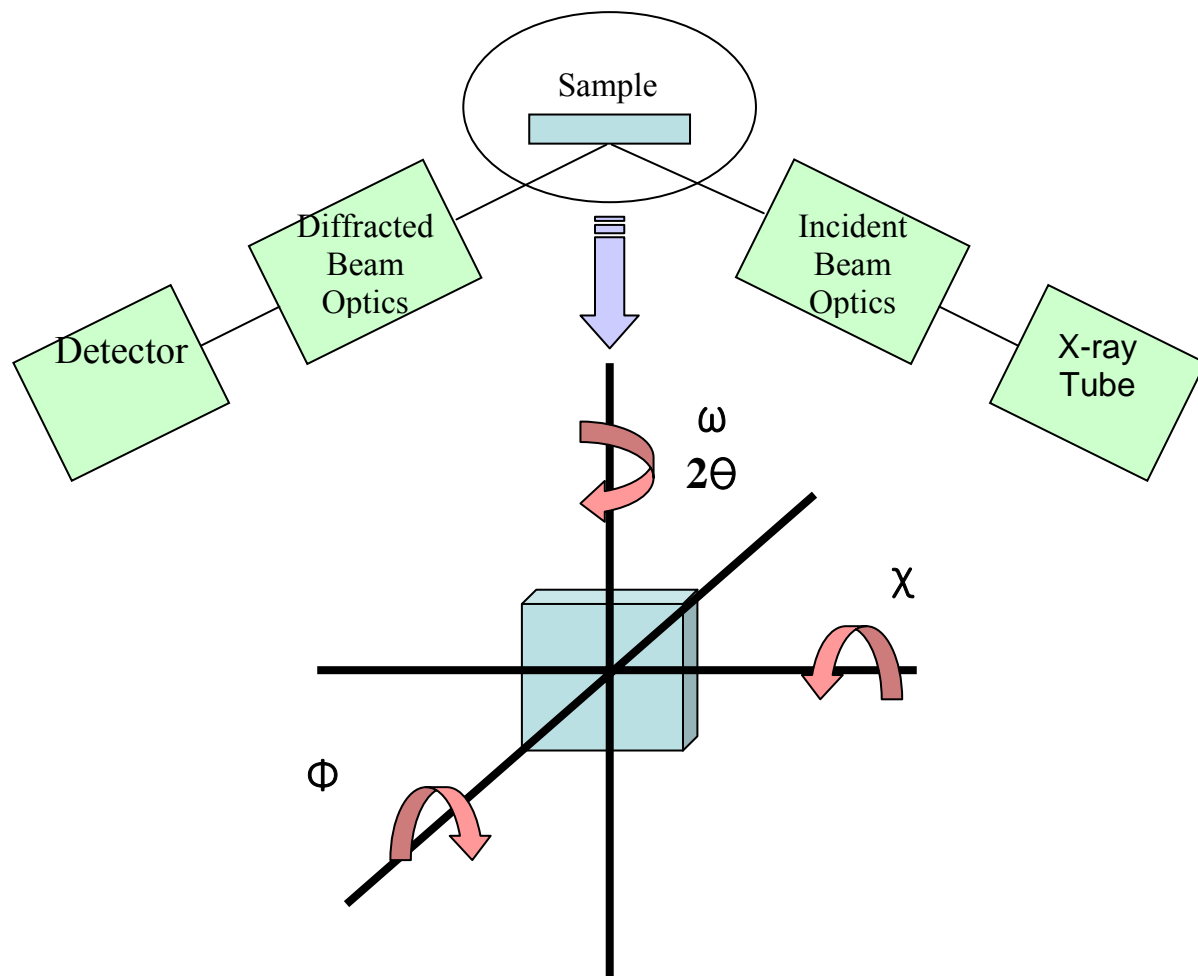


Figure 3-2. Philips X'pert high resolution diffractometer using 4-circle goniometer.

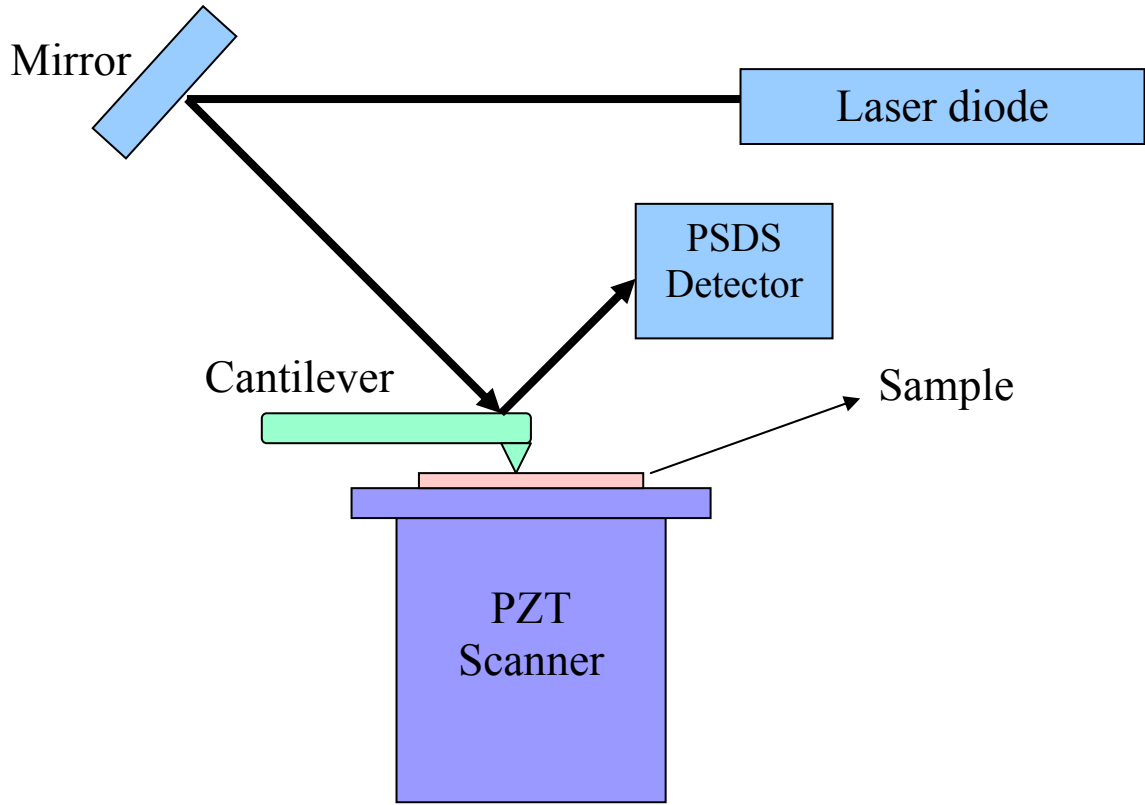


Figure 3-3. Optical detection mechanism in AFM .

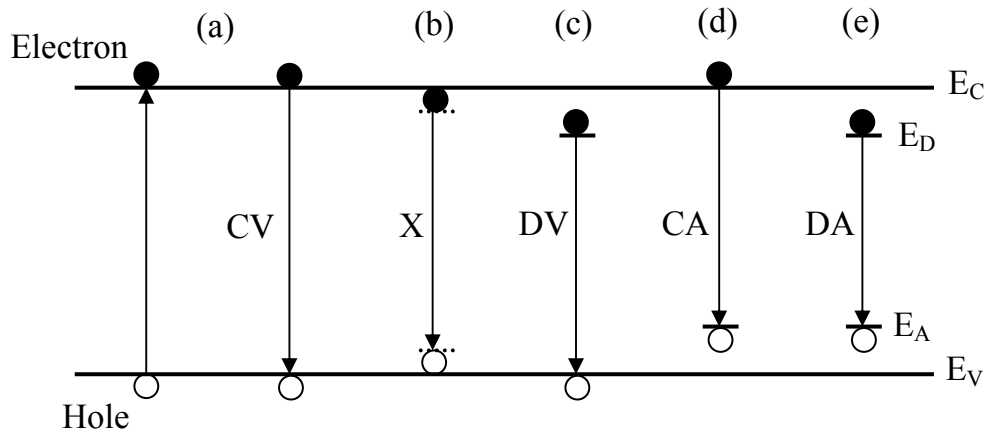


Figure 3-4. Radiative recombination mechanisms.

CHAPTER 4  
ZINC OXIDE THIN FILMS GROWN WITH O<sub>2</sub>/O<sub>3</sub> MIXTURE GAS

**4. 1 Introduction**

The defect mechanisms and the electronic behavior of chemical dopants in ZnO are not completely understood. Relevant native defects include vacancies (V<sub>o</sub> and V<sub>zn</sub>), interstitials (Zn<sub>i</sub> and O<sub>i</sub>), and antisites (Zn<sub>o</sub> and O<sub>zn</sub>). These defects have significant influence on the electrical and optical properties of the films. Therefore, controlling native defects and doping is important in realizing ZnO based devices. In particular, the residual donor defects in ZnO compensate the acceptor dopants and inhibit the realization of majority carrier p-type ZnO. Therefore, decreasing the background native donor density and achieving high quality undoped films are essential elements in realizing robust p-type materials.

One way to modify the distribution of native defects is through the selection of oxidation conditions. In an effort to control the oxygen-related defect density, several groups have explored the use of different oxidant sources. In molecular beam epitaxy, ozone/oxygen mixtures [119], hydrogen peroxide and nitrogen dioxide have been explored as oxidant sources [120, 121]. El-Shaer *et al.* reported high quality ZnO film growth using H<sub>2</sub>O<sub>2</sub> in chemical beam epitaxy [122]. N<sub>2</sub>O, H<sub>2</sub>O and O<sub>3</sub> have been examined as alternative oxidant sources in MOCVD and ALD methods [123, 124].

In addition to the growth ambient, thermal annealing also can be used to control these native defects. Post-annealing is typically performed to improve crystal quality and/or activate dopants [92, 125, 126]. Post-growth thermal annealing also can be an effective way to manipulate the residual donor defect density. In particular, annealing ZnO films under oxygen ambient should decrease the density of oxygen vacancies and related defects introduced during

thin-film growth. The effects of annealing treatments depend not only on the specific annealing conditions, but on the method used to grow the initial films [127-129].

In this chapter, we discuss the use of an O<sub>2</sub>/O<sub>3</sub> mixture as an oxidant source and examine the electrical and optical properties of ZnO thin films grown in ozone as compared to molecular oxygen. Also, post-growth thermal annealing was performed for these samples. The annealing behavior for ZnO thin films grown by pulsed laser deposition using ozone as the oxidant is examined. The properties of ZnO films grown in an O<sub>2</sub>/O<sub>3</sub> gas mixture and annealed in oxygen are compared to films grown and annealed in molecular oxygen.

## 4. 2 Experimental

The ZnO films were grown on single crystal c-plane sapphire by pulsed laser deposition. The ZnO ablation target was prepared by sintering high purity (99.99995 %) ZnO powder at 1000 °C in air. The ZnO targets were ablated by a KrF excimer laser with a laser fluence of ~ 1.5 J/cm<sup>2</sup> and laser frequency of 1 Hz. The background gas introduced during the growth was either pure O<sub>2</sub> or an O<sub>2</sub>/O<sub>3</sub> gas mixture. The O<sub>2</sub>/O<sub>3</sub> gas mixture used in this study contains ~2-3% ozone. Pure molecular oxygen gas was also used for comparison. The growth temperature was 650 °C and the film thickness was approximately 400 nm for the samples discussed in this chapter. The pressure during growth was varied from 10<sup>-1</sup> to 10<sup>-5</sup> Torr. After the growth, thermal annealing was performed at 500 - 900 °C under oxygen ambient for 30 mins. The room temperature electrical properties were investigated by Hall measurements using four-point van der Pauw method with a commercial LakeShore Hall measurement system. The optical properties of the ZnO films were examined by photoluminescence (PL) spectroscopy using a He-Cd laser (λ = 325 nm) as the excitation source. The crystallinity was characterized by using a

Philips MRD X'pert x-ray diffraction system. The surface morphology was examined via atomic force microscopy.

## 4.3 Results and Discussion

### 4.3.1 Electrical and Optical Properties of ZnO Thin Films Grown with O<sub>2</sub>/O<sub>3</sub> Gas Mixture

Figure 4-1 shows the carrier concentration of the ZnO films grown with O<sub>2</sub>/O<sub>3</sub> mixture gas and pure O<sub>2</sub> gas as a function of growth pressure. The ZnO films grown with O<sub>2</sub>/O<sub>3</sub> mixture gas exhibit lower donor defect density as compared to those grown with pure O<sub>2</sub> for the entire pressure regime considered. The lowest carrier density for ZnO film grown with O<sub>2</sub>/O<sub>3</sub> mixture gas,  $6.2 \times 10^{16} \text{ cm}^{-3}$ , is almost one order of magnitude lower than that for a ZnO film grown with O<sub>2</sub>, where the electron carrier density is  $2.0 \times 10^{17} \text{ cm}^{-3}$ . In addition, the donor density initially decreased with increasing pressure, although increasing the pressure above 50 mTorr yielded an increase in the donor density for both cases of O<sub>2</sub> and O<sub>2</sub>/O<sub>3</sub> growth. This increase of donor defect density at this higher pressure regime can most likely be attributed to changes in growth kinetics due to collisions of the ablated plume species with the background gas. It is well known that increasing the background pressure in the 10-100 mTorr range yields a decrease in ablated species kinetic energies. If one assumes that the increase in residual donor density reflects an increase in oxygen vacancy-related defects, then the kinetic energy of the ablated species must be actively facilitating the formation of fully oxidized ZnO films. It should be noted that the insertion of excess oxygen atoms can generate O-related defects, in particular O<sub>i</sub>-O, that has been assigned as a double donor [130]. However, this seems less likely since the increase in donor density first occurs with molecular oxygen, which has a lower oxidation potential than ozone.

The decrease in donor defect density for ZnO films grown with O<sub>2</sub>/O<sub>3</sub> gas mixture relative to those grown in molecular oxygen can be explained by the decrease of oxygen vacancy-related defects, and by an increase of acceptor defects that compensate the residual native donors. While

there is continued debate in the literature regarding the specific defects that yields the shallow donor state, oxygen vacancies and zinc interstitials are clearly associated with the onset of unintentional n-type conductivity in ZnO [131]. If we assume that oxygen vacancies are a primary or secondary source for residual donor defects, it is expected that oxygen vacancies are compensated by oxygen atoms and that the donor defect density will decrease with increased pressure. However, in our experiments the donor density increased again at high pressure for both cases of O<sub>2</sub> and O<sub>2</sub>/O<sub>3</sub> growth. Also, several groups reported that oxygen vacancies should be deep donors rather than shallow donors in n-type material [132-134]. Therefore, compensating oxygen vacancies may not fully explain the decrease of the donor defect density of the ZnO films grown with O<sub>2</sub>/O<sub>3</sub>. Zn interstitials, which have been considered as another source for n-type conductivity, also have a high formation energy [130]. The lower donor defect density of ZnO films grown with O<sub>2</sub>/O<sub>3</sub> may not be due to compensating Zn<sub>i</sub>. Thus, it is reasonable to consider alternative mechanisms, in addition to eliminating oxygen vacancies or zinc interstitials, in understanding the lower carrier density of ZnO films grown with O<sub>2</sub>/O<sub>3</sub> mixture gas.

There are several defect structures that can affect the electrical properties of ZnO, namely vacancies (V<sub>o</sub> and V<sub>zn</sub>), interstitials (Zn<sub>i</sub> and O<sub>i</sub>), and antisites (Zn<sub>o</sub> and O<sub>zn</sub>). In order to examine the data, a plot is made of the ratio of donor defect density of the ZnO films grown with either O<sub>2</sub> or O<sub>2</sub>/O<sub>3</sub> (Figure 4-2). The low pressure region is designated as Zn rich and the high pressure region as O-rich condition. The difference of donor defect density between the ZnO sample grown with O<sub>2</sub> and O<sub>2</sub>/O<sub>3</sub> mixture was significant, 20 times lower, for pressures above 50 mTorr, while it is smaller at a lower pressure even though the ZnO sample grown with O<sub>2</sub>/O<sub>3</sub> mixture gas yields a lower defect donor density. This decrease might be explained by highly active oxygen atoms generating acceptor defects such as Zn vacancies and oxygen interstitials. These

Zn vacancies and oxygen interstitials would be generated under O-rich condition because they have low formation energy at O-rich condition [135] and effectively compensate residual donor defects. On the other hand, the formation of Zn vacancies and oxygen interstitials is not favorable at Zn-rich conditions, and thus active oxygen atoms cause defects rather than generate acceptors that could compensate a residual donor. It appears that O<sub>3</sub> generates acceptors, such as Zn vacancies and O interstitials, only at O-rich condition leading to a decrease in background donor defect density. However, further increasing the growth pressure increases the defect donor density again. This increase in donor density with oxygen pressure of 100 mTorr is related to gas-phase collisions in the plume decreasing the oxidation processes in film growth. Therefore, the lower donor defect density of the ZnO samples grown with O<sub>2</sub>/O<sub>3</sub> is due to the increase the acceptor defects rather than just elimination of native donors. However, the native donor defects are still dominant and the number of acceptor defects created in the film too small to overcome donor defects. Thus, the films remain n-type.

Figure 4-3 depicts the Hall mobility as a function of the pressure. The Hall mobility of ZnO films grown with pure oxygen gas is higher than that of ZnO films grown with O<sub>2</sub>/O<sub>3</sub> mixture gas up to 1 mTorr. There was no general trend above that pressure. The lower mobility of ZnO samples grown with O<sub>2</sub>/O<sub>3</sub> mixture gas at the low pressures range is probably due to the defects generated in ozone growth. However, at 10 and 100 mTorr, the mobility of ZnO grown with O<sub>2</sub>/O<sub>3</sub> is comparable with that of the film grown O<sub>2</sub>.

We also investigated the PL properties at room temperature (Figure 4-4). The PL shows strong bandedge emission with very weak deep level for the ZnO samples grown with pure O<sub>2</sub> gas regardless of the pressure. On the contrary, emission from deep levels increases with increasing pressure for the ZnO samples grown with the ozone mixture gas. The deep level

emission of the ZnO sample grown with pure O<sub>2</sub> gas increases slightly with pressure, but the change is not significant compared to the case of ZnO samples grown with O<sub>2</sub>/O<sub>3</sub> gas mixture. For the ZnO films grown with O<sub>2</sub>/O<sub>3</sub> gas mixture, the deep level is almost the same for pressures up to 10 mTorr. However, above 50 mTorr, it increases with pressure. There are two broad peaks at around 510 nm and 700 nm for the ZnO films grown with ozone mixture gas. The green emission has been attributed to the transition from conduction band to zinc vacancies, which are deep acceptors, while the red emission is related to deep acceptors such as oxygen interstitials [136-138]. The broad peaks of red emission shown at around 700 nm are similar to peaks seen in post-annealed ZnO and ZnO:P films under oxygen ambient [92, 139]. This indicates that active ozone causes similar effects on the ZnO samples with thermal annealing, such as in creating deep acceptor levels, leading to a decrease in donor defect density.

The intensity of the bandedge emission is shown in Fig 4-5. The ZnO samples grown with pure oxygen gas showed higher intensity in bandedge emission than those grown with ozone mixture gas for the entire pressure range. This is probably due to the non-radiative deep level defects generated by ozone growth. Therefore, the radiative band edge recombination is reduced. This is related to the low carrier density of ZnO samples grown with ozone mixture gas. This indicates that the ozone growth increases the deep level emission and generates non-radiative centers

#### **4.3.2 Post-Annealed ZnO Thin Films Grown with O<sub>3</sub>**

The structural properties of the films were examined both as-deposited and after annealing. In general, the crystalline properties of the films grown with O<sub>2</sub> or O<sub>2</sub>/O<sub>3</sub> were similar. Figure 4-6 shows the x-ray diffraction  $\omega$  rocking curves for the ZnO (002) reflection in films grown with pure O<sub>2</sub> and O<sub>2</sub>/O<sub>3</sub> gas mixture. The ZnO films grown with O<sub>2</sub> or O<sub>2</sub>/O<sub>3</sub> showed similar rocking

curve full width at half maximum (FWHM) in the as-grown state. Annealing results in a significant improvement of crystallinity compared to the as-deposited material. In particular, the ZnO films annealed at 900°C showed a 25-30 % decrease in x-ray diffraction rocking curve FWHM compared to the as-grown state.

The surface morphology of the annealed films is shown in Fig. 4-7. The as-grown ZnO films grown with O<sub>2</sub>/O<sub>3</sub> mixture gas show a smoother surface as compared to the ZnO samples grown with pure O<sub>2</sub> for the specific experimental conditions considered. On the surface of ZnO samples grown with pure O<sub>2</sub>, ZnO islands gradually disappear as the annealing temperature increases. The post annealing improves surface roughness for both cases.

Fig. 4-8 shows the carrier density for the annealed ZnO films grown with pure O<sub>2</sub> and O<sub>2</sub>/O<sub>3</sub> mixture. The carrier density of as-grown ZnO films grown with O<sub>2</sub>/O<sub>3</sub> is one order of magnitude lower than that for ZnO grown with pure O<sub>2</sub>. The carrier concentration of ZnO films grown with pure O<sub>2</sub> generally decreases with oxygen annealing. Interestingly, the carrier concentration of the ZnO films grown with O<sub>2</sub>/O<sub>3</sub> mixture gas slightly increases with oxygen annealing. At the highest annealing temperature of 900 °C, the carrier density increases for both cases. The decrease in donor density for the ZnO films grown with pure O<sub>2</sub> can be explained as follows. First, thermal annealing in O<sub>2</sub> could cause oxygen diffusion into the film, decreasing oxygen deficiency or Zn interstitials in ZnO. Note that oxygen vacancies are not shallow donors. However, it has also been shown that hydrogen is a shallow donor in ZnO [19]. In addition, hydrogen easily diffuses in ZnO [101, 102, 140]. Regardless of the microscopic origin, the shallow donor defect density will generally decrease with the annealing [141]. The ZnO films grown with O<sub>2</sub>/O<sub>3</sub> show the opposite behavior. It was previously reported that ozone can create deep acceptor-like defects in ZnO [142]. The introduction of these defects yields a lower donor

defect density for the as-deposited ZnO samples grown with O<sub>2</sub>/O<sub>3</sub> [59]. The transport properties of the films are determined by native donor defects and the acceptor-like defects caused by ozone. As the annealing temperature increases, the increase in effective electron density extracted from the Hall measurements suggests that the annealing treatment annihilates the ozone-induced acceptor defects that compensate the donors. This decrease competes with decreasing native donor defects as seen for films grown in O<sub>2</sub>. However, the decrease in acceptor defects dominates the change in donor density for films grown in ozone. It should be noted that similar ozone-related acceptor states may be created at the near-surface region when ZnO is exposed to ozone. This may explain the observed improvement in Schottky diode performance when ozone treatment of the ZnO surface is employed prior to metal deposition [143].

The behavior of carrier mobility with annealing is shown in Fig. 4-9. The mobility of the ZnO samples grown in O<sub>2</sub> changes little with annealing, at least up to annealing temperatures of 800°C. The mobility for ZnO samples grown with ozone initially drops at low annealing temperature and slowly increases with higher temperature annealing. The ZnO films grown with O<sub>2</sub>/O<sub>3</sub> mixture gas show a lower mobility over the entire annealing temperature range as compared to ZnO films grown with pure O<sub>2</sub>. This lower mobility probably reflects the compensated carrier density due to the presence of ozone-induced acceptors.

Room temperature photoluminescence for ZnO films is shown in Fig. 4-10. The PL spectra for the as-deposited films are dominated by the near band edge peak, with only weak visible emission due to the mid-gap transitions. However, the visible emission due to defect states increased significantly for annealing temperatures above 700 °C. Increasing the deep level emission in ZnO with post-annealing has been reported elsewhere [126, 144, 145]. ZnO samples grown with pure O<sub>2</sub> and O<sub>2</sub>/O<sub>3</sub> mixture gas showed the same behavior for the deep level

emission. Interestingly, the band edge emission of annealed ZnO films shows different behavior depending on the oxidation source used during growth. The intensity of band edge emission as a function of annealing temperature is shown in Fig. 4-11. The intensity of band edge emission of ZnO samples grown with pure O<sub>2</sub> increases at the annealing temperature of 500 °C, then decreases as the annealing temperature increases further. On the other hand, the intensity of band edge emission of ZnO samples grown O<sub>2</sub>/O<sub>3</sub> mixture gas was not affected by the annealing temperature. The band edge emission is due to the exciton recombination. Relaxation through deep traps competes with exciton emission. Therefore, we can deduce that the non-radiative traps of ZnO samples grown with O<sub>2</sub>/O<sub>3</sub> mixture gas are not significantly affected by the annealing and have a different origin from that of ZnO films grown with pure O<sub>2</sub>. The source is probably due to the acceptor-like defects caused by ozone.

#### 4. 4 Summary

ZnO films grown with O<sub>2</sub>/O<sub>3</sub> mixture gas exhibit a lower donor density than those grown with pure O<sub>2</sub> gas. The lower donor density is attributed to the generation of acceptor defects such as V<sub>Zn</sub> and O<sub>i</sub> compensating the residual donor defects. It should be noted that, for all films considered, the carrier type remained n-type. For the PL properties, ozone growth increases the deep level emission and generates non-radiative centers.

The effects of post-growth annealing on the properties of ZnO films grown with pure O<sub>2</sub> and O<sub>2</sub>/O<sub>3</sub> mixture gas are reported. The carrier density of ZnO films grown with pure O<sub>2</sub> generally decreases with annealing. In contrast, the carrier density of the ZnO films grown with O<sub>2</sub>/O<sub>3</sub> mixture gas slightly increases. This difference suggests that reducing the density of acceptor defects generated by ozone with annealing contributes to the increase in the donor density even though the residual donor defects are also decreased with the annealing. The ZnO

samples grown with  $O_2/O_3$  mixture gas shows consistent intensity of the bandedge emission regardless of the annealing temperature, while the intensity of the bandedge emission of the ZnO samples grown with pure  $O_2$  is affected by the annealing.

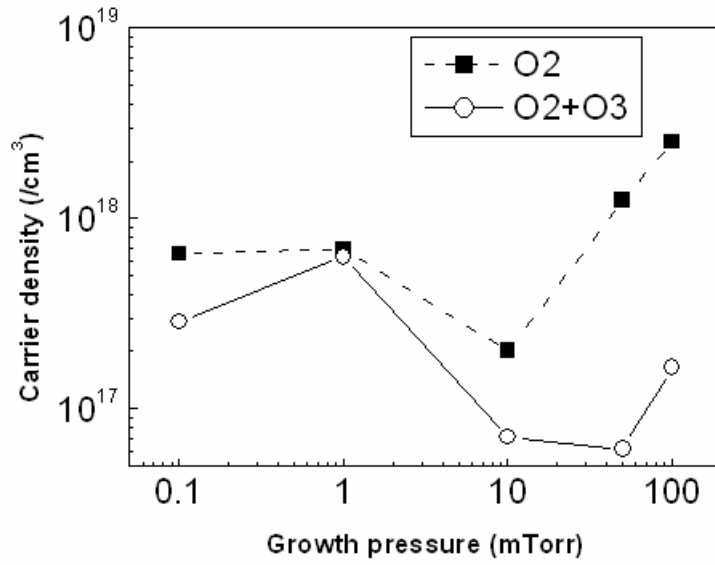


Figure 4-1. Carrier density of ZnO films grown with pure O<sub>2</sub> and O<sub>2</sub>/O<sub>3</sub> mixture gas at various pressures.

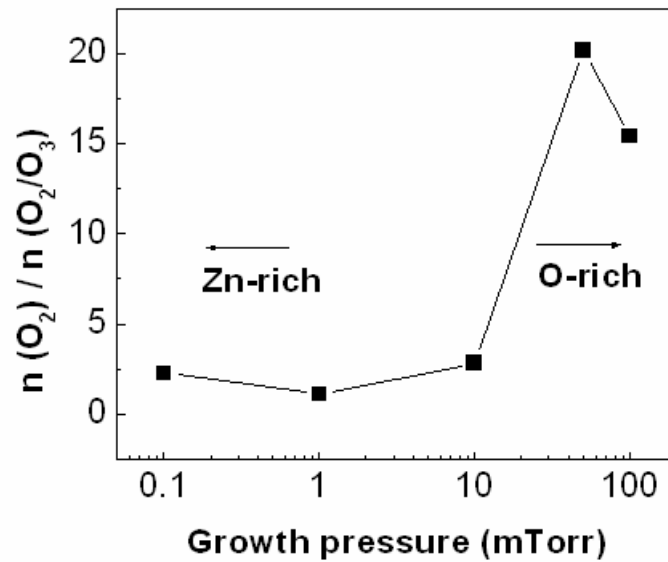


Figure 4-2. Ratio of donor defect density of the ZnO films grown with O<sub>2</sub> and O<sub>2</sub>/O<sub>3</sub>.

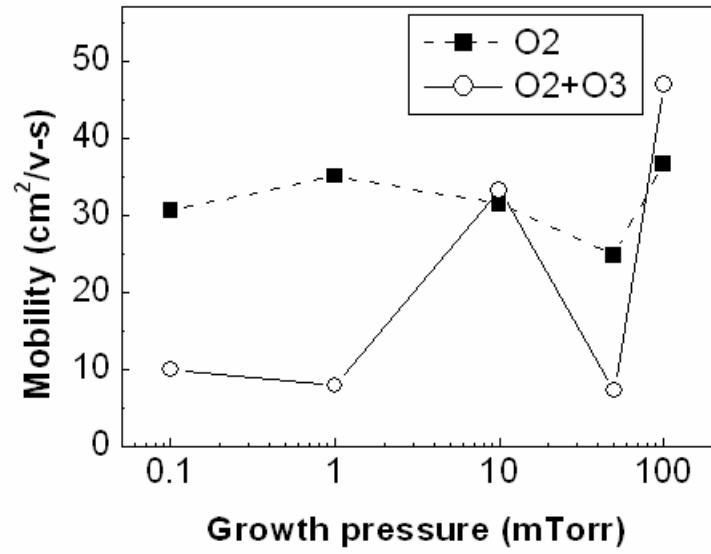
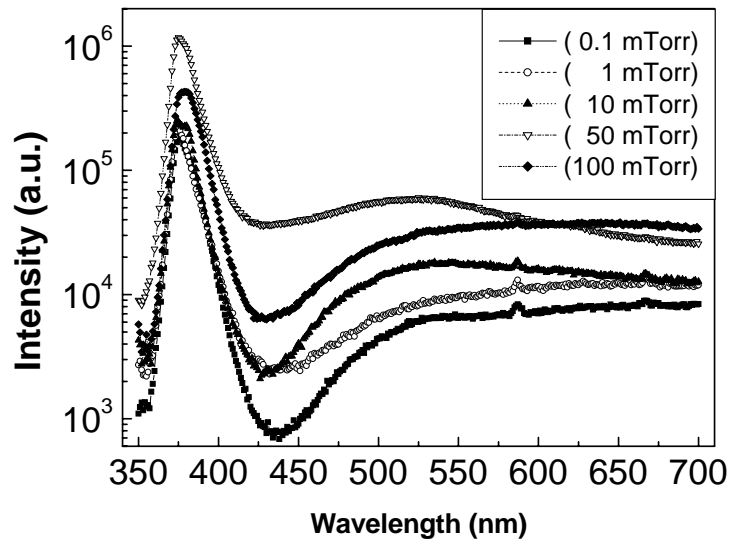
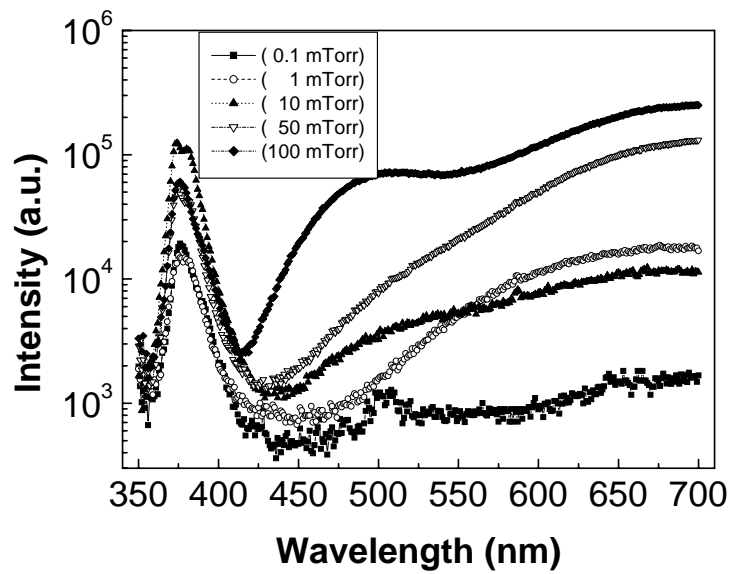


Figure 4-3. Mobility of ZnO films grown with pure O<sub>2</sub> and O<sub>2</sub>/O<sub>3</sub> mixture gas at various pressures.



A



B

Figure 4-4. Room-temperature PL spectra of ZnO films A) grown with pure  $O_2$  and B)  $O_2/O_3$  mixture gas.

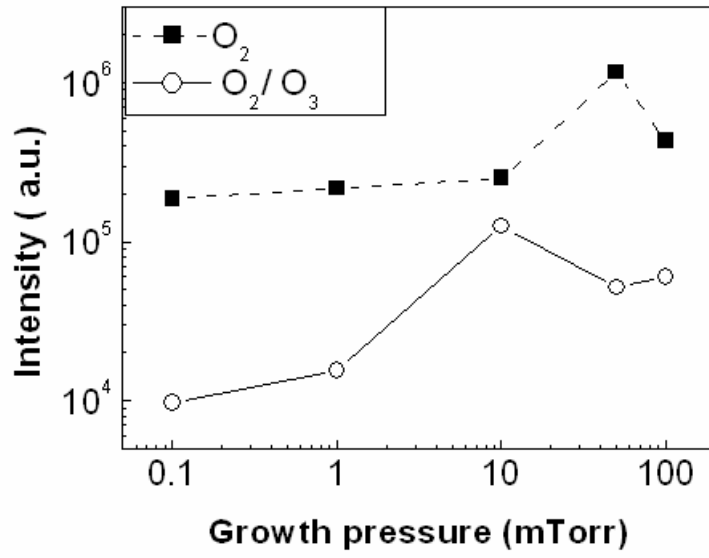
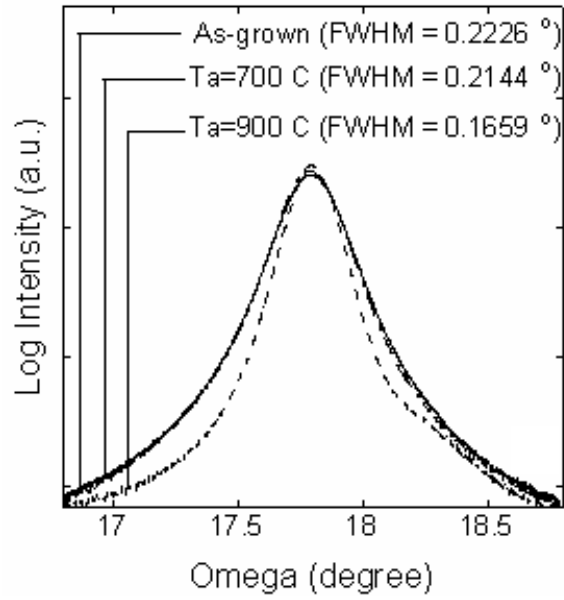
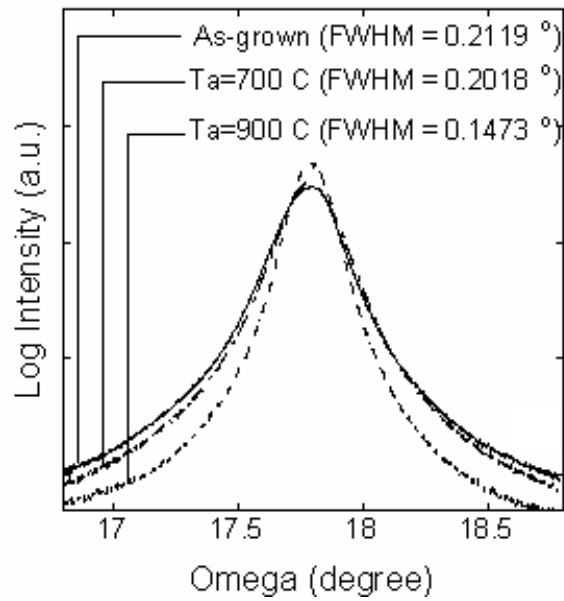


Figure 4-5. Intensity of bandedge emission of ZnO films grown with pure  $O_2$  and  $O_2/O_3$  mixture gas at various pressures.



A



B

Figure 4-6. X-ray diffraction omega rocking curves for ZnO films grown with A) pure O<sub>2</sub> B) O<sub>2</sub>/O<sub>3</sub> mixture gas.

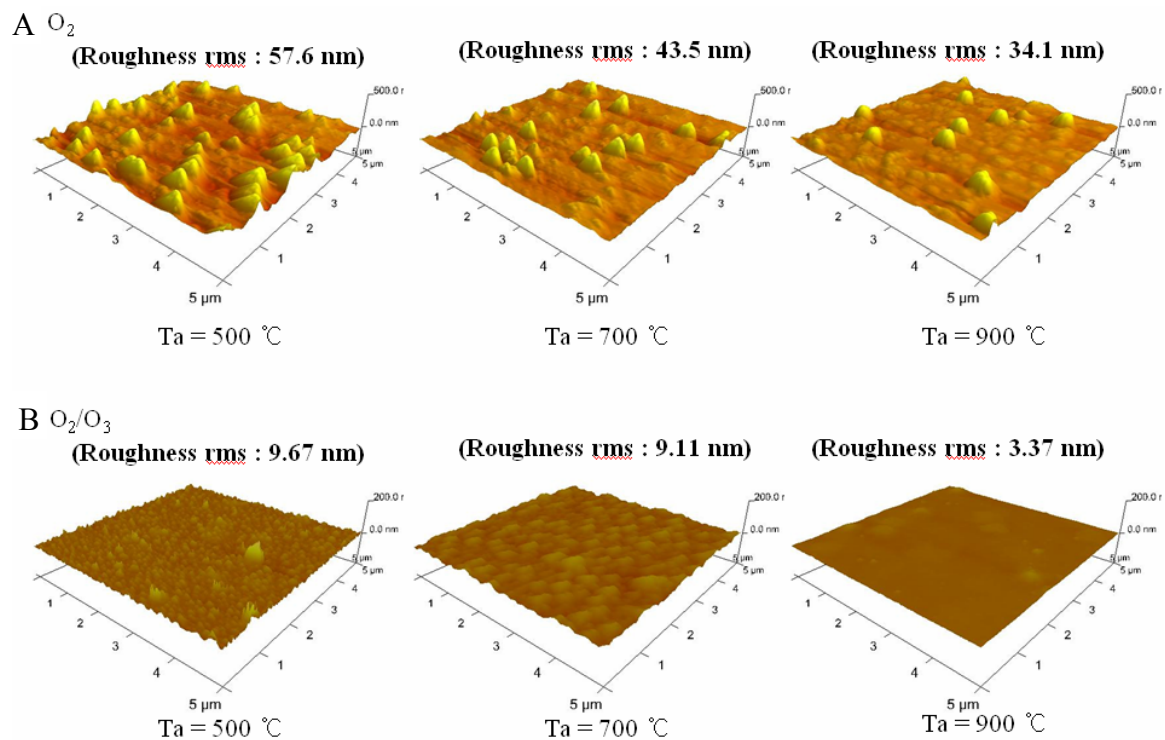


Figure 4-7. Atomic force microscopy images for annealed ZnO films grown with A) pure O<sub>2</sub> B) O<sub>2</sub>/O<sub>3</sub> mixture gas.

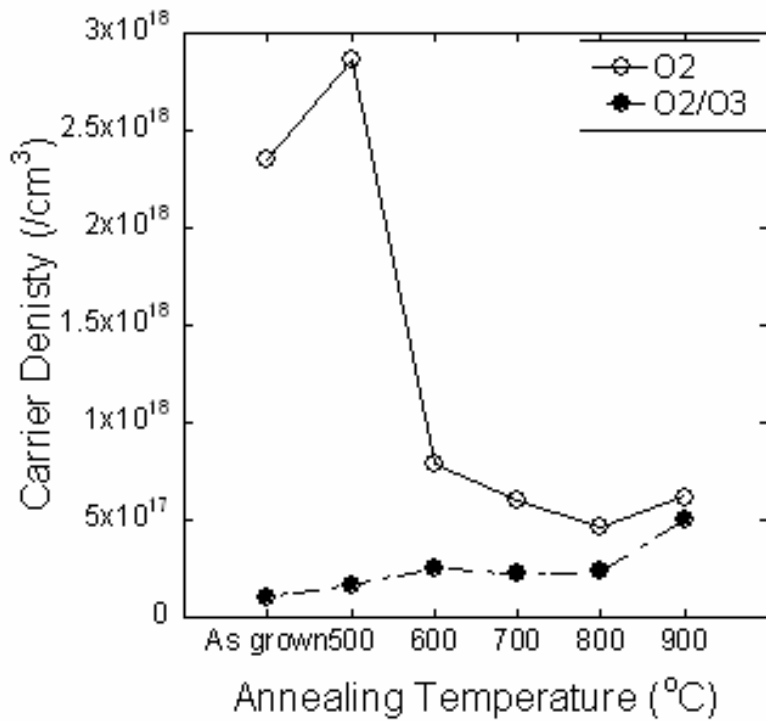


Figure 4-8. Carrier density of ZnO films grown with A) pure O<sub>2</sub> B) O<sub>2</sub>/O<sub>3</sub> mixture gas as a function of the annealing temperature.

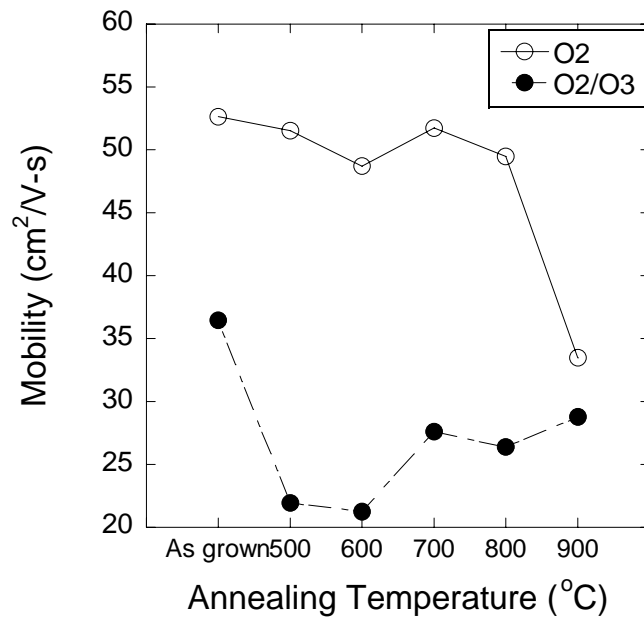
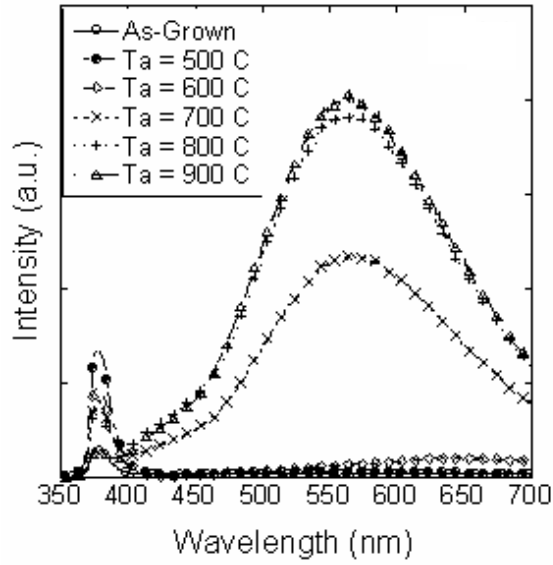
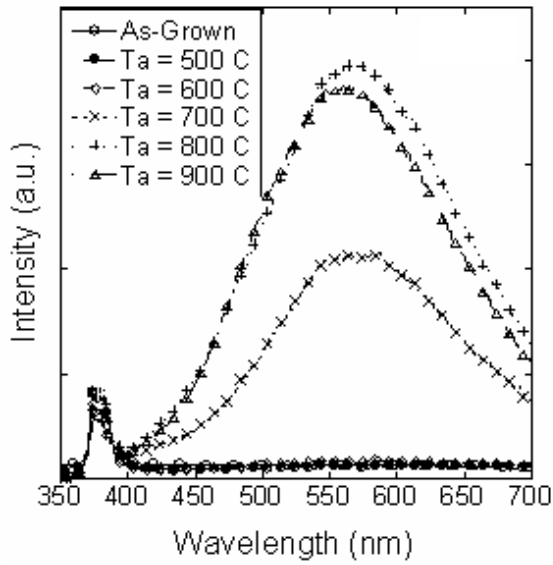


Figure 4-9. Mobility of ZnO films grown with A) pure O<sub>2</sub> B) O<sub>2</sub>/O<sub>3</sub> mixture gas as a function of the annealing temperature.



A



B

Figure 4-10. Room temperature PL spectra of ZnO films grown with A) pure  $O_2$  B)  $O_2/O_3$  mixture gas as a function of the annealing temperature.

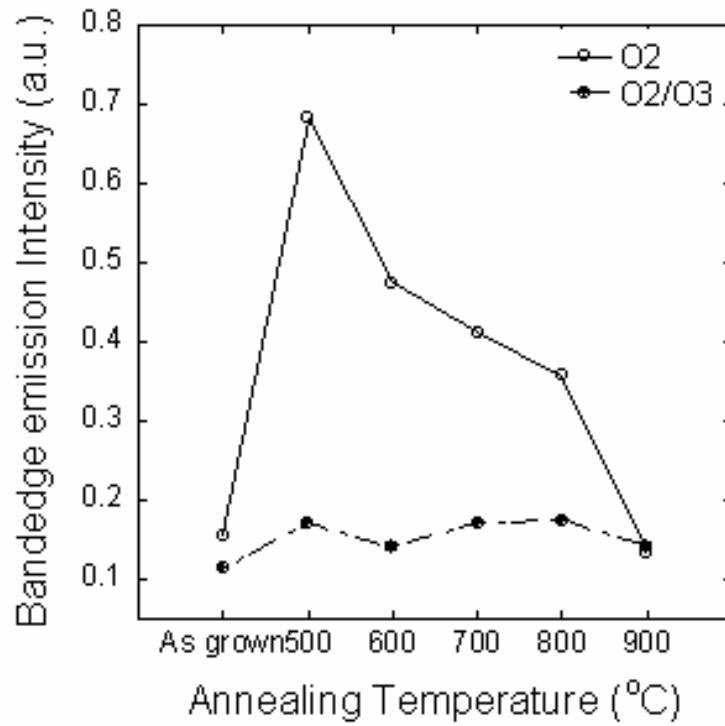


Figure 4-11. The intensity of bandedge emission of ZnO films grown with A) pure O<sub>2</sub> B) O<sub>2</sub>/O<sub>3</sub> mixture gas as a function of the annealing temperature.

CHAPTER 5  
ZINC OXIDE THIN FILMS GROWN WITH ZNO HOMO-BUFFER LAYER

**5. 1 Introduction**

In realizing optoelectronic applications, the synthesis of ZnO films with high crystalline quality is essential. While single crystal ZnO is commercially available, allowing for the growth of lattice-matched homoepitaxial ZnO thin films, these substrates are relatively expensive. As a result, several substrates have been investigated for ZnO heteroepitaxial growth. ScAlMgO<sub>4</sub> is nearly lattice-matched to ZnO, differing by only 0.09 %, but is expensive and unavailable as large area wafers [146]. High quality ZnO film growth has been reported on MgAl<sub>2</sub>O<sub>4</sub> (111) substrates by using a Mg wetting layer with radio frequency plasma-assisted molecular beam epitaxy [147]. However, the most widely used substrate for ZnO growth is sapphire due to its low cost and availability of large area wafers.

Sapphire presents an 18 % lattice mismatch with ZnO resulting in a high density of dislocations. There have been many reports using numerous techniques to facilitate heteroepitaxial ZnO thin film growth on sapphire. While a few studies report the growth of high-quality ZnO on sapphire without employing a buffer layer [148], most efforts to improve crystallinity and/or morphology employ some type of buffer layer. MgO buffer layers have been explored as the initial nucleation layer [122]. ZnO/MgO double buffer layers, annealed ZnO, and annealed ZnMgO buffer layers have also been used to improve ZnO film crystallinity even for the lattice-matched ScAlMgO<sub>4</sub> substrate [149-151]. Epitaxial GaN has also been used as a buffer layer in ZnO film growth due to its similar lattice constants with ZnO [152]. Several groups have reported on using ZnO, deposited at low growth temperatures, as a buffer layer to improve nucleation and film quality. With low temperature deposited ZnO buffer layers, morphology is improved but crystallinity can be relatively poor. Recently, Wang *et al.* reported an improvement

in the structural quality of heteroepitaxial ZnO films deposited by metal-organic chemical vapor deposition through the use of a high temperature deposited ZnO buffer layer [153]. The growth and annealing of a ZnO buffer layer at high temperature results in a large grain size by decreasing the density of nucleation sites and lowering the dislocation density [154]. The resulting full-width half-maximum (FWHM) of the x-ray diffraction (002) rocking curve was approximately 100 arcsec.

Buffer layer growth parameters play a key role in the properties of the subsequent epitaxial films. Although various buffer layers are often used for subsequent ZnO film growth, the effects of buffer growth parameters on the properties of the subsequent epitaxial layers is less studied. In this chapter, the effects of buffer layer growth conditions on subsequent ZnO film properties were examined. In these experiments, an O<sub>2</sub>/O<sub>3</sub> mixture gas was used as the oxidant source. The crystalline quality, surface morphology, and electrical properties of the ZnO thin films were examined when deposited on ZnO buffer layers deposited at various temperatures and pressures. In this study, a four-fold improvement in crystallinity for heteroepitaxial ZnO films on sapphire is reported through the use of a high temperature deposited ZnO buffer layer grown by pulsed laser deposition (PLD). The structural, optical and electrical properties, as well as the surface morphology of the ZnO films are reported.

## **5. 2 Experimental**

ZnO films were grown on sapphire (0001) using a range of buffer layer growth conditions. The buffer temperature was fixed at 850 °C when the buffer pressure was variable parameter. The buffer pressure was fixed at 1 mTorr when the buffer temperature was variable parameter. An ozone/oxygen gas mixture was used as an oxidation source. The gas mixture contained ~ 2-3% ozone. The growth technique was pulsed laser deposition. The ZnO target was prepared by

sintering high purity (99.99955 %) ZnO powders at 1000 °C for 12 hours in air. A KrF excimer laser was used for ablation. Laser frequency was 1 Hz for the buffer layer and 4 Hz for the epilayers; laser influence of approximately 1.5 J/cm<sup>2</sup>. The film structure consisted of a 25 nm ZnO buffer layer, followed by growth of a relatively thick (1 μm) ZnO film. The thick ZnO epitaxial layer was grown at 850 °C under an ozone/oxygen mixture with partial pressure of 10 mTorr. ZnO films were also grown without a buffer layer for comparison. The crystallinity of the films were examined via high resolution x-ray diffraction (HR-XRD) using a Philips MRD X'Pert system. The electrical properties were characterized via Hall measurements. Photoluminescence (PL) spectroscopy, using a He-Cd laser (λ = 325 nm) excitation source, was used to evaluate the optical properties of the ZnO films. The surface morphology was characterized with atomic force microscopy (AFM) in tapping mode.

## 5.3 Results and Discussion

### 5.3.1 Effects of Buffer Growth Parameters on the Properties of Heteroepitaxial ZnO Films

An AFM image for a ZnO film grown without a buffer layer is shown in Figure 5-1. The film grown without a buffer showed a highly crystallized large-grain morphology with hexagonal shaped crystal diameters on the order of 1 ~ 2 μm. The root-mean square (rms) roughness was approximately 80 nm. The use of a buffer layer has a significant impact on the subsequent ZnO layer morphology. Figure 5-2 shows AFM images for 1 μm thick ZnO films grown on ZnO buffer layers deposited at 1 mTorr and various buffer layer growth temperatures. Figure 5-3 shows the AFM images for 1 μm thick ZnO films grown on buffers deposited at 850°C in various O<sub>2</sub>/O<sub>3</sub> pressures. Using a ZnO buffer layer between the substrate and thick epitaxial layer reduced the size of hexagonal grains. The hexagonal grain size slightly increased as the buffer layer growth pressure was increased. The size of hexagonal grains was somewhat reduced for

films grown on buffers deposited at temperatures of 450-850°C. The dimensions of the hexagonal grains were similar for a range of buffer layer growth temperatures.

The RMS roughness values for the ZnO films are shown in Fig. 5-4. The RMS roughness was reduced by using a buffer for the buffer layer growth temperatures and pressures considered. However, the RMS values were not a strong function of the buffer layer growth temperature. The buffer layer growth pressure does affect the roughness rms values. The films are generally smoother with the buffer layer growth pressure less than or equal to 1 mTorr; the roughness increased as the buffer layer growth pressure increased above 10 mTorr. This indicates a higher density of nucleation sites for buffer layers deposited at lower pressure. This may also reflect the change in plume energetics within the ablation process. At lower pressure, the energy of ablated species will be higher due to fewer collisions with gas-phase molecules. It should also be noted that the growth rate used for the ZnO buffer layer was four times slower than that used for the subsequent 1  $\mu\text{m}$  thick film. This appears to have the most significant impact on final film morphology given that the temperature and pressure used for some of the buffers was quite similar to that used for the thick film growth.

The crystallinity of the ZnO films as a function of buffer layer growth conditions was also investigated. The full-width half-maximum (FWHM) of the XRD  $\omega$ -rocking curve for ZnO (002) is shown in Fig. 5-5. The FWHM values range from 33.12 to 242.64 arcsec. The FWHM for the films without a buffer layer was approximately 35 arcsec. All samples showed high crystallinity as reflected in out-of plane x-ray diffraction curves. These values are comparable to previous reports on ZnO films grown on lattice matched ScAlMgO<sub>4</sub> substrates [151]. Low buffer layer growth temperatures deteriorate the crystallinity and increases the FWHM values significantly as compared to films lacking a buffer layer. The FWHM decreases as the buffer temperature

increases. In general, increasing the buffer temperature decreases the nucleation site density and thus yields a larger grain size and improved crystallinity [153, 154]. There was a slight correlation between the grain size and crystallinity. Films grown without the buffer layer had large grains and the smallest rocking curve FWHM. Using a buffer at low temperature and pressure prevents the growth of large hexagonal crystals, improves morphology, but degrades the crystallinity. This is evident in the reduced roughness rms and surface morphology.

Figure 5-6 shows the carrier concentration and mobility of the ZnO films grown on buffer deposited at 850°C with different buffer layer growth pressures. Increasing the buffer pressure does not significantly affect the mobility. Note that all samples showed a higher mobility than the film grown without the buffer. The film grown without a ZnO buffer layer displayed a mobility of 74 cm<sup>2</sup>/V-s and carrier concentration of 1.65x10<sup>18</sup> cm<sup>-3</sup>. The carrier density did decrease with increasing buffer growth pressure. Figure 5-7 shows the carrier concentration and mobility for the ZnO films grown on buffers deposited at various temperatures. The mobility for the ZnO film grown with different buffer temperatures generally increased with the buffer deposition temperature. The carrier density did not show significant dependence on the buffer deposition temperature.

### **5.3.2 High Quality ZnO Films Using a High Temperature Deposited ZnO Buffer Layer**

The optimal film properties, as determined by crystallinity and morphology, were achieved by employing a 25 nm thick buffer layer on sapphire grown at 700 °C with the background oxygen pressure of 1 mTorr. The high deposition temperature yields good crystallinity. The low pressure yields good morphology. Growth conditions for the subsequent thick film can then be selected to optimize desired transport or photonic properties. For this study, a 1 μm ZnO epitaxial layer was then grown at 650 °C under oxygen partial pressure of 10 mTorr on this high

temperature deposited ZnO buffer layer. A ZnO film was also grown without a buffer layer for comparison. Figure 5-8 show the XRD  $\omega$ -rocking curve of the (0002) plane for the ZnO films on sapphire (001), comparing films grown with and without the high temperature ZnO buffer layer. Even for the ZnO film grown without a buffer layer, the FWHM of the XRD  $\omega$ -rocking curve for the (002) is relatively narrow ( $0.1146^\circ$ ). This is comparable to previous results reported for ZnO films grown using PLD [155]. When the high temperature deposited buffer layer was employed, the out-of-plane crystallinity of the ZnO film was remarkably improved. The FWHM of the XRD (002)  $\omega$ -rocking curve for the ZnO film was as narrow as 27.36 arcsec by inserting the buffer layer between the thick ZnO epilayer and sapphire substrate. It is worth noting that these ZnO films grown with this buffer on lattice mismatched sapphire substrates show comparable crystal quality to that reported for ZnO films grown on lattice matched  $\text{ScAlMgO}_4$  substrates, in which the XRD (002)  $\omega$ -rocking curve FWHM was 36 arcsec [151].

To investigate the in-plane crystallinity, in-plane  $\phi$ -scans through the ZnO (102) were performed. The XRD  $\phi$ -scans for the ZnO grown with and without the high temperature ZnO buffer are shown in Fig. 5-9. It shows well-aligned in-plane epitaxy, showing six-fold symmetry with a  $60^\circ$  separation for both cases. The FWHM of the  $\omega$ -rocking curve for the (102) reflection, seen in Fig. 5-10, is  $0.1242^\circ$  for ZnO film grown with the high temperature deposited ZnO buffer and  $0.2647^\circ$  for that grown without the buffer. The high temperature deposited ZnO buffer layer yields an improvement for in-plane and out-of-plane crystallinity. Note that the FWHM of the  $\omega$ -rocking curve through the ZnO (102) for the film grown with the high temperature deposited ZnO buffer was only reduced from  $0.2647^\circ$  to  $0.1242^\circ$ , while the out-of-plane ZnO (002) rocking curve FWHM was about 15 times narrower, decreasing from  $0.1146^\circ$  to  $0.0076^\circ$ . As discussed elsewhere [122], the FWHM of the  $\omega$ -rocking curve for ZnO (002) is largely determined by

screw dislocations with a Burgers vector  $b=[001]$ , while that of (102) results from edge dislocations. The high temperature deposited ZnO buffer layer appears to decrease these types of screw dislocations.

We also examined the electrical and optical properties of ZnO films grown with and without the high temperature deposited ZnO buffer. The Hall data are shown in Table 5.1. The resistivity of the ZnO film grown with the high temperature deposited ZnO buffer increased from 0.7078 ohm-cm to 3.1217 ohm-cm. This can be attributed to improved stoichiometry and a reduction in defects by using a high temperature deposited ZnO buffer. The residual donor density is reduced one order of magnitude by using the high temperature deposited ZnO buffer layer as compared to the ZnO film grown without the buffer. In addition, the ZnO film grown with the high temperature deposited ZnO buffer layer shows a high mobility of  $87.68 \text{ cm}^2/\text{V}\cdot\text{s}$ , which is about three times higher than that of the ZnO film grown without the buffer layer. This improved mobility reflects a reduction in defects that affects carrier transport by scattering. As a result, we can conclude that the buffer layer remarkably improves the properties of the ZnO film.

The room temperature photoluminescence (PL) spectra of ZnO films grown with and without a high temperature deposited ZnO buffer layer is shown in Fig. 5-11 A) and B), respectively. The defect related visible emission was reduced by using the high temperature deposited ZnO buffer layer. In addition, the PL peak for the ZnO film grown by using the high temperature deposited ZnO buffer layer was shifted to higher energy. This is probably due to the improvement of optical properties by eliminating non-radiative defect levels near the band edge. Interestingly, both near-band edge peaks for ZnO film grown with and without the buffer showed additional structure at slightly longer wavelength. The ZnO films grown by using the high temperature deposited ZnO buffer layer showed peaks at 3.3155, 3.2546, 3.2112, and 3.1234 eV.

These peaks are tentatively attributed to the free excitons and their phonon replicas [156], although these features are rarely seen in room temperature PL for ZnO [157].

The surface morphology of the ZnO films was examined by atomic force microscopy (AFM) as shown in Fig. 5-12. The root mean square (RMS) surface roughness was measured to be 47.8 nm and 1.55 nm for ZnO films grown without and with the high temperature deposited ZnO buffer, respectively. Also, the ZnO film grown with a high temperature deposited ZnO buffer showed well-defined 1  $\mu\text{m}$  diameter size hexagonal crystals on the surface. These hexagonal columns contribute to a high degree of crystallinity in the film.

#### **5. 4 Summary**

ZnO films were grown on sapphire (0001) with different ZnO buffer deposition temperatures and pressures. The buffer layer improved the surface roughness regardless of the buffer temperatures and pressures. In particular, the change of the buffer growth pressure affects on the roughness more sensitively than the buffer growth temperature. Using a buffer layer grown at low deposition temperature deteriorated the crystallinity. The change of the buffer temperature did affect the electrical properties of the ZnO films more than changes in the buffer deposition pressures. In optimal buffer growth condition, highly crystalline ZnO films were realized on lattice-mismatched sapphire substrate by using a thin high temperature deposited ZnO buffer layer. The FWHM of the  $\omega$ -rocking curve was 27.36 arcsec and 447.12 arcsec for ZnO (002) and (102), respectively. This result is among the best reported for ZnO heteroepitaxial films. The films showed room temperature mobility of 87.68  $\text{cm}^2/\text{V}\cdot\text{s}$  and strong near bandedge emission with very weak defect related visible emission. In addition, the film RMS roughness was only 1.55 nm by using the high temperature deposited ZnO buffer layer.

Table 5-1. Hall data of ZnO films grown with and without a high temperature deposited ZnO buffer layer.

	Resistivity (ohm-cm)	Carrier density (/cm <sup>3</sup> )	Mobility (cm <sup>2</sup> /v-s)
Without buffer	0.7078	$2.50 \times 10^{17}$	35.98
With buffer	3.1217	$2.40 \times 10^{16}$	87.68

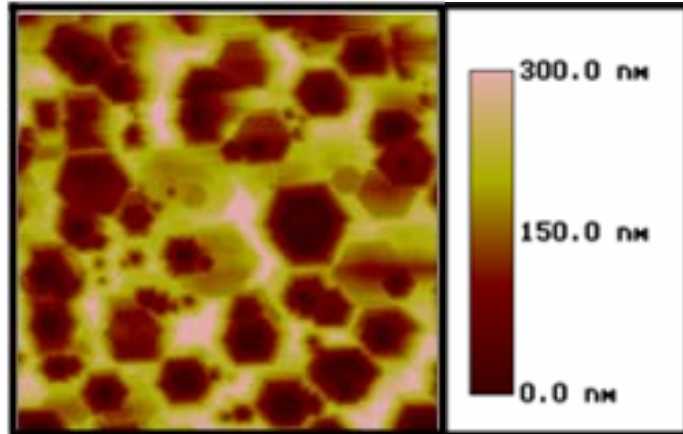


Figure 5-1. Atomic force microscopy image of a 1  $\mu\text{m}$  thick ZnO films grown on (0001) sapphire at 850°C and 10 mTorr without the use of a nucleating buffer layer. The scanned image size is 10 x 10  $\mu\text{m}^2$ .

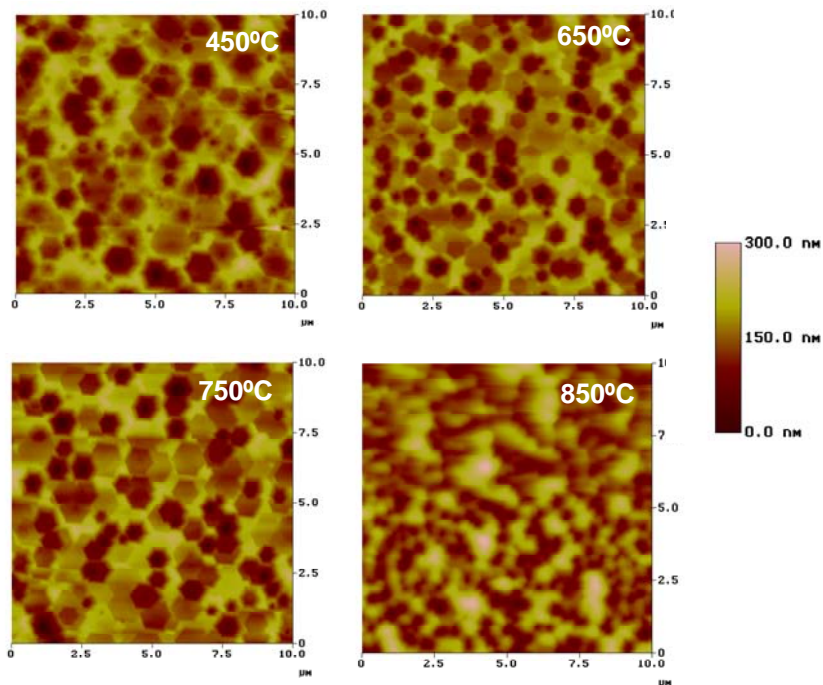


Figure 5-2. Atomic force microscopy image of 1  $\mu\text{m}$  thick ZnO films deposited on (0001) sapphire at 850°C and 10 mTorr in which a nucleating ZnO buffer layer deposited in 1 mTorr  $\text{O}_2/\text{O}_3$  was employed with different buffer growth temperatures. The scanned image size is 10 x 10  $\mu\text{m}^2$ .

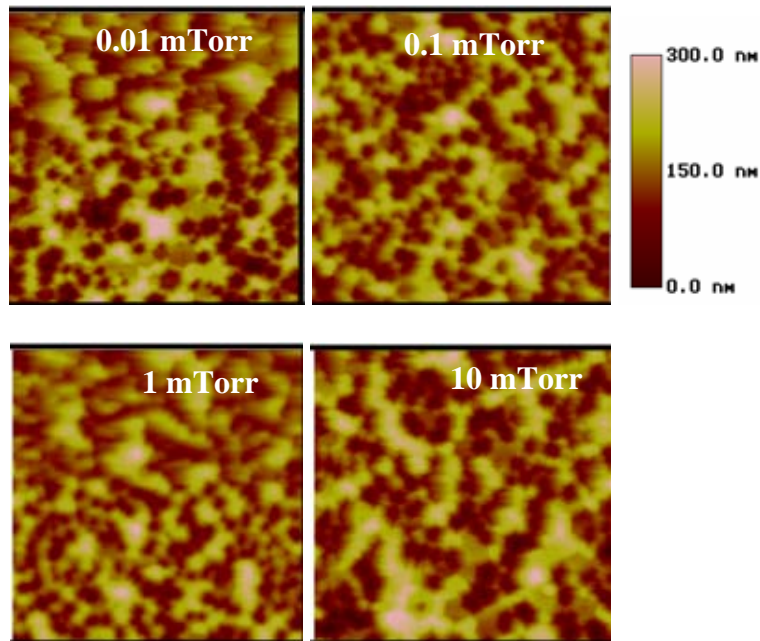
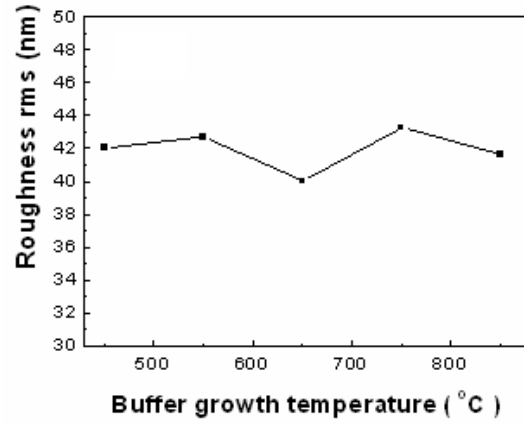
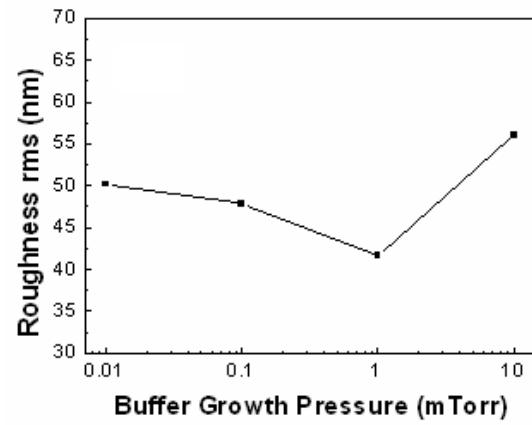


Figure 5-3. Atomic force microscopy image of 1  $\mu\text{m}$  thick ZnO films deposited on (0001) sapphire at 850°C and 10 mTorr in which a nucleating ZnO buffer layer deposited at 850°C was employed with different buffer growth  $\text{O}_2/\text{O}_3$  pressures. The scanned image size is 10 x 10  $\mu\text{m}^2$ .

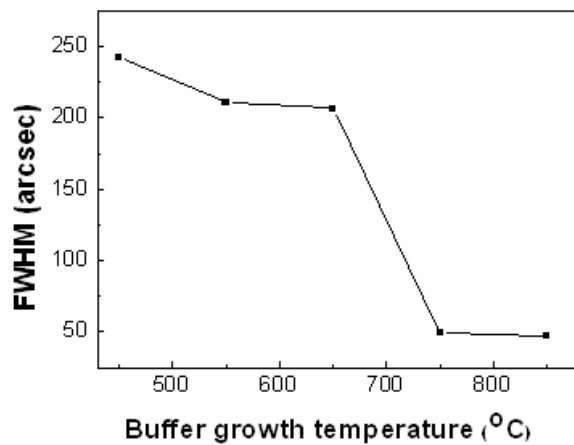


A

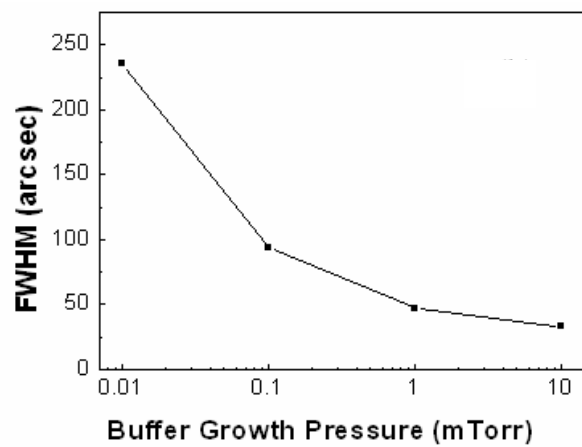


B

Figure 5-4. RMS roughness of 1  $\mu\text{m}$  thick ZnO films grown A) at 1 mTorr with different buffer growth temperatures or B) at 850°C with different buffer growth pressures.

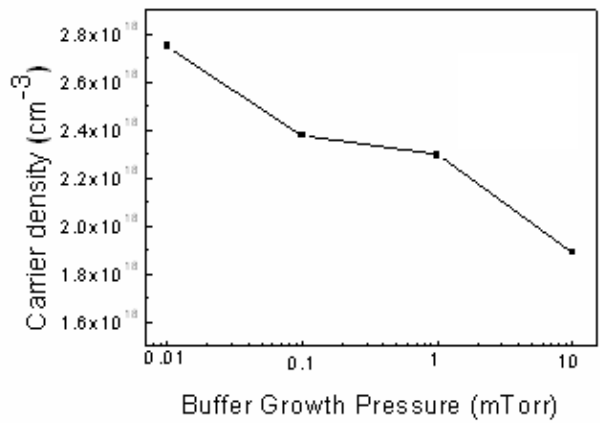


A

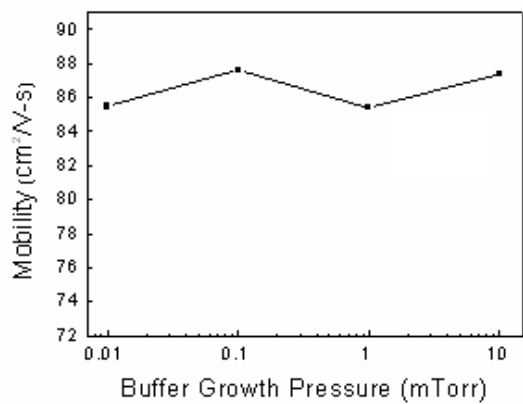


B

Figure 5-5. FWHM of  $\omega$ -rocking curves of the ZnO (002) of 1  $\mu\text{m}$  thick ZnO films grown A) at 1 mTorr with different buffer growth temperatures or B) at 850°C with different buffer growth pressures.

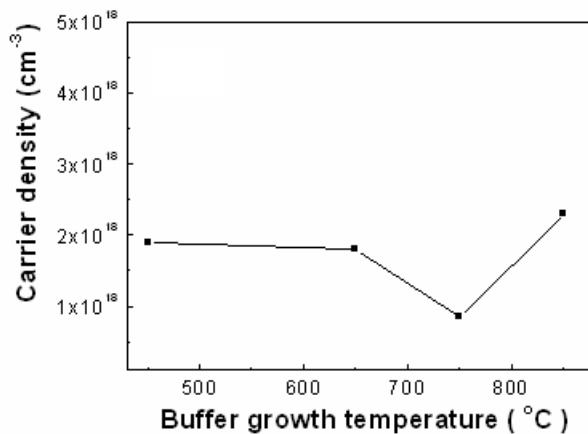


A

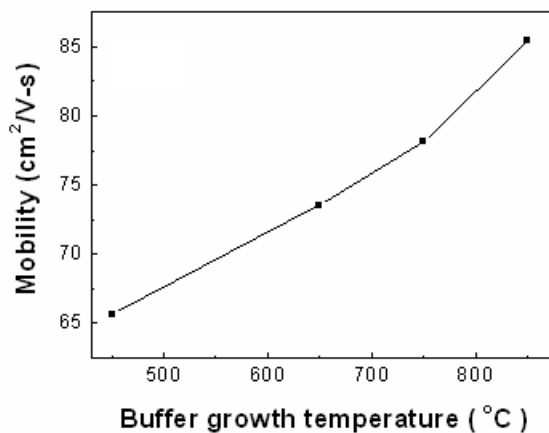


B

Figure 5-6. Plots of A) carrier concentration and B) mobility for 1  $\mu\text{m}$  thick ZnO films deposited on (0001) sapphire at 850°C and 10 mTorr in which a nucleating ZnO buffer layer deposited at 850°C was employed with different buffer growth  $\text{O}_2/\text{O}_3$  pressures.

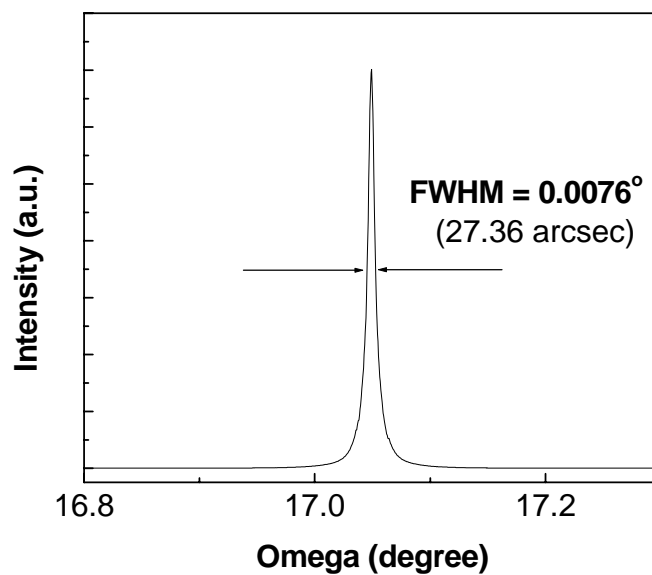


A

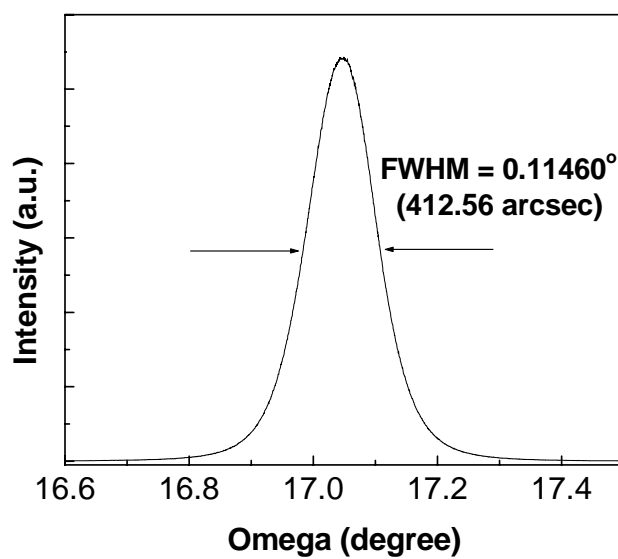


B

Figure 5-7. Plots of A) carrier concentration and B) mobility for 1  $\mu\text{m}$  thick ZnO films deposited on (0001) sapphire at 850°C and 10 mTorr in which a nucleating ZnO buffer layer deposited in 1 mTorr  $\text{O}_2/\text{O}_3$  was employed with different buffer growth temperatures.

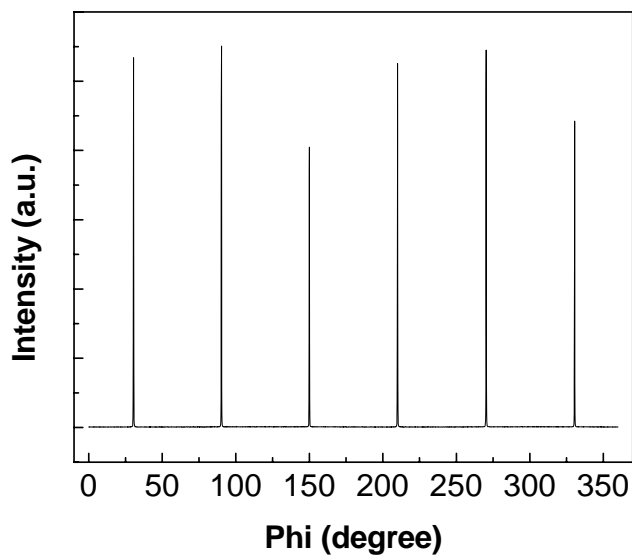


A

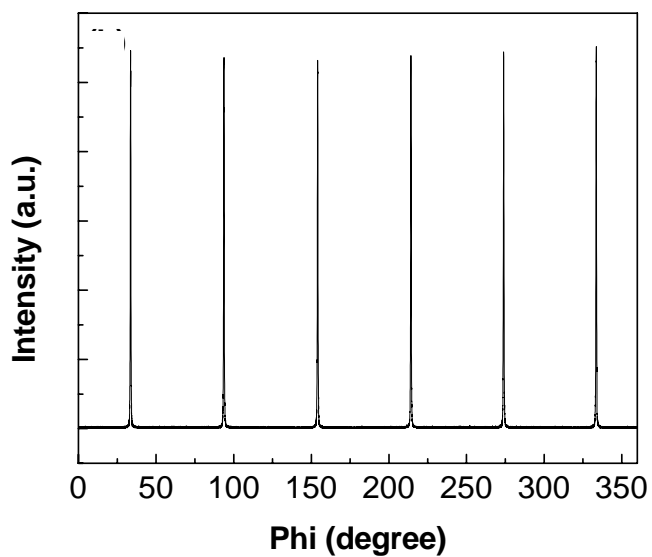


B

Figure 5-8. XRD  $\omega$ -rocking curves of ZnO (002) grown A) with and B) without a high temperature deposited ZnO buffer.

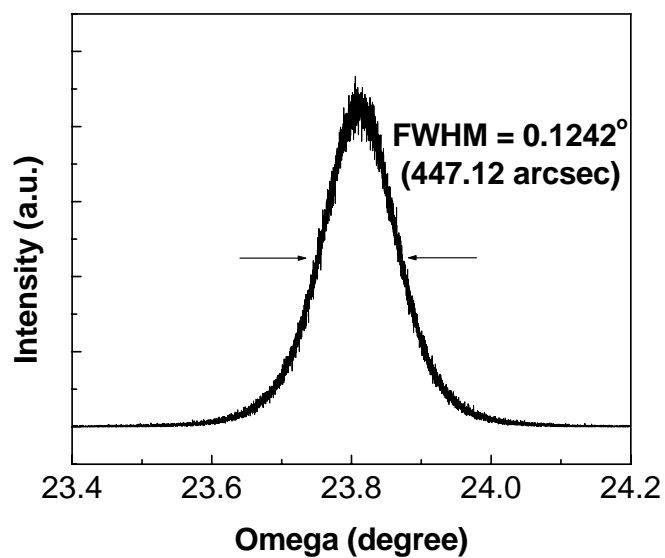


A

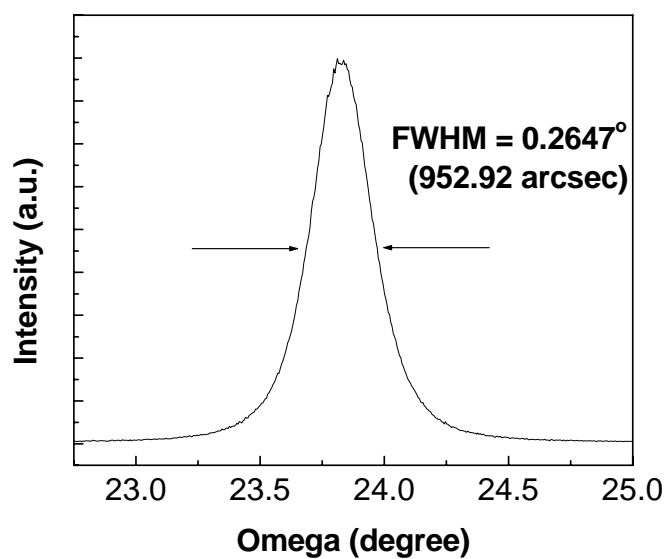


B

Figure 5-9. XRD phi scan of ZnO (102) grown A) with and B) without a high temperature deposited ZnO buffer.

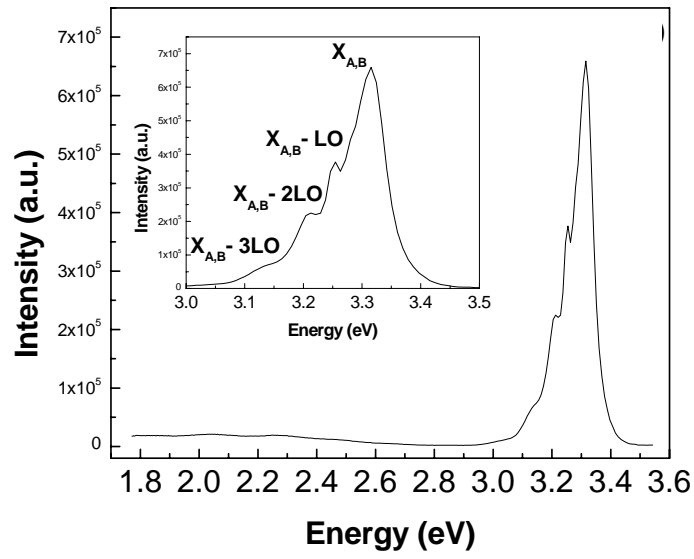


A

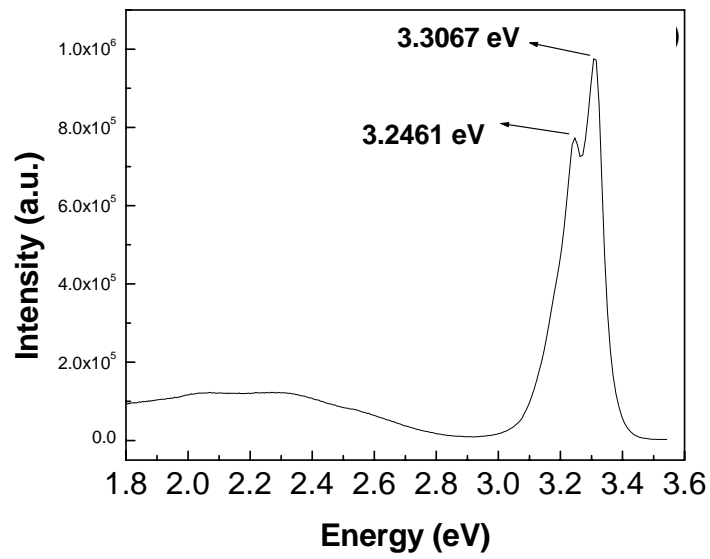


B

Figure 5-10. XRD  $\omega$ -rocking curves of ZnO (102) grown A) with and B) without a high temperature deposited ZnO buffer.

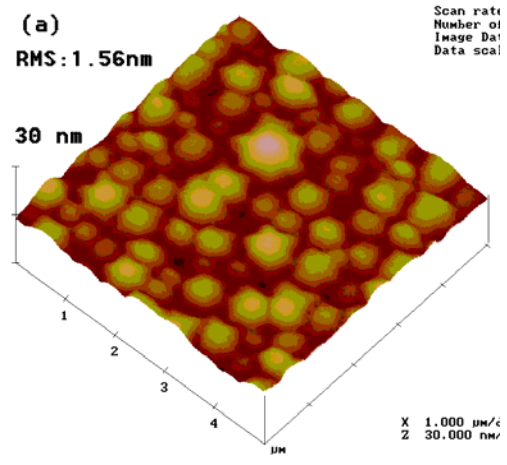


A

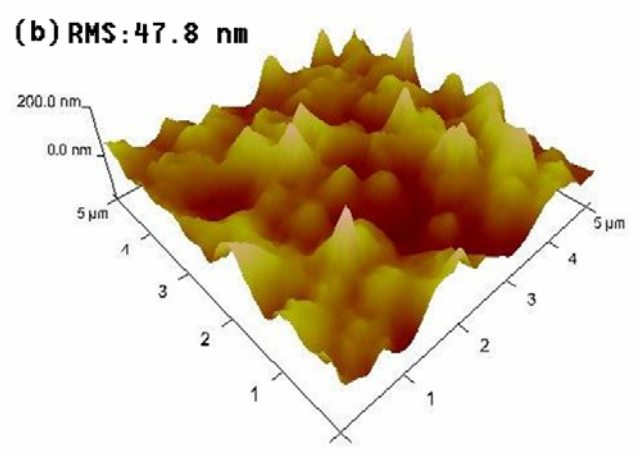


B

Figure 5-11. PL spectra of ZnO films grown A) with and B) without a high temperature deposited ZnO buffer at room temperature.



A



B

Figure 5-12. AFM images of ZnO films grown A) with and B) without a high temperature deposited ZnO buffer in 5 x 5  $\mu\text{m}^2$ .

## CHAPTER 6 PHOSPHORUS DOPED ZNO AND ZNMGO THIN FILMS

### 6. 1 Introduction

The most challenge issue in device processing, particularly for ZnO-based light emitters, is the formation of p-type ZnO. Achieving p-type ZnO is difficult due to the relatively deep location of the ZnO valence band as well as self-compensation effect from native donor defects such as oxygen vacancies ( $V_O$ ), zinc interstitials ( $Zn_i$ ), and hydrogen, the latter of which can easily diffuse into ZnO at moderate temperatures [18,19,27,101, 102]. This difficulty in realizing p-type ZnO has hindered efforts to realize robust pn junction devices. As such, the formation of p-type ZnO has been a topic of intense investigation for several years [158]. Recently, there have been several reports of electroluminescence from ZnO-based LED structures [8-11,159], providing proof-of-concept demonstrations for ZnO materials in light emitting applications. However, the stability and reproducibility of p-type ZnO, as well as the behavior of specific candidate dopants, remain open questions. Reliable and reproducible p-type ZnO synthesis represents a significant impediment to realizing practical applications of optoelectronic devices based on ZnO materials.

By far, the most studied dopants are the group V anions [160], motivated by the obvious opportunity to hole dope via substituting -3 anions for the -2 oxygen sites. Unfortunately, theoretical arguments suggest that substituting Sb, As, or P on the oxygen site should yield deep acceptors rather than shallow levels and thus may be inefficient in contributing to p-type conduction [26, 27]. The principle driver for this is size mismatch. For example, the ionic radius of phosphorus (2.12 Å) is significantly larger than that for oxygen (1.38 Å). Due to this large size mismatch, these group V anions are predicted to favor antisite defects to alleviate lattice strain and the antisite defects are acceptor-compensating donors [28]. Despite these apparent

limitations, there have been multiple reports of p-type ZnO doping with phosphorus [59, 60, 109, 141, 161], realizing both rectifying [162] and light-emitting [11] junctions. Theoretical studies suggest that these anions may act as acceptors, not through substitution on the oxygen site, but by forming an antisite complex (e.g.  $P_{Zn}-2V_{Zn}$ ) [63, 64]. Obviously, for P, As, and Sb, there are open questions regarding the specific doping mechanism as well as processing conditions necessary to activate the acceptor states.

The epitaxial growth and properties of doped and undoped (Zn,Mg)O, (Zn,Cd)O, and (Zn,Be)O alloys is an important element in realizing heterojunctions and multiple quantum well structures for efficient carrier confinement and injection. Many groups have studied transport in (Zn,Mg)O/ZnO pn heterostructures [105, 106, 163, 164]. Heterojunction devices with a n-(Zn,Mg)O/ZnO/p-(Zn,Mg)O structure was reported using N-In co-doped ZnMgO [107]. Ye *et al.* reported p-type (Zn,Mg)O thin films codoped with Al and N deposited by magnetron sputtering [108]. P-type conductivity in (Zn,Mg)O films has been reported using P or Li as the acceptor dopant [109, 110].

In this chapter, the behavior of P in ZnO is examined, in particular characterizing the effect of processing on the transport properties for ZnO:P films grown by pulsed laser deposition, followed by rapid thermal annealing. Focus is given to understanding the sensitivity of carrier-type conversion on deposition and annealing conditions for post-annealed P-doped ZnO films. The film properties are used to extrapolate the behavior of the phosphorus dopant in the process-dependent creation of effective acceptor states. In addition, the growth and properties of phosphorus-doped  $Zn_{1-x}Mg_xO:P$  ( $x = 0.05, 0.10$ ) films deposited by pulsed laser deposition is discussed, focusing on the influence of Zn/Mg ration and post-growth annealing on transport.

For phosphorus-doped ZnO films (no Mg), the use of post-growth annealing is critical to activation of the phosphorus dopant as an acceptor.

## 6. 2 Experimental

### 6.2.1 Phosphorus Doped ZnO

The ZnO:P films were grown on sapphire (0001) by pulsed laser deposition at substrate temperatures in the range of 500~800 °C in an oxygen partial pressure of 30-150 mTorr, followed by post thermal annealing at temperatures ranging from 500 to 950 °C under oxygen ambient. Prior to ZnO:P deposition, an undoped ZnO buffer layer was deposited on the sapphire at 400°C in 20 mTorr. This served as a nucleation layer for ZnO:P growth, greatly improving surface morphology and reproducibility in the transport properties. The buffer layer was annealed at 650 °C in an oxygen ambient prior to ZnO:P deposition. This pre-anneal increased the resistivity of the buffer layer, thus decreasing its impact on the subsequent Hall measurements of the ZnO:P films. Phosphorus-doped ZnO targets were fabricated using high purity (99.9995 %) ZnO mixed with P<sub>2</sub>O<sub>5</sub> (99.998 %) as the doping agent. The targets were sintered at 1000 °C for 12 h in air. The phosphorus doping levels chosen for this study were 0.5 and 1 at %. The target was ablated by a KrF excimer laser with the laser frequency of 1 Hz and energy density of approximately 1.5 J/cm<sup>2</sup>. The film thickness was approximately 400 nm for the ZnO:P layer and 100 nm for the undoped ZnO buffer layer. The room temperature electrical properties were investigated by Hall measurements using the four-point van der Pauw method with a commercial LakeShore Hall measurement system. In order to minimize the influence of persistent photoconductivity often seen in acceptor-doped ZnO [93], the samples were maintained in the dark for 12 h prior to Hall measurements. Typical room-temperature decay

times for persistent photoconductivity in P-doped ZnO can be on the order of  $10^4$  seconds as reported elsewhere [93]. The magnetic field strength ranged from  $-1$  tesla to  $+1$  tesla.

### **6.2.2 Phosphorus Doped $Zn_{1-x}Mg_xO$**

The (Zn,Mg)O:P films were grown on c-plane sapphire by pulsed laser deposition. The  $Zn_{1-x}Mg_xO:P$  ( $x = 0.05, 0.10$ ) targets were fabricated by sintering high purity ZnO (99.99955 %), MgO (99.998 %), and  $P_2O_5$  (99.998 %) powders. The concentration of phosphorus in the targets was 2 at %. A KrF excimer laser was utilized as the ablation source. The repetition rate was 1 Hz; laser fluence was approximately  $1.5 \text{ J/cm}^2$ . A 100 nm undoped ZnO buffer layer was first deposited on the sapphire substrate at  $400 \text{ }^\circ\text{C}$  in 20 mTorr oxygen prior to growth of 400 nm thick (Zn,Mg)O:P films. The substrate temperature was varied from 550 to  $650 \text{ }^\circ\text{C}$ . The growth pressure was 150 mTorr oxygen. After growth, rapid thermal annealing (RTA) was performed at  $600 \sim 900 \text{ }^\circ\text{C}$  under 1 atm oxygen ambient. The duration of the RTA anneal was 3 minutes. X-ray diffraction was used to examine the crystallinity of the (Zn,Mg)O:P films. The electrical properties were investigated by Hall measurements using a LakeShore Hall measurement system. Room temperature photoluminescence measurements were performed to investigate the optical properties of the films.

## **6.3 Results and Discussion**

### **6.3.1 Behavior of Rapid Thermal Annealed ZnO:P films**

Experimental efforts examined the structural and transport properties of as-deposited and post-annealed ZnO films doped with 0.5 and 1.0 at.% phosphorus. In general, phosphorus doping at the high concentrations considered in this study leads to a degradation in crystalline quality of the epitaxial films. Figure 6-1 shows the X-ray diffraction rocking curves for ZnO films that are undoped, as well as doped with 0.5 and 1.0 at.% P. These films were grown at

700°C in 150 mTorr oxygen, using the same ZnO buffer nucleation layer as described earlier. The rocking curve full-width half-maximum (FWHM) was 0.80° for the undoped film, 1.79° for 0.5 at.% P, and 3.21° for the film doped with 1 at.% P. This large increase in the x-ray diffraction rocking curve with P doping indicates a high density of defects and lattice strain associated with high phosphorus doping. Based on these results, one might anticipate superior semiconductor material properties in the 0.5 at.% P-doped material as compared to the 1.0 at.% P-doped ZnO. As will be seen, the results for the 0.5 at.% P-doped films were more systematic. As such, the majority of the discussion will center on the behavior of the 0.5 at.% P-doped films. However, the results for the 1.0 at.% P-doped ZnO films will also be presented for comparison.

The processing window for achieving p-type conduction in P-doped ZnO films was relatively narrow, requiring high temperature in situ growth followed by rapid thermal annealing (RTA) treatment. Before examining the specific conditions for p-type conversion, it is useful to consider the generic behavior of the P-doped ZnO thin films. First, the as-deposited ZnO:P films were n-type, with electron concentrations ranging from  $10^{17}$  to  $10^{19}$  cm<sup>-3</sup> depending on the deposition temperature, pressure, and phosphorus concentration [141]. Figure 6-2 shows the carrier density of the as-grown ZnO:P films that were deposited at different substrate temperatures and phosphorus doping levels. All as-deposited samples show n-type conductivity regardless of the growth temperature and phosphorus doping level [165]. For the growth conditions selected, the 1 at% phosphorus-doped ZnO films generally showed lower donor density as compared to the 0.5 at% phosphorus-doped ZnO films. The lowest donor density for the as-deposited films in Fig. 6-2 was  $1.1 \times 10^{17}$  /cm<sup>3</sup>, observed for the 1 at.% P doped film grown at 600 °C. The n-type conductivity of as-grown P-doped films reflects an amphoteric doping behavior for phosphorus in ZnO in yielding either donor or acceptor states. The dominant

P-related donor is assumed to be the  $P_{Zn}$  antisite defect. Previous work on P-doped ZnO films as-grown at moderate temperatures showed a slight decrease in d-spacing with phosphorus doping [141]. Substitution of a large anion (phosphorus) on the smaller oxygen site should yield an increase in lattice spacing. The observed decrease in lattice spacing is inconsistent with substitution on the O site, but suggestive of an alternative location for the P, possibly as an antisite  $P_{Zn}$  defect. This would be consistent with these films being n-type, given that  $P_{Zn}$  is presumed to be a donor, albeit relatively deep. Note that these films were deposited in relatively O-rich (oxygen pressure equals 150 mTorr) growth condition. The formation of zinc vacancies and oxygen interstitials is also possible based on their estimated formation energy in O-rich conditions [135] even though residual and antisite donor defects are dominant in transport.

Regarding the P-related defects, both P-related donors ( $P_{Zn}$  and  $P_{Zn}-V_{Zn}$ ) and acceptors ( $P_{Zn}-2V_{Zn}$  complex and  $P_O$ ) appear to coexist, with their relative ratio likely dependent on the growth conditions and its effect on the amphoteric nature of phosphorus [28,64,166]. The coexistence of donor and acceptor states associated with phosphorus doping is consistent with the low-temperature photoluminescence (PL) data shown in Figure 6-3 for a P-doped ZnO films. In this case, the P-doped ZnO sample was shown to be n-type via Hall effect measurements, yet displayed a PL peak that has previously been attributed to an acceptor state in group-V doped ZnO materials. One also might expect that the oxygen rich growth conditions used in this study would suppress the formation of  $P_O$  and promote the generation of anti-site  $P_{Zn}$  donors [166]. The anti-site  $P_{Zn}$  defects could combine with a double acceptor,  $V_{Zn}$ , which is a favorable native defect in O-rich growth condition, and generate  $P_{Zn}-2V_{Zn}$  complexes. This complex is predicted to be a shallow acceptor. The lower carrier density seen in the 1 at.% P doped film (as compared to the 0.5 at.%) suggests a higher density of acceptors. (e.g.  $P_O$  or  $P_{Zn}-2V_{Zn}$ ) yielding a lower

donor density. Note that the low temperature growth also yields an O-rich growth condition by suppressing oxygen liberation.

Returning to the data in Figure 6-2, it is interesting to consider the inflection in both resistivity and carrier density at a growth temperature of 650-700°C. For the sample doped with 0.5 at.% P, the electron carrier density initially increases, then steadily decreases with increasing growth temperature. This might be explained in one of two ways. First, the increased growth temperature may initiate the generation of compensating acceptor states ( $P_O$  or  $P_{Zn}-2V_{Zn}$ ), thus yielding a decrease in electron concentration. Alternatively, the decrease in electron concentration could reflect a reduction in overall P content (and associated donors) due to P evaporation. However, this second possibility would not explain the lower electron density observed for the 1 at.% P-doped ZnO films grown under identical conditions. Thus, the most logical explanation is that, at  $T \geq 650^\circ\text{C}$ , acceptor states are generated with increasing density relative to the donor concentration that dominates transport for films grown at lower temperature. Note that, in previous work involving P-doped films grown at lower temperatures, higher P concentrations yielded higher donor density. Annealing at higher temperature in  $O_2$  resulted in a significant decrease in donor concentration. In the present study, increasing the growth temperature to  $700^\circ\text{C}$  decreases the donor density. This suggests that, at temperatures higher than  $700^\circ\text{C}$ , the formation of acceptor states become a significant contribution for P-doped ZnO. This could involve P substitution on the oxygen site, or formation of  $P_{Zn}-2V_{Zn}$  complexes, as has been theoretically predicted. In either case, the results suggest that donors (perhaps  $P_{Zn}$ ) are predominantly formed at the growth temperature of  $600^\circ\text{C}$ , while acceptor formation ( $P_O$  or  $P_{Zn}-2V_{Zn}$ ) is observed at  $700^\circ\text{C}$  or higher.

While there is evidence for acceptor formation for growth above 700 °C, it is interesting to note that the donor density of 1 at% phosphorus-doped ZnO films generally increases with the growth temperature while that of 0.5 at% phosphorus-doped ZnO films decreases. This may reflect a segregation of phosphorus for high deposition temperature and higher phosphorus doping level. Indirect evidence for phosphorus segregation at the higher temperatures can be seen in the atomic force microscopy (AFM) images shown in Fig. 6-4, where a significant modification in surface morphology is observed for the P-doped ZnO film grown at 800°C as compared to 650°C. In the high temperature region, there will be a competition between the formation of  $P_O$  or  $P_{Zn-2V_{Zn}}$  acceptors, the formation of  $P_{Zn-V_{Zn}}$ ,  $P_{Zn}$ , and/or native defect donor states, and segregation of phosphorus. The carrier type and density of the phosphorus-doped ZnO is determined by both native defects and amphoteric phosphorus doping behavior.

For growth in the temperature range of 500-800°C, and oxygen pressure range of 1-150 mTorr, all ZnO:P films examined in this study were n-type. However, p-type conversion of the as-deposited P-doped ZnO films was achieved via post-growth annealing. First note that the effects of post-growth annealing depend on whether the anneal is steady-state (furnace anneal) or short transient (rapid thermal annealing). As reported earlier, steady state annealing of ZnO:P in oxygen yielded an increase in resistivity without conversion to p-type, often resulting in semi-insulating behavior. In contrast, a short (2-3 min) rapid thermal anneal (RTA) in oxygen could produce a decrease in resistivity and conversion to p-type conduction. First consider the generic behavior of P-doped ZnO subjected to an RTA anneal. Figure 6-5 shows the generic behavior for ZnO:P films subjected to a 2 min oxygen anneal at various temperatures. These 0.5 at.% P-doped ZnO films were grown at 700°C in 50 or 150 mTorr  $O_2$ . Note that, for the sample set in figure 6-5, most of these films remained n-type and did not show conversion with annealing, due

largely to experimental uncertainty in the thermal transients for the particular RTA system employed. Nevertheless, the overall behavior of the films considered in Figure 6-5 is instructive. First, the initial increase in resistivity with rapid thermal annealing in 1 atm O<sub>2</sub> likely reflects a decrease in surface conductivity and/or oxygen vacancy-related defects associated with cooling the as-grown films in low (50-150 mTorr) oxygen pressure. Note, however, that an inflection in the resistivity ( and carrier concentration) with annealing temperature is observed for both sample sets. This behavior is typical for a compensated semiconductor in which the relative ratio of activated donor and acceptors is changing with annealing temperature. Again, for films considered in Figure 6-5, type conversion was not observed for most samples. However, the annealing temperature dependence of resistivity with RTA treatment was common to P-doped ZnO films subjected to annealing. It is also interesting to note that the inflections in resistivity and carrier concentration for these annealed P-doped ZnO films in the temperature range of 800-950°C is similar in nature to the inflection seen in the as-grown films for the growth temperature range of 600-750°C as discussed for Fig. 6-2. This is consistent with a model in lower temperature processing favors P-related donor formation, while high temperatures activate P-related acceptor states. The fact that this behavior is observed at lower temperatures for epitaxial films as compared to post-annealed activation is not unexpected, given that crystallization in epitaxy occurs on a free surface.

Through improved control of thermal transients during the annealing cycles, p-type conversion was achieved via post-growth rapid thermal annealing. Table 6-1 shows the Hall measurement results for a series of 0.5 at.% P-doped films deposited in 150 mTorr at various substrate growth temperatures, then RTA annealed in oxygen for the temperature range 850~ 950 °C. Table 6-2 shows similar results for the 1 at.% P-doped ZnO. Interestingly, for the 0.5 at.% P

doped films, only the films grown at 700-750 °C showed reproducible p-type conversion upon annealing, while the samples grown at other temperatures generally remained n-type even after the thermal annealing process. Figure 6-6 shows the resistivity and carrier density as a function of annealing temperature for the 0.5 and 1.0 at.% P-doped ZnO films, along with an undoped film for comparison. First note that an RTA peak temperature at or above 900 °C was needed in order to achieve p-type conversion. Second, note that the resistivity remained relatively high for samples annealed at 850 °C, a temperature just below that needed for p-type conversion. Most importantly, the background electron density remained low enough such that type conversion with moderate hole concentrations was possible. Also note that large changes in carrier density were not observed for the undoped ZnO film subjected to the same annealing cycle.

The mobility of the ZnO:P films was also determined. For 0.5 and 1.0 at.% doping levels, the mobility decreases until type conversion occurs. It increases again after converting to p-type. The ZnO:P films grown with a higher P contents shows a higher mobility over the entire range. In general, p-type ZnO:P films have a low carrier mobility, typically less than 1 cm<sup>2</sup>/V-s.

Given the multi-carrier type conductance due to the presence of compensating donors and acceptors, along with the low carrier mobility for holes in P-doped ZnO, it is useful to examine the actual Hall voltages used to extract carrier type and density. For these samples, the Hall measurements were performed at multiple magnetic field, namely 2000, 4000, 6000, 8000, and 10,000 Gauss. As a reminder, Hall measurements using a van der Pauw method are performed using a four-point configuration (illustrated in inset for Fig. 6-7) in which current is passed through one sample diagonal (e.g contacts 1 and 3) with voltage measured across the transverse diagonal (contacts 2 and 4) while simultaneously applying a magnetic field perpendicular to the sample surface. The same measurement is then made for the same current/voltage configuration

but with the magnetic field reversed. The Hall voltage can then be distinguished from other signal sources (noise, offset, magnetoresistance) by taking the difference between the two measurements described above. The van der Pauw approach involves extracting the magnetic field dependent voltage difference for the two possible voltage contact choices along with the two possible current polarities. Thus, a van der Pauw measurement generates four voltage-pair differences, each of which indicates the carrier type based on the sign of the voltage difference. Figure 6-7 shows a plot of these four voltage pairs for the 0.5 at.% P-doped ZnO film grown at 700°C in 150 mTorr oxygen, followed by rapid thermal annealing at 900°C. The voltage pair polarities were selected such that a positive voltage difference indicates p-type, a negative voltage difference n-type. For measurements taken at the five magnetic fields considered, all voltage pairs for this sample are consistent with p-type majority carrier conduction. This was routinely seen for samples reported as being p-type in this study.

In examining the Hall data in Tables 6-1 and 6-2 for the 0.5 and 1.0 at.% P-doped films, it becomes apparent that the results for the 1.0 at.% P-doped films are less systematic with higher variability in the measured parameters as compared to the 0.5 at.% samples. As mentioned earlier, the x-ray diffraction results indicate that the 1.0 at.% P-doped samples are highly defective as compared to the 0.5 at.% P-doped films. This is also reflected in the room temperature photoluminescence data for RTA processed, p-type ZnO:P films. The room temperature photoluminescence characteristics for the RTA annealed p-type films are shown in Fig. 6-8. The photoluminescence for the 1 at.% P-doped sample shows a near band edge emission with significant visible emission commonly attributed to defects. The film with 0.5 at.% P shows significantly higher intensity at the near band edge emission with little mid-gap emission. Clearly, the semiconducting properties are better for lower P concentrations.

Given the results presented in this study, it is possible to postulate on the specific defect structures that yield n-type behavior in the as-grown films, while yielding p-type conduction upon annealing. In previous studies, Kim *et al.* have also reported carrier type conversion in sputter deposited ZnO:P films by using rapid thermal annealing [36]. Hwang *et al.* claimed that phosphorus atoms act as an acceptor by occupying oxygen sites in the ZnO during the RTA process [167]. However, the  $P_O$  acceptor is predicted to be deep while the  $P_{Zn}-2V_{Zn}$  complex is predicted to have a low formation energy and act as a shallow acceptor [63, 64]. Furthermore, the O-rich growth and annealing conditions used in the present study should favor  $P_{Zn}-2V_{Zn}$  formation and suppress the formation of  $P_O$  [63]. It may be that both  $P_{Zn}-2V_{Zn}$  and  $P_O$  defects are present in these films. However, given the consistency with  $P_{Zn}$  formation in the as-grown films, it is reasonable to assume that the high-temperature formation of the associated complex  $P_{Zn}-2V_{Zn}$  is the source of p-type behavior seen in post-annealed films. A key aspect in activating p-type conversion is in limiting the donor density that must be overcome for majority carrier p-type behavior to be observed.

### 6.3.2 Dependence of $Zn_{1-x}Mg_xO:P$ Film Properties on Magnesium Concentration

Previous work has shown that epitaxial films of the (Zn,Mg)O solid solution can maintain the wurtzite crystal structure for Mg concentrations as high as 33 at.%. For the compositions considered in this study, the phosphorus-doped (Zn,Mg)O films were wurtzite as determined by x-ray diffraction. Figure 6-9 shows the x-ray diffraction scans for the (Zn,Mg)O:P films, revealing only c-axis oriented, wurtzite peaks for the growth temperatures and Mg concentrations considered. The c-axis lattice parameter for the films was determined to be 5.1940 Å.

The primary focus of this study was on the acceptor dopant behavior as reflected in transport. Figure 6-10 A shows the carrier concentration of as-grown (Zn,Mg)O:P films grown

at different substrate temperatures. The resistivity for these films is also shown in Fig. 6-10 B. The  $Zn_{0.90}Mg_{0.10}O:P$  films grown at temperatures between 500-600°C were p-type as-deposited; films grown at  $T \geq 650^\circ C$  were n-type. This result is consistent with previous work reported on phosphorus-doped (Zn,Mg)O. Interestingly, the as-grown  $Zn_{0.95}Mg_{0.05}O:P$  films were not p-type for any of the growth conditions considered. The films showed only n-type conductivity over the entire growth temperature range. In previous work, it was speculated that the addition of Mg in phosphorus-doped ZnO increases the bandgap, in particular moving the conduction band higher in energy. This shift in the conduction band increases the activation energy of defect donor states commonly observed in undoped ZnO [93]. This drives the background electron density low enough to have the acceptor states due to phosphorus dictate carrier type. In the present experiment, it appears the a Mg concentration of  $x=0.10$  in  $Zn_{1-x}Mg_xO:P$  is a critical amount necessary in order to observe this carrier type conversion;  $x=0.05$  is not. It should be mentioned that the generation of compensating deep acceptor states with Mg alloying could also explain this result. This would also decrease the number of carriers and yields the lower carrier density for  $Zn_{0.9}Mg_{0.1}O:P$  as compared to  $Zn_{0.95}Mg_{0.05}O:P$ . However, it is difficult to identify a mechanism whereby the  $Mg^{+2}$  yields such states. The increase in the band gap with the addition of Mg in ZnO:P films should increasing the activation energy of donor states as well as the acceptor states due to phosphorus doping. However, previous work has shown that the increase in band gap with Mg addition to ZnO is mostly reflected in an increase in the conduction band edge. This is consistent with the fact that the conduction band in these compounds is primarily formed from cation orbitals.

It is interesting to note that, for both  $Zn_{0.90}Mg_{0.10}O:P$  and  $Zn_{0.95}Mg_{0.05}O:P$  films, the carrier density exhibits a minimum value for a growth temperature of 650 °C. The initial decrease in

carrier concentration with increasing deposition temperature may reflect an increase in band gap due to changes in the Zn/Mg ratio. The vapor pressure of Zn is notably higher than that for Mg. The films grown at the higher temperature should have higher Mg content, and hence a larger bandgap. This should result in lower carrier concentration. It is also possible that the decrease in carrier concentration with increasing deposition temperature reflects the activation of phosphorus in a relatively deep acceptor state. Theoretical arguments suggest that P substitution on the oxygen site should yield a deep acceptor state. It has also been suggested that the formation of a  $P_{Zn}-2V_{Zn}$  complex accounts for the observed acceptor state in p-type ZnO. The addition of Mg to ZnO should drive the acceptor state further from the valence band, regardless of the specific acceptor state defect.

The increase in carrier concentration and n-type conduction for  $T_{\text{growth}} \geq 650^{\circ}\text{C}$  is more difficult to explain. It may indicate a shift in the doping behavior of P, creating a high density of donor states at the higher growth temperatures. One possibility is the substitution of P on the Zn site, forming a triple donor state. The possibility of either donor or acceptor states with P doping reflects an amphoteric behavior that has been discussed for phosphorus atoms in ZnO at above.

Figure 6-11 shows the room temperature photoluminescence spectra for the as-grown  $(\text{Zn},\text{Mg})\text{O}:\text{P}$  films. The  $\text{Zn}_{0.95}\text{Mg}_{0.05}\text{O}:\text{P}$  films showed a near band edge luminescence peak and a broad defect band emission. The  $\text{Zn}_{0.9}\text{Mg}_{0.1}\text{O}:\text{P}$  films showed a broad defect band emission with no near band edge peak. For both cases, the defect-related visible emission is enhanced as the growth temperature is increased. The intensity of the near band edge peak also increased for the  $\text{Zn}_{0.95}\text{Mg}_{0.05}\text{O}:\text{P}$  films as growth temperature increased. Note that suppression of the near band edge luminescence with P doping has also been observed in ZnO, although this suppression is more pronounced with  $(\text{Zn},\text{Mg})\text{O}$  films. Clearly, the doping of ZnO films with P and Mg

generates deep level traps that suppress and/or prevent near bandedge emission. The peak position of near bandedge emission for the  $Zn_{0.95}Mg_{0.05}O:P$  films was 3.315 eV, which is slightly higher in energy than the 3.298 eV seen for our ZnO films. This shift is due to the increased bandgap in the (Zn,Mg)O:P films with increasing Mg concentration.

Rapid thermal annealing (RTA) was then performed in order to investigate possible activation of acceptor states in (Zn,Mg)O:P films. These experiments were restricted to films grown at 550 °C. The RTA processing was performed in 1 atm oxygen for a annealing time of 3 min. Carrier concentrations for the annealed films are shown in Fig. 6-12. Annealing the  $Zn_{0.95}Mg_{0.05}O:P$  films at 800 °C in oxygen for 3 min resulted in a carrier type conversion from n-type to p-type. These films showed a hole carrier density on the order of  $1.6 \times 10^{16} /cm^3$ . This carrier type conversion can be ascribed to the activation of phosphorus dopants. Further increasing the annealing temperature made the films highly n-type with no p-type behavior observed. This behavior is similar to that seen in phosphorus-doped ZnO films [59]. In contrast, the  $Zn_{0.90}Mg_{0.1}O:P$  films that showed p-type conductivity in the as-grown state converted to n-type with annealing.

The resistivity of the  $Zn_{0.95}Mg_{0.05}O:P$  films increased with RTA temperatures  $\leq 800^\circ C$ . Annealing at higher temperatures resulted in a reduction in resistivity. The resistivity of  $Zn_{0.90}Mg_{0.1}O:P$  films did not change significantly with annealing temperatures below 700 °C. However, resistivity decreased rapidly for anneals above this annealing temperature. For annealing temperatures less than 700 °C, the resistivity of  $Zn_{0.90}Mg_{0.1}O:P$  films is higher than  $Zn_{0.95}Mg_{0.05}O:P$  films, presumably due to the increased band gap. Interestingly, at high annealing temperatures, the  $Zn_{0.90}Mg_{0.1}O:P$  films became more conductive and n-type while  $Zn_{0.95}Mg_{0.05}O:P$  films remained resistive.

The luminescence properties of the annealed films was also examined. The PL spectra for annealed ZnMgO:P films is shown in Fig 6-13. The defect level photoluminescence increased with annealing temperature, but it slightly decreased at the highest annealing temperature. The near band edge emission of the films grown with 5 at. % generally decrease with annealing temperature. This indicates that deep non-radiative centers in the films were generated with annealing.

#### 6. 4 Summary

The properties of P-doped ZnO films subjected to rapid thermal annealing were examined. The as-deposited 1 at% phosphorus-doped ZnO films generally exhibit a lower donor density than 0.5 at % phosphorus doped ZnO films. The lower donor density is consistent with a higher density of P-related acceptors. The generation of anti-site  $P_{Zn}$  defects and their complex with  $V_{Zn}$  shows strong sensitivity on the growth condition. The excess P atoms in 1 at% phosphorus-doped ZnO films generates P-related donors as well and compensates the P-related acceptors. As a result, this amphoteric doping behavior of phosphorus in ZnO influences the transport properties even though all as-grown samples have n-type conductivity. Post annealing causes a carrier type conversion for the ZnO:P film grown at 700 °C. Samples grown at the other temperatures tend to remain in n-type even after the post annealing. In addition, variable magnetic field Hall measurements confirmed the p-type behavior.

The realization of p-type conductivity in  $Zn_{1-x}Mg_xO:P$  thin films is dependent on Mg content. At concentrations of  $x=0.1$ , p-type conduction can be achieved without post thermal annealing treatments. For lower Mg concentrations, an RTA treatment is necessary. Mg in the ZnMgO:P films contributes to the p-type conduction by increasing the activation energy of donor defects even though it also increase that for the acceptor defects. Mg incorporation in the

ZnMgO:P films may also enhance deep level traps. Unfortunately, Mg alloying in ZnO films degrades the luminescence properties. Deep non-radiative centers in the ZnMgO:P films were generated with annealing.

Table 6-1. Hall data of 0.5% P-doped films grown at various temperatures and subjected to various post-annealing temperatures.

Growth Temp(°C)	(ZnO:P <sub>0.005</sub> ) – Hall data (150 mTorr growth pressure)			
	As Grown	RTA temperature (°C) / (annealing time = 2 min)		
		850	900	950
600	4.47 Ω-cm	4400 Ω-cm	140 Ω-cm	1.1 Ω-cm
	$1.1 \times 10^{18} \text{ cm}^{-3}$	$3.9 \times 10^{16} \text{ cm}^{-3}$	$1.2 \times 10^{17} \text{ cm}^{-3}$	$4.9 \times 10^{18} \text{ cm}^{-3}$
	1.28 cm <sup>2</sup> /Vs	0.037 cm <sup>2</sup> /Vs	0.37 cm <sup>2</sup> /Vs	1.2 cm <sup>2</sup> /Vs
	N-type	N-type	N-type	N-type
650	0.17 Ω-cm	1700 Ω-cm	70 Ω-cm	6.3 Ω-cm
	$2.6 \times 10^{18} \text{ cm}^{-3}$	$2.9 \times 10^{15} \text{ cm}^{-3}$	$4.3 \times 10^{17} \text{ cm}^{-3}$	$2.7 \times 10^{18} \text{ cm}^{-3}$
	1.38 cm <sup>2</sup> /Vs	1.30 cm <sup>2</sup> /Vs	0.20 cm <sup>2</sup> /Vs	0.36 cm <sup>2</sup> /Vs
	N-type	N-type	N-type	N-type
700	15.59 Ω-cm	3400 Ω-cm	<b>360 Ω-cm</b>	<b>19 Ω-cm</b>
	$6.2 \times 10^{17} \text{ cm}^{-3}$	$3.9 \times 10^{15} \text{ cm}^{-3}$	<b><math>4.2 \times 10^{16} \text{ cm}^{-3}</math></b>	<b><math>4.1 \times 10^{17} \text{ cm}^{-3}</math></b>
	0.98 cm <sup>2</sup> /Vs	0.47 cm <sup>2</sup> /Vs	<b>0.40 cm<sup>2</sup>/Vs</b>	<b>0.80 cm<sup>2</sup>/Vs</b>
	N-type	N-type	<b><u>P-type</u></b>	<b><u>P-type</u></b>
750	2.2 Ω-cm	630 Ω-cm	140 Ω-cm	<b>21 Ω-cm</b>
	$4.8 \times 10^{17} \text{ cm}^{-3}$	$1.4 \times 10^{16} \text{ cm}^{-3}$	$2.2 \times 10^{17} \text{ cm}^{-3}$	<b><math>9.5 \times 10^{17} \text{ cm}^{-3}</math></b>
	5.80 cm <sup>2</sup> /Vs	0.68 cm <sup>2</sup> /Vs	0.21 cm <sup>2</sup> /Vs	<b>0.30 cm<sup>2</sup>/Vs</b>
	N-type	N-type	N-type	<b><u>P-type</u></b>
800	2.0 Ω-cm	360 Ω-cm	100 Ω-cm	4.5 Ω-cm
	$4.5 \times 10^{17} \text{ cm}^{-3}$	$2.6 \times 10^{16} \text{ cm}^{-3}$	$2.6 \times 10^{16} \text{ cm}^{-3}$	$3.7 \times 10^{18} \text{ cm}^{-3}$
	7.10 cm <sup>2</sup> /Vs	0.66 cm <sup>2</sup> /Vs	2.40 cm <sup>2</sup> /Vs	0.38 cm <sup>2</sup> /Vs
	N-type	N-type	N-type	N-type

Table 6-2. Hall data of 1.0% P-doped films grown at various temperatures and subjected to various post-annealing temperatures.

Growth		(ZnO:P <sub>0.01</sub> ) – Hall data (150 mTorr growth pressure)		
Temp (°C)	As Grown	RTA temperature (°C) / (annealing time = 2 min)		
		850	900	950
600	27.34 Ω-cm	32.2 Ω-cm	24.5 Ω-cm	<b>77.7 Ω-cm</b>
	1.1 x 10 <sup>17</sup> cm <sup>-3</sup>	2.6 x 10 <sup>14</sup> cm <sup>-3</sup>	1.1 x 10 <sup>18</sup> cm <sup>-3</sup>	<b>1.6 x 10<sup>17</sup> cm<sup>-3</sup></b>
	2.06 cm <sup>2</sup> /Vs	7.55 cm <sup>2</sup> /Vs	0.24 cm <sup>2</sup> /Vs	<b>0.50 cm<sup>2</sup>/Vs</b>
	N-type	N-type	N-type	<b>P-type</b>
650	20.1 Ω-cm	10400 Ω-cm	38.6 Ω-cm	1.91 Ω-cm
	4.7 x 10 <sup>18</sup> cm <sup>-3</sup>	6.7 x 10 <sup>14</sup> cm <sup>-3</sup>	3.7 x 10 <sup>18</sup> cm <sup>-3</sup>	3.2 x 10 <sup>18</sup> cm <sup>-3</sup>
	0.07 cm <sup>2</sup> /Vs	0.01 cm <sup>2</sup> /Vs	0.04 cm <sup>2</sup> /Vs	1.03 cm <sup>2</sup> /Vs
	N-type	N-type	N-type	N-type
700	1.98 Ω-cm	35.2 Ω-cm	<b>488 Ω-cm</b>	<b>801 Ω-cm</b>
	1.8 x 10 <sup>17</sup> cm <sup>-3</sup>	2.3 x 10 <sup>14</sup> cm <sup>-3</sup>	<b>1.6 x 10<sup>17</sup> cm<sup>-3</sup></b>	<b>2.4 x 10<sup>15</sup> cm<sup>-3</sup></b>
	18.1 cm <sup>2</sup> /Vs	7.80 cm <sup>2</sup> /Vs	<b>0.81 cm<sup>2</sup>/Vs</b>	<b>3.20 cm<sup>2</sup>/Vs</b>
	N-type	N-type	<b>P-type</b>	<b>P-type</b>
750	2.41 Ω-cm	22.0 Ω-cm	4.36 Ω-cm	2.33 Ω-cm
	2.8 x 10 <sup>17</sup> cm <sup>-3</sup>	5.9 x 10 <sup>14</sup> cm <sup>-3</sup>	1.8 x 10 <sup>18</sup> cm <sup>-3</sup>	3.3 x 10 <sup>18</sup> cm <sup>-3</sup>
	9.18 cm <sup>2</sup> /Vs	4.80 cm <sup>2</sup> /Vs	0.79 cm <sup>2</sup> /Vs	0.81 cm <sup>2</sup> /Vs
	N-type	N-type	N-type	N-type
800	0.68 Ω-cm	34.1 Ω-cm	<b>46 Ω-cm</b>	6300 Ω-cm
	4.2 x 10 <sup>17</sup> cm <sup>-3</sup>	5.7 x 10 <sup>14</sup> cm <sup>-3</sup>	<b>2.0 x 10<sup>17</sup> cm<sup>-3</sup></b>	5.2 x 10 <sup>15</sup> cm <sup>-3</sup>
	22.1 cm <sup>2</sup> /Vs	3.19 cm <sup>2</sup> /Vs	<b>0.68 cm<sup>2</sup>/Vs</b>	0.19 cm <sup>2</sup> /Vs
	N-type	N-type	<b>P-type</b>	N-type
850	0.027 Ω-cm	7 Ω-cm	8.11 Ω-cm	1.51 Ω-cm
	1.1 x 10 <sup>19</sup> cm <sup>-3</sup>	7.5 x 10 <sup>17</sup> cm <sup>-3</sup>	1.5 x 10 <sup>18</sup> cm <sup>-3</sup>	2.5 x 10 <sup>18</sup> cm <sup>-3</sup>
	22 cm <sup>2</sup> /Vs	1.20 cm <sup>2</sup> /Vs	0.49 cm <sup>2</sup> /Vs	1.65 cm <sup>2</sup> /Vs
	N-type	N-type	N-type	N-type

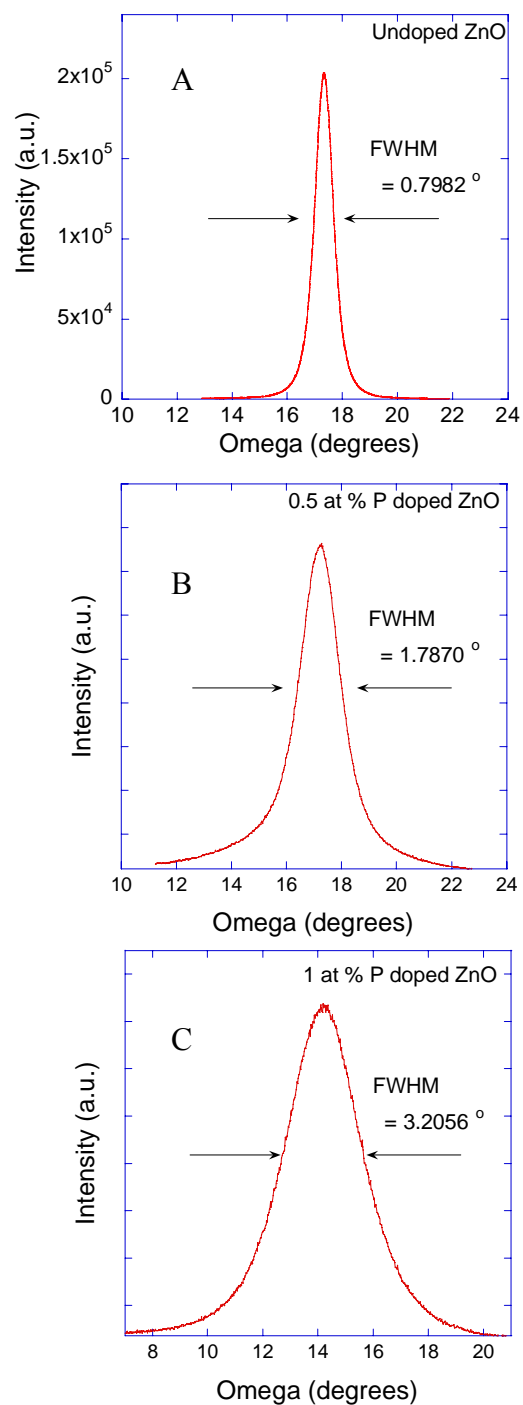
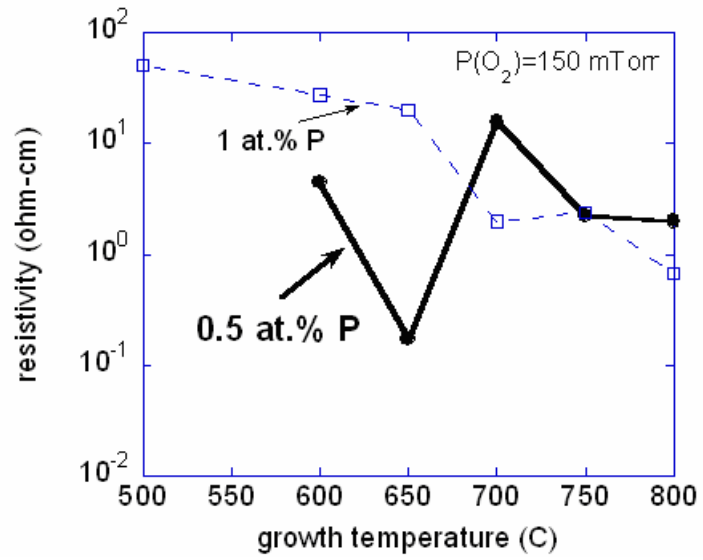
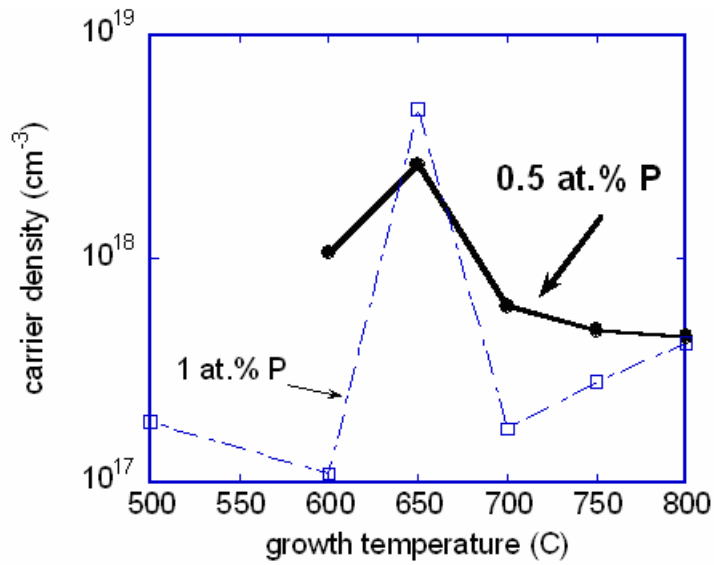


Figure 6-1. X-ray diffraction omega rocking curves for A) undoped, B) 0.5 at.% P-doped, and C) 1.0 at.% doped ZnO films grown by pulsed laser deposition. Growth conditions were 700°C and 150 mTorr oxygen.



A



B

Figure 6-2. Hall data for as-deposited ZnO:P films, showing A) resistivity and B) carrier density. All films in this figure are n-type.

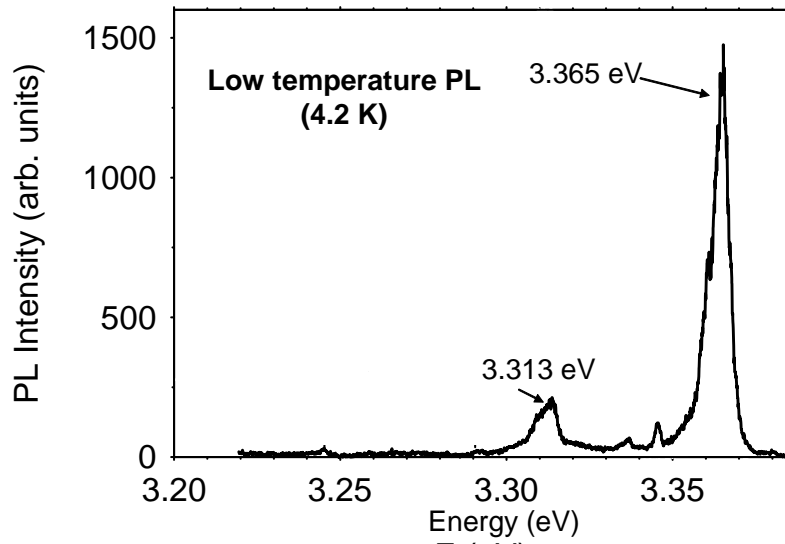


Figure 6-3. Low temperature photoluminescence (PL) for a ZnO:P film showing an acceptor-associated peak at 3.313 eV.

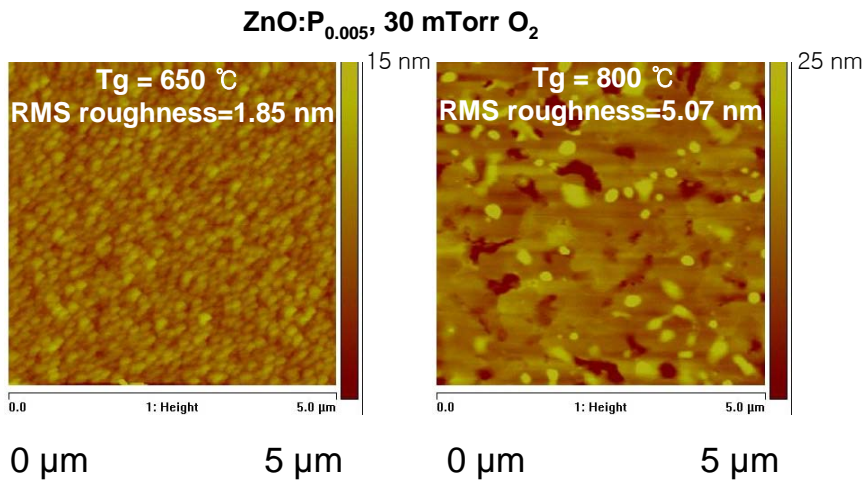


Figure 6-4. Atomic force microscopy images for 0.5 at.% P-doped ZnO films grown at different substrate temperatures.

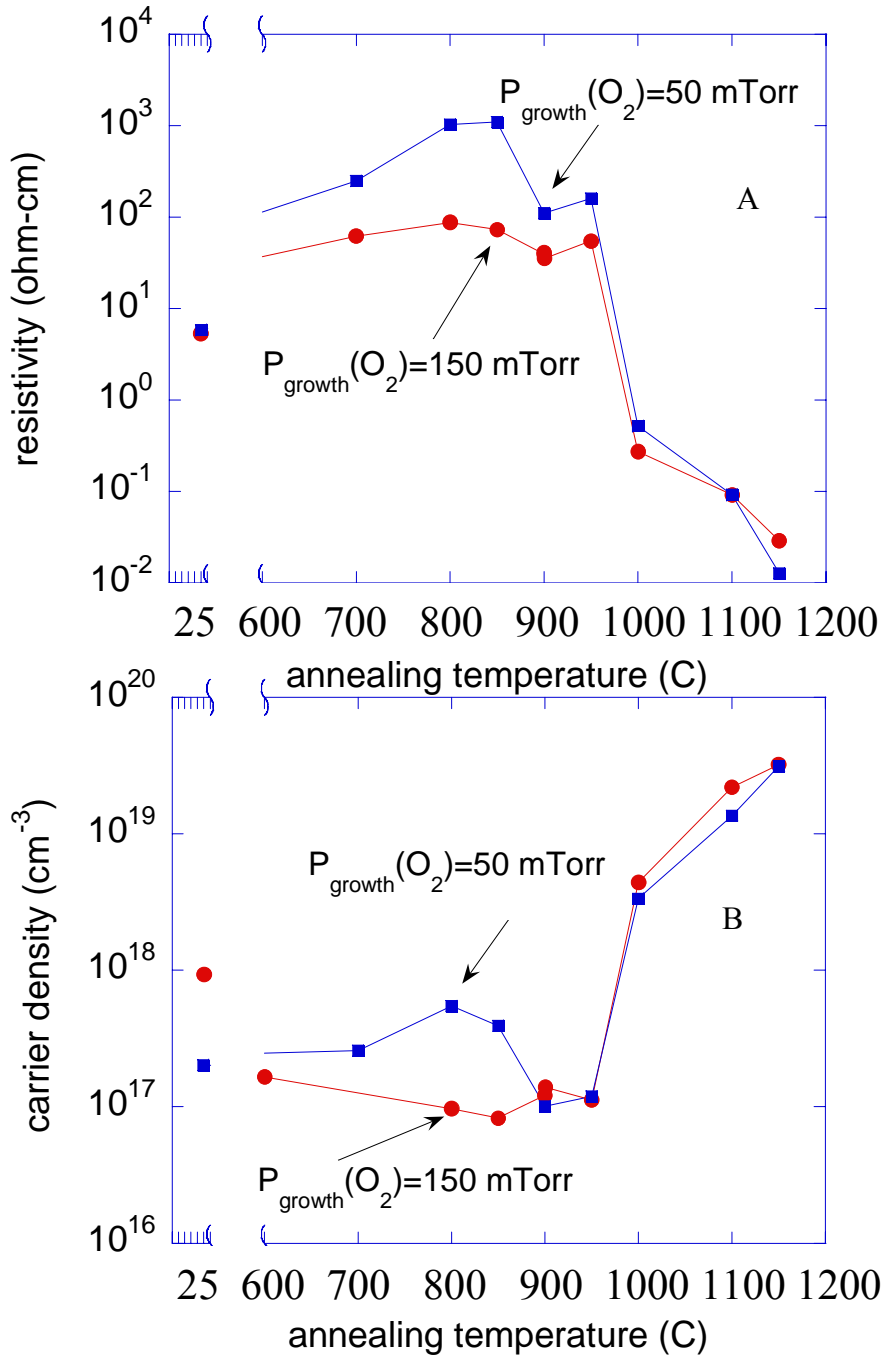


Figure 6-5. Hall data for rapid thermal annealed ZnO films doped with 0.5 at.% P, grown at 700°C, showing A) resistivity and B) carrier density as a function of annealing temperature. Most films in this figure were n-type.

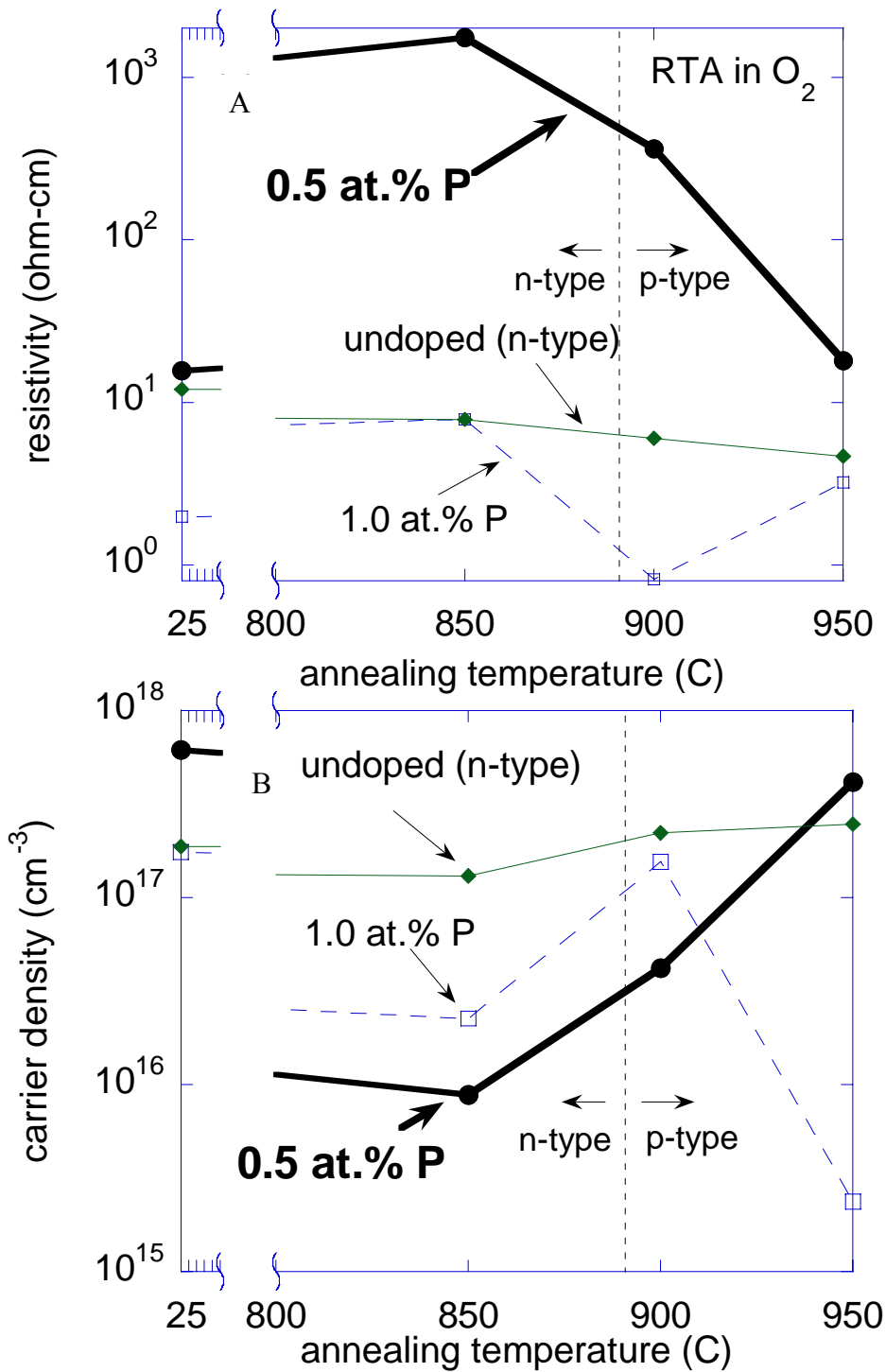


Figure 6-6. Hall data for rapid thermal annealed ZnO films doped with 0.5 and 1.0 at.% P, grown at 700°C, 150 mTorr oxygen, showing A) resistivity and B) carrier density as a function of annealing temperature.

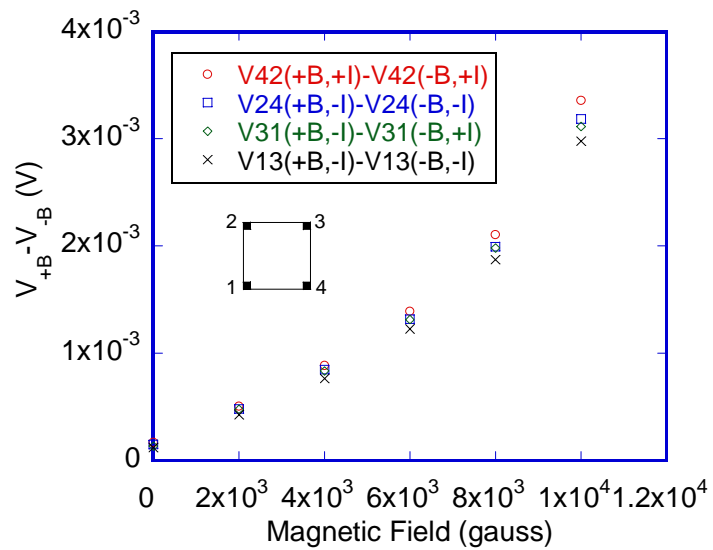


Figure 6-7. Plot of van der Pauw Hall voltage differences for a p-type 0.5 at.% P-doped ZnO film subjected to a 900°C RTA process. The voltage difference polarity for all measurements are consistent with p-type conduction.

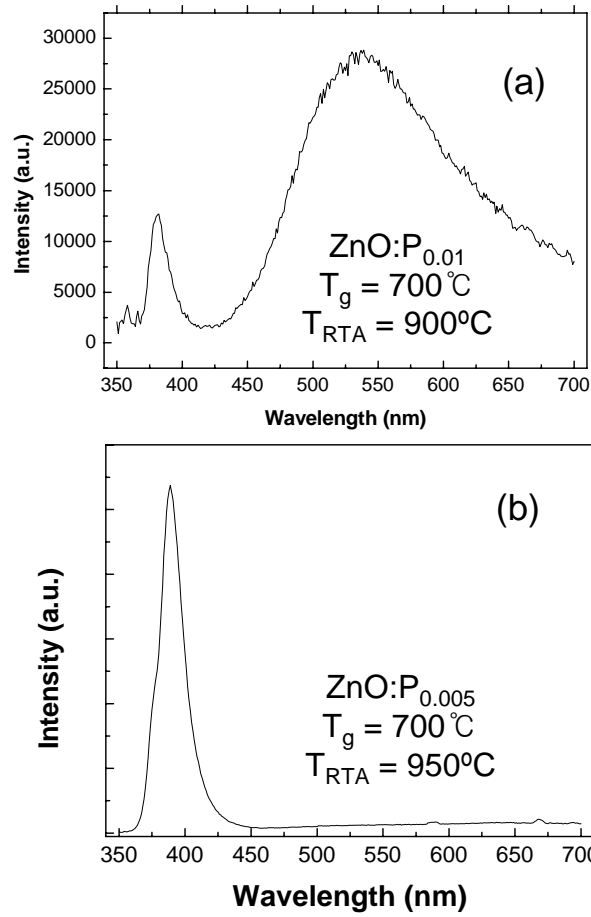
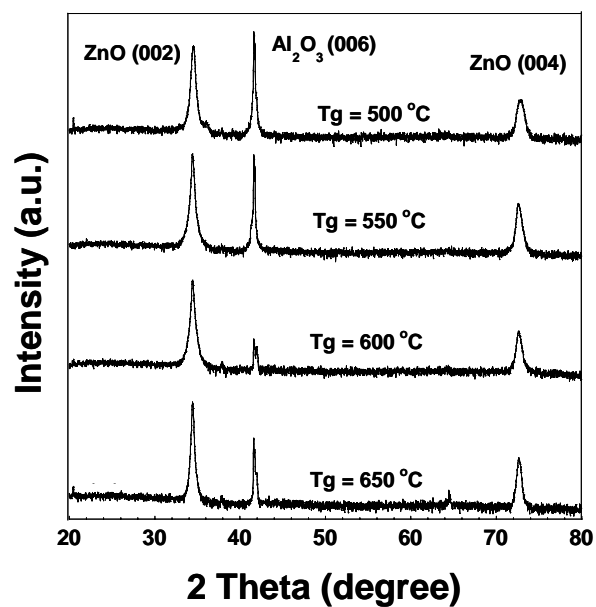
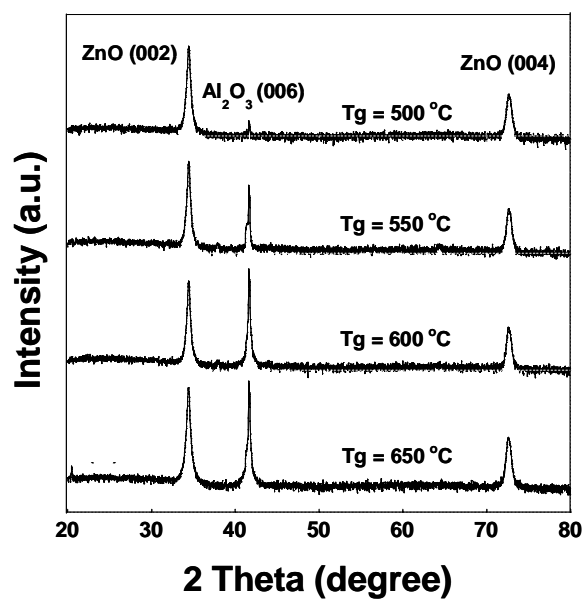


Figure 6-8. Room temperature photoluminescence data for A) 1.0 at.% and B) 0.5 at.% P-doped ZnO films that were post-annealed and p-type.

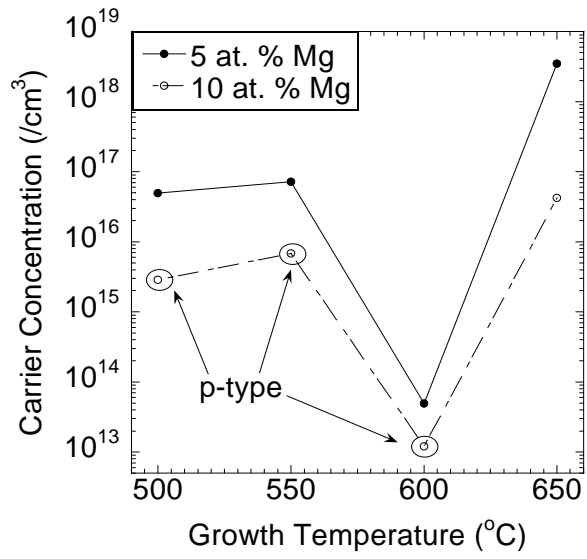


A

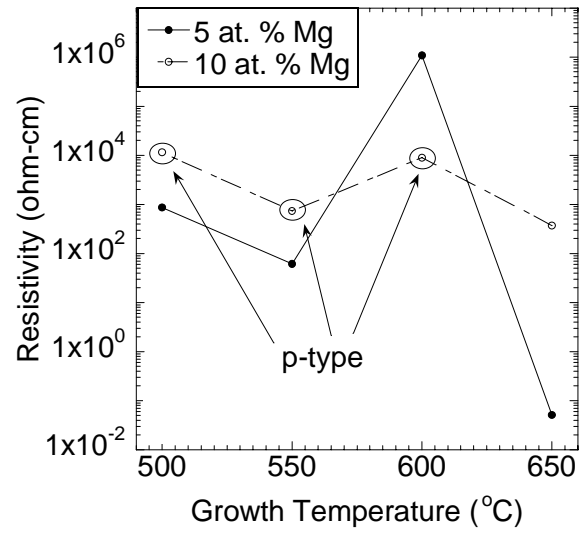


B

Figure 6-9. XRD spectra of as-grown ZnMgO:P films that contains 5 A) and 10 B) at. % of Mg.

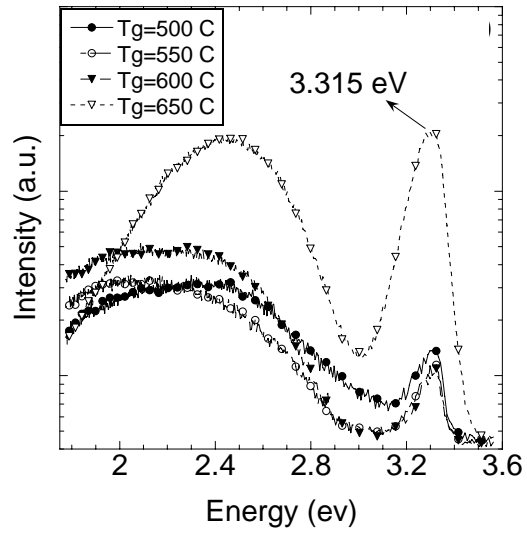


A

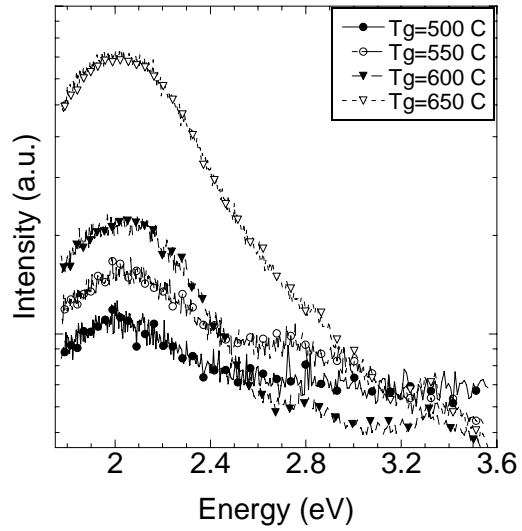


B

Figure 6-10. Carrier concentration A) and resistivity B) of as-grown ZnMgO:P<sub>0.2</sub> films grown with different growth temperatures.

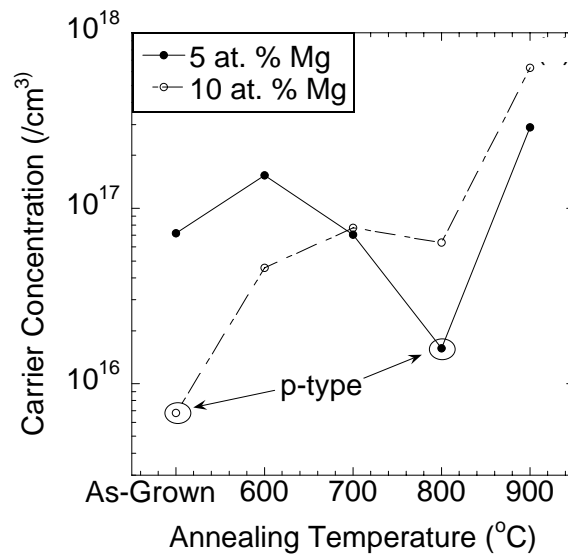


A

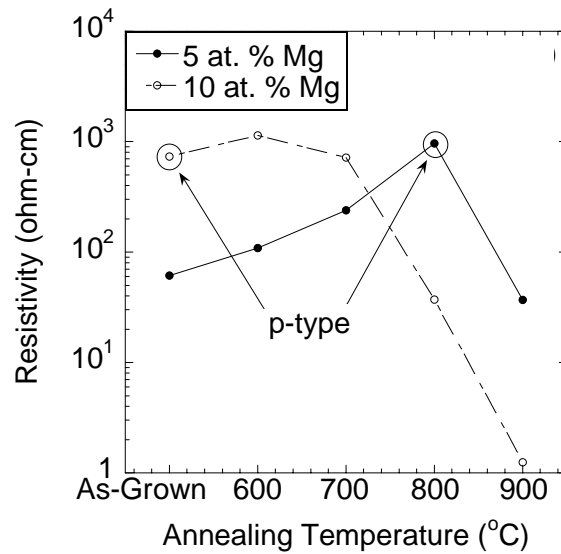


B

Figure 6-11. PL spectra for as-grown ZnMgO:P<sub>0.2</sub> films that contains 5 A) and 10 B) at. % of Mg.

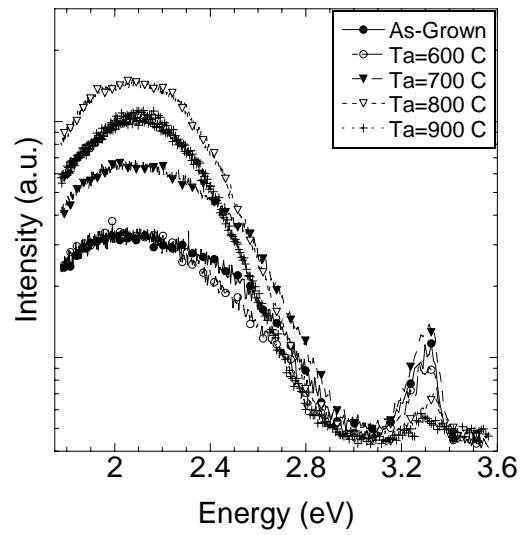


A

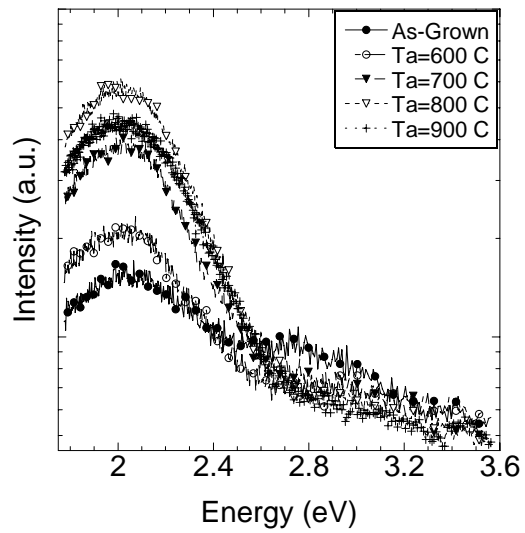


B

Figure 6-12. Carrier concentration A) and resistivity B) of ZnMgO:P<sub>0.2</sub> films with the annealing temperature.



A



B

Figure 6-13. PL spectra for annealed ZnMgO:P<sub>0.2</sub> films that contains 5 A) and 10 B) at. % of Mg.

## CHAPTER 7 ZINC OXIDE LIGHT EMITTING DIODES

### 7. 1 Introduction

In recent years, significant efforts have been directed towards the fabrication of ZnO thin film [143, 168] and nanowire [169, 170] devices, including rectifying [162, 171-173] and light emitting diodes (LED). Lim *et al.* have reported the fabrication of ZnO based light emitting diodes using sputter deposited phosphorus-doped ZnO as the p-type layer [11]. Ryu *et al.* employed BeZnO/ZnO quantum wells and obtained UV electroluminescence [10]. Tsukazaki *et al.* fabricated a p-ZnO/i-ZnO/n-ZnO LED on ScAlMgO<sub>4</sub> by using repeated-temperature-modulation epitaxy for the p-type ZnO:N layer [8]. Liu *et al.* reported electroluminescence from a ZnO homojunction light emitting diodes grown on a single crystal ZnO substrate [9]. Ye *et al.* used N-Al codoping for p-type doping and fabricated ZnO LEDs on Si with sputter deposition [174]. In all cases, the reported light emission intensity from the ZnO LEDs was relatively weak. A significant challenge in developing ZnO light emitting diodes is the formation of p-type material. ZnO exhibits an asymmetric doping behavior, where it is easily made n-type but difficult to realize p-type [7]. Despite this challenge, many groups have reported on successful p-type doping with several dopants [26, 59, 65]. In previous chapter, phosphorus-doped p-type ZnO was successfully achieved by pulsed laser deposition. In this chapter, the synthesis and properties of ZnO LED heterojunctions employing these P-doped ZnO materials is reported.

### 7. 2 Experimental

The ZnO thin film structures were fabricated on the sapphire (0001) substrate using pulsed laser deposition. Phosphorus and gallium were used as the p- and n-type dopants, respectively. Prior to LED epitaxial film deposition, an undoped ZnO buffer layer was deposited on the sapphire at 400°C and a pressure of 20 mTorr as a nucleation layer. This buffer layer was

annealed at 650 °C. The subsequent epitaxial films were grown in an oxygen partial pressure of 150 mTorr. The LED structures consist of 250 nm of P-doped ZnO, 40 nm of undoped Zn<sub>0.9</sub>Mg<sub>0.1</sub>O, 40 nm of ZnO, 40 nm of Zn<sub>0.9</sub>Mg<sub>0.1</sub>O, and 450 nm of Ga-doped ZnO. Figure 1 shows a schematic of the device structure. The epitaxial films were grown at a substrate temperature of 700°C. Phosphorus-doped ZnO targets were fabricated using high purity (99.9995 %) ZnO mixed with P<sub>2</sub>O<sub>5</sub> (99.998 %) as the doping agent. The phosphorus doping levels was 0.5 at. %. Gallium-doped ZnO targets were fabricated with high purity (99.9995 %) ZnO mixed with gallium oxide (99.998 %) as the doping agent. The gallium doping level was 1 at. %. The carrier concentration in the P and Ga doped ZnO layers were estimated to be  $1 \times 10^{17} \text{ cm}^{-3}$  and  $5 \times 10^{19} \text{ cm}^{-3}$ , respectively, based on Hall measurements performed on single layer films grown under the same conditions. All targets were sintered at 1000°C for 12 hours in air. The targets were ablated with a KrF excimer laser with the laser frequency of 1 Hz and energy density of approximately 1.5 J/cm<sup>2</sup>.

Prior to the LED fabrication, the ZnO multilayered structures were annealed in a rapid thermal annealing (RTA) system at 900 °C for 1 min under an oxygen ambient to activate the p-type dopant. The LED fabrication started with device isolation and followed with p-mesa definition using dilute phosphoric acid solution. Electron beam deposited Ni (20nm)/Au (80nm) and Ti (20nm)/Au(80nm) were used as the p- and n-Ohmic metallization [175, 176]. The current-voltage characteristics were measured using an Agilent 4145B parameter analyzer. The electroluminescence spectra were measured with a Princeton Instrument spectrophotometer equipped with a CCD array. The total light output power was measured by a Si photodiode. Also, room temperature PL measurements were performed with a He-Cd laser source.

### 7.3 Results and Discussion

The I-V characteristics of the as-fabricated diodes showed high leakage currents as seen in Figure 7-1. There was limited diode rectification and light emission. However, if the fabricated diodes were annealed at 350 °C for 5 mins in oxygen, rectifying I-V characteristics and electroluminescence were observed. This result is also shown in Figure 7-1. Note that annealing at 350°C in oxygen should do little or nothing to either the oxygen content or phosphorus location within the bulk of the structure given that the films were grown at 700°C and annealed at 900°C prior to device wet processing. The stability of the phosphorus doping profiles to high temperature growth and annealing can be seen in figure 7-2. Here, the secondary ion mass spectrometry (SIMS) profiles of ZnO/ZnMgO:P multilayers are examined both as-grown and annealed. The profile for the as-grown ZnO/ZnMgO:P multilayer shows no evidence for significant phosphorus interdiffusion across ZnO/ZnMgO interfaces during growth despite the fact that growth occurred at 700°C. Figure 7-2 B shows the SIMS profile for a multilayer structure subjected to a 1 min rapid thermal anneal in nitrogen at 750°C. Again, no evidence for phosphorus diffusion across the ZnO/ZnMgO heterointerface is observed.

While the 350°C anneal in oxygen has little impact on bulk oxygen or phosphorus content, it does appear to eliminate surface and mesa sidewall conduction that was introduced when the LED structure was fabricated by wet etching and photolithography. Table I shows the effect of wet etching on the resistivity. The Table 7-1 shows P-doped ZnO film resistivities measured before and after a moderate wet etching exposure to dilute phosphoric acid. As seen in the Table 7-1, the extrapolated resistivity (assuming uniform carrier density distribution) decreases significantly with exposure to the etchant. The carrier type of the etched samples was n-type. The origin of this increase in conductivity could be metallization of the surface or incorporation

of hydrogen as a donor. Hydrogen can be easily incorporated in to ZnO during processing [101, 102, 140, 177]. Regardless of the origin, the 350°C anneal eliminates this conduction path.

The applied voltage and total light emission intensity as a function of drive current for a typical annealed ZnO:P/ZnMgO/ZnO/ZnMgO/ZnO:Ga heterojunction is shown in Fig. 7-3 A. The metal contacts were confirmed to be ohmic by linear I-V curves. Turn-on voltage for this device was ~ 2.2 V, which is lower than what would be anticipated for a pn junction for a 3.2 eV semiconductor. Figure 7-3 B shows the optical spectra for the device taken at two different applied voltage biases. Although light emission intensity varied linearly with drive current, the near band edge electroluminescence peak does not emerge until the applied voltage is 7 volts or greater. Given that the device is a planar structure, the voltage drop will occur partially along the planar current path, partially across the junction. Figure 7-4 compares the electroluminescence and photoluminescence spectra for the LED heterostructure. The EL spectra shows the peak at 385 nm. This peak is slightly shifted to the longer wavelengths relative to the photoluminescence observed for the same structure. The origin of this shift is unclear. Also, the electroluminescence spectrum shows more visible emission intensity than that seen in the photoluminescence spectrum.

#### **7. 4 Summary**

ZnO light emitting diodes were fabricated on c-plane sapphire by using p-i-n heterostructures. For the heterostructural diodes, Zn<sub>0.9</sub>Mg<sub>0.1</sub>O/ZnO/ Zn<sub>0.9</sub>Mg<sub>0.1</sub>O layers were used to confine the carriers into the quantum well. This device showed diode characteristics and the light emission was observed by Si photodiode detector. Also, the electroluminescence(EL) spectra was observed at the near bandedge of 385 nm with a small deep level emission.

Table 7-1 Resistivity for P-doped ZnO thin films before and after wet etching.

Sample		Resistivity (ohm-cm)
RTA 900°C	Before etching	38.605
	After etching	9.3952
RTA 950°C	Before etching	1.9089
	After etching	0.957

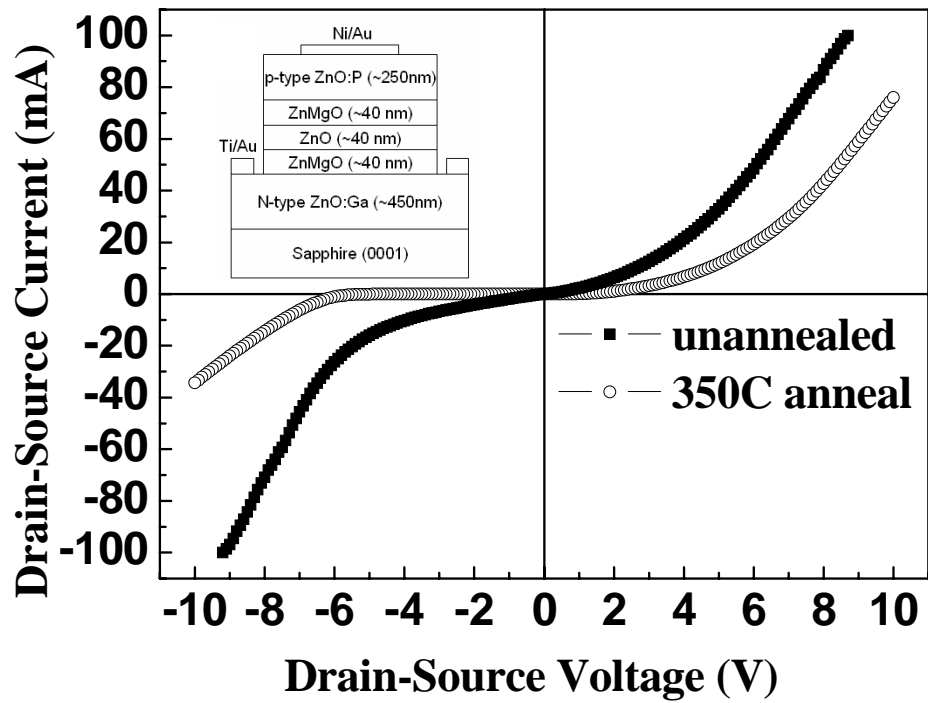


Figure 7-1. I-V characteristics for a ZnO:P/Zn<sub>0.9</sub>Mg<sub>0.1</sub>O/ZnO/Zn<sub>0.9</sub>Mg<sub>0.1</sub>O/ZnO:Ga heterojunction diode both as-fabricated and after a 350°C anneal. Also show in the inset is a schematic of the device structure.

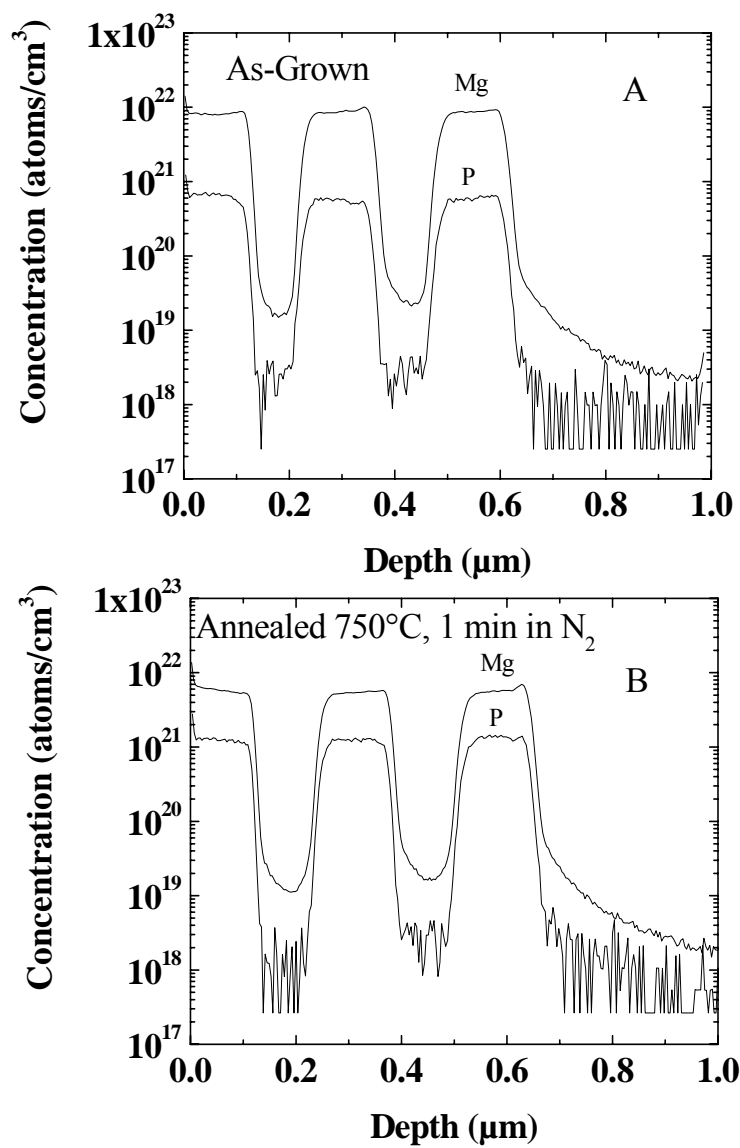


Figure 7-2. Secondary ion mass spectrometry composition depth profile taken for a ZnMgO:P/ZnO multilayer both A) without and B) with a post-growth anneal.

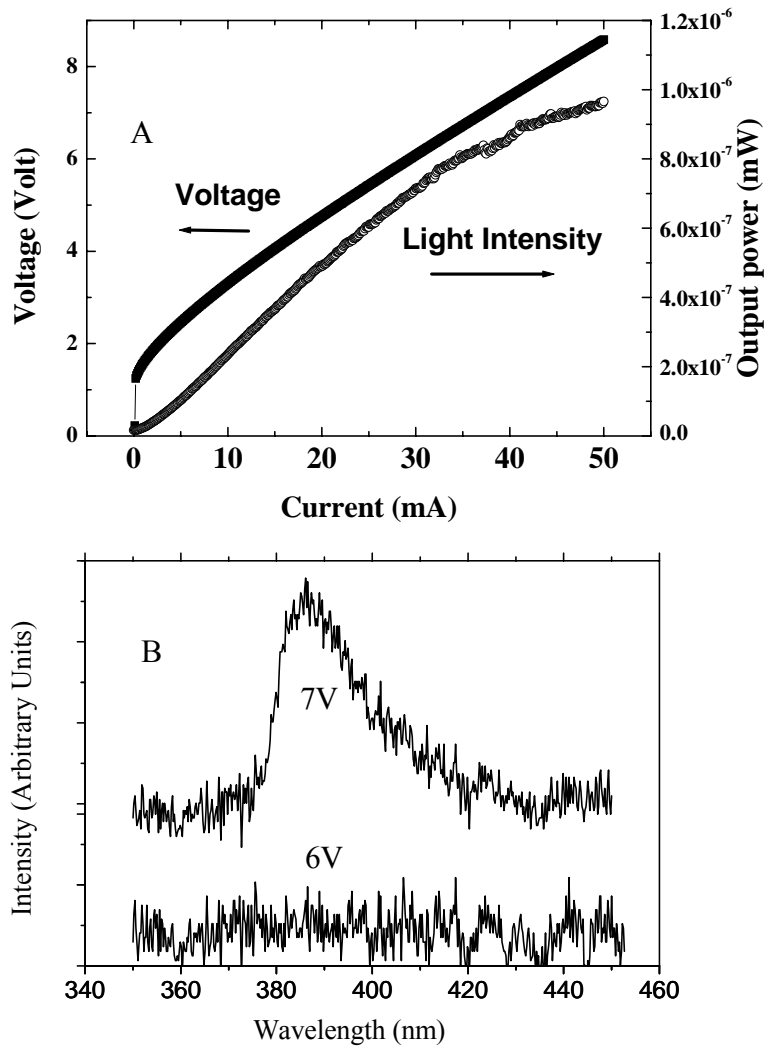


Figure 7-3. Plot of A) light intensity and voltage as a function of drive current for an annealed ZnO:P/Zn<sub>0.9</sub>Mg<sub>0.1</sub>O/ZnO/Zn<sub>0.9</sub>Mg<sub>0.1</sub>O/ZnO:Ga heterojunction diode. Also shown B) is the spectra for the diode at two different bias voltages.

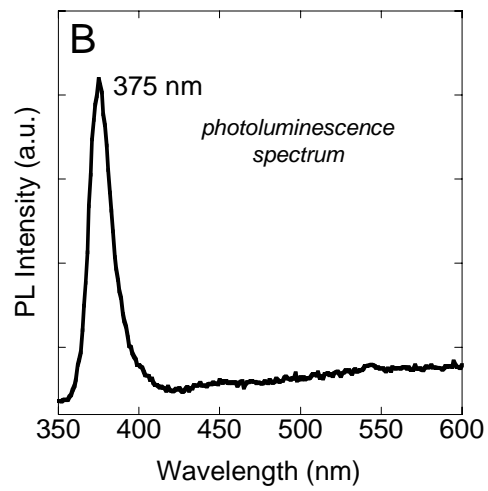
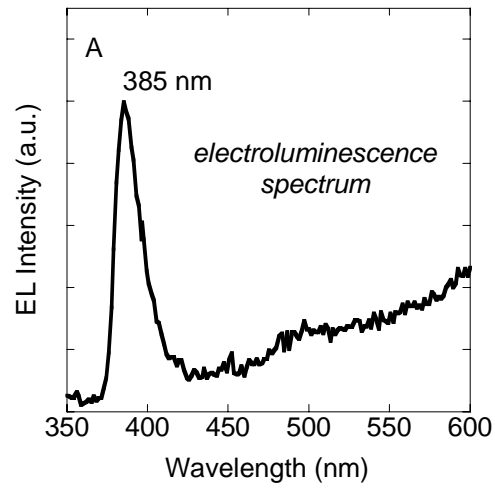


Figure 7-4. Room temperature optical spectra of a ZnO:P/Zn<sub>0.9</sub>Mg<sub>0.1</sub>O/ZnO/Zn<sub>0.9</sub>Mg<sub>0.1</sub>O/ZnO:Ga heterojunction diode for A) electroluminescence and B) photoluminescence.

## CHAPTER 8 CONCLUSION

The research presented in this dissertation focused on ZnO thin film growth by pulsed laser deposition for the realization of ZnO light emitting diodes. Firstly, undoped ZnO films were investigated to understand native defects and to obtain a high quality films. P-type ZnO and ZnMgO films were achieved by doping with phosphorus. Film properties were examined. Lastly, ZnO LEDs were fabricated by using P-doped p-type ZnO layer. Light emission was observed.

### **8. 1 Undoped ZnO Thin Films**

For the undoped ZnO, understanding behavior of the native defects and obtaining a high quality films are major issues addressed in this study. ZnO thin films were grown on sapphire substrate with pure O<sub>2</sub> and O<sub>2</sub> /O<sub>3</sub> gas mixture as an oxidant source. The electrical and optical properties of the films were investigated.

The ZnO films grown with O<sub>2</sub>/O<sub>3</sub> mixture gas exhibit almost one order of magnitude lower donor defect density as compared to those grown with pure O<sub>2</sub>. The decrease in donor defect density for ZnO films grown with O<sub>2</sub>/O<sub>3</sub> gas mixture relative to those grown in molecular oxygen can be explained by highly active oxygen atoms generating acceptor defects such as Zn vacancies and oxygen interstitials. Ozone can create deep acceptor-like defects in ZnO. These defects yields a lower donor defect density for the as-deposited ZnO samples grown with O<sub>2</sub>/O<sub>3</sub>. The growth in ozone increases the acceptor defects. However, the native donor defects are still dominant and the number of acceptor defects created in the film is insufficient to overcome donor defects. Thus, the films remain n-type.

The PL properties at room temperature showed that the ozone growth increases the deep level emission and generates non-radiative centers. This indicates that active ozone creates deep acceptor levels, leading to a decrease in donor defect density.

Annealing studies were performed on ZnO films grown by using either O<sub>2</sub> and an O<sub>2</sub>/O<sub>3</sub> gas mixture as the oxidant. Annealing results in a significant improvement of crystallinity compared to the as-deposited material and improves surface roughness as well for both cases. Interestingly, the carrier concentration of the ZnO films grown with O<sub>2</sub>/O<sub>3</sub> mixture gas slightly increases with oxygen annealing. This behavior is contrary to the general behavior ZnO films grown with pure O<sub>2</sub>. This indicates that the annealing treatment annihilates the ozone-induced acceptor defects that compensate the donors. In the room temperature PL measurements, the band edge emission of annealed ZnO films shows different behavior depending on the oxidation source used during growth. we can deduce that the non-radiative traps of ZnO samples grown with O<sub>2</sub>/O<sub>3</sub> mixture gas are not significantly affected by the annealing and have a different origin from that of ZnO films grown with pure O<sub>2</sub>. The source is probably due to the acceptor-like defects caused by ozone.

The film quality critically depends on the initial growth mode. Using a buffer and controlling the buffer growth parameters play a key role in high quality ZnO film growth. The effects of buffer growth temperature and pressure on the properties of ZnO films were investigated. The use of a buffer layer has a significant impact of the subsequent ZnO layer morphology. The RMS roughness was reduced by using a buffer for the buffer layer growth temperatures and pressures considered. The FWHM decreases as the buffer temperature increases. Using a buffer at low temperature and pressure prevents the growth of large hexagonal crystals, improves morphology, but degrades the crystallinity. The high quality ZnO film was achieved via high temperature deposited ZnO buffer layer. The high temperature deposited ZnO buffer layer yields an improvement for in-plane and out-of-plane crystallinity. The FWHM of the XRD (002) and (102)  $\omega$ -rocking curve for the ZnO film was as narrow as 27.36 arcsec (0.0076°)

and 447.12 arcsec ( $0.1242^\circ$ ), respectively. The residual donor density is reduced one order of magnitude as compared to the ZnO film grown without the buffer. It shows a high mobility of  $87.68 \text{ cm}^2/\text{V-s}$ , which is about three times higher than that of the ZnO film grown without the buffer layer. In terms of optical properties, The defect related visible emission was reduced by using the high temperature deposited ZnO buffer layer. The ZnO films showed peaks at 3.3155, 3.2546, 3.2112, and 3.1234 eV. These peaks are tentatively attributed to the free excitons and their phonon replicas, although these features are rarely seen in room temperature PL for ZnO. The RMS surface roughness was measured to be 47.8 nm and 1.55 nm for ZnO films grown without and with the high temperature deposited ZnO buffer, respectively.

## 8. 2 Phosphorus Doped ZnO and ZnMgO

A high density of defects and lattice strain are associated with high phosphorus doping. The rocking curve full-width half-maximum (FWHM) was  $0.80^\circ$  for the undoped film,  $1.79^\circ$  for 0.5 at.% P, and  $3.21^\circ$  for the film doped with 1 at.% P. All as-deposited ZnO:P samples show n-type conductivity regardless of the growth temperature and phosphorus doping level. However, p-type conversion of the as-deposited P-doped ZnO films was achieved via post-growth annealing. The n-type conductivity of as-grown P-doped films reflects an amphoteric doping behavior for phosphorus in ZnO in yielding either donor or acceptor states. The dominant P-related donor is assumed to be the  $\text{P}_{\text{Zn}}$  antisite defect. The anti-site  $\text{P}_{\text{Zn}}$  defects could combine with a double acceptor,  $\text{V}_{\text{Zn}}$ , which is a favorable native defect in O-rich growth condition, and generate  $\text{P}_{\text{Zn}}\text{-}2\text{V}_{\text{Zn}}$  complexes. This complex is predicted to be a shallow acceptor. Various magnetic fields Hall measurements were performed to confirm p-type conductivity of ZnO:P films. For measurements taken at the five magnetic fields considered, all voltage pairs for this sample are consistent with p-type majority carrier conduction. The PL properties were

deteriorated with high phosphorus doping. Clearly, the semiconducting properties are better for lower P concentrations.

It appears that a Mg concentration of  $x=0.10$  in  $Zn_{1-x}Mg_xO:P$  is a critical amount necessary in order to observe the p-type conductivity in as-deposited  $ZnMgO:P$  films ;  $x=0.05$  is not sufficient. The generation of compensating deep acceptor states with Mg alloying could also explain this result. The doping of ZnO films with P and Mg generates deep level traps that suppress and/or prevent near bandedge emission. Rapid thermal annealing (RTA) also was performed in order to investigate possible activation of acceptor states in  $(Zn,Mg)O:P$  films. Annealing the  $Zn_{0.95}Mg_{0.05}O:P$  films at  $800\text{ }^{\circ}\text{C}$  in oxygen for 3 min resulted in a carrier type conversion from n-type to p-type. These films showed a hole carrier density on the order of  $1.6 \times 10^{16} /\text{cm}^3$ . This indicates that deep non-radiative centers in the films were generated with annealing.

### **8. 3 ZnO Based LEDs**

ZnO light emitting diodes were fabricated utilizing P-doped thin films grown by pulsed-laser deposition. The heterojunction diodes using  $ZnO:P/Zn_{0.9}Mg_{0.1}O/ZnO/Zn_{0.9}Mg_{0.1}O/ZnO:Ga$  layer showed diodes characteristics having  $\sim 2.2\text{ eV}$  turn-on voltage. The EL spectra shows the near bandedge emission with some deep level emission.

## LIST OF REFERENCES

1. D. M. Bagnall, Y. F. Chen, Z. Zhu, T. Yao, S. Koyama, M. Y. Shen, and T. Goto, *Appl. Phys. Lett.* **70**, 2230 (1997).
2. D. C. Look, *Mater. Sci. Eng. B* **80**, 381 (2001).
3. A. Ohtomo, M. Kawasaki, T. Koida, K. Masubuchi, and H. Koinuma, *Appl. Phys. Lett.* **72**, 2466 (1998).
4. C. W. Teng, J. F. Muth, U. Ozgur, M. J. Bergmann, H. O. Everitt, A. K. Sharma, C. Jin, and J. Narayan, *Appl. Phys. Lett.* **76**, 979 (2000).
5. T. Makino, Y. Segawa, M. Kawasaki, A. Ohtomo, R. Shiroki, K. Tamura, T. Yasuda, and H. Koinuma, *Appl. Phys. Lett.* **78**, 1237 (2001).
6. M. S. Han, J. H. Kim, T. S. Jeong, J. M. Park, C. J. Youn, J. H. Leem, and Y. R. Ryu, *J. Cryst. Growth* **303**, 506 (2007).
7. S. B. Zhang, S. H. Wei, and A. Zunger, *J. Appl. Phys.* **83**, 3192 (1998).
8. A. Tsukazaki, A. Ohtomo, T. Onuma, M. Ohtani, T. Makino, M. Sumiya, K. Ohtani, S. Chichibu, S. Fuke, Y. Segawa, H. Ohno, H. Koinuma, and M. Kawasaki, *Nat. Mater.* **4**, 42 (2005).
9. W. Liu, S. S. Gu, J. D. e, S. M. Zhu, S. M. Liu, X. Zhou, R. Zhang, Y. Shi, Y. D. Zheng, Y. Hang, and C. L. Zhang, *Appl. Phys. Lett.* **88**, 092101 (2006).
10. Y. Ryu, T. Lee, J. A. Lubguban, H. W. White, B. Kim, Y. Park, and C. Youn, *Appl. Phys. Lett.* **88**, 241108 (2006).
11. J.-H.Lim, C.-K.Kang, K.-K. Kim,I.-K. Park, D.-K. Hwang and S.-J.Park, *Adv. Mater.* **18**, 2720 (2006).
12. T. Yamamoto and H. K. Yoshida, *Physica B* **302**, 155 (2001).
13. D. R. Lide, *CRC Handbook of Chemistry and Physics*, 73<sup>rd</sup> Edition, CRC press, New York, (1992).
14. Y. Li, G. S. Tompa, S. Liang, C. Gorla, Y. Lu, and J. Doyle, *J. Vac. Sci. Technol. A* **15(3)**, 1063 (1997).
15. T. Yamamoto and H. K. Yoshida, *Jpn. J. Appl. Phys. Part 2* **38**, L166 (1999).
16. A. F. Kohan, G. Ceder, D. Morgan, and C. G. Van de Walle, *Phys. Rev. B* **61**, 15019 (2000).
17. C. G. Van de Walle, *Physica B* **308-310**, 899 (2001).

18. D. C. Look, J. W. Hemsley, and J. R. Sizelove, *Phys. Rev. Lett.* **82**, 2552 (1999).
19. C. G. Van de Walle, *Phys. Rev. Lett.* **85**, 1012 (2000).
20. D. M. Hofmann, A. Hofstaetter, F. Leiter, H. Zhou, F. Henecker, B. K. Meyer, S. B. Orlinskii, J. Schmidt, and P. G. baranov, *Phys. Rev. Lett.* **88**, 045504 (2002).
21. T. Minami, H. Sato, H. Nanto, and S. Takata, *Jpn. J. Appl. Phys. Part 2* **24**, L781 (1985).
22. Y. Sato and S. Sata, *Thin Solid Films* 281-282, 445 (1996).
23. H. J. Ko, Y. F. Chen, S. K. Hong, H. Wensch, T. Yao, and D. C. Look, *Appl. Phys. Lett.* **77**, 3761 (2000).
24. M. Miyazaki, S. Sato, K. Mitsui, and H. Nishimura, *J. Un-Cryst. Solids* **218**, 323 (1997).
25. S. Y. Myong, S. J. Baik, C. H. Lee, W. Y. Cho, and K. S. Lim, *Jpn. J. Appl. Phys. Part 2* **36**, L1078 (1997).
26. D. C. Look and B. Clafin, *Phys. Status Solidi B* **241**, 624 (2004).
27. S. B. Zhang, S.-H. Wei, and A. Zunger, *Phys. Rev. B* **63**, 075205 (2001).
28. C. H. Park, S. B. Zhang, and S. H. Wei, *Phys. Rev. B* **66**, 073202 (2002).
29. D. C. Look, R. L. Jones, J. R. Sizelove, N. Y. Garces, N. C. Giles, and L. E. Halliburton, *Phys. Status Solidi A* **195**, 171 (2004).
30. U. Ozgur, Ya. I. Alivov, C. Liu, A. Teke, M. A. Reshchikov, S. Doonan, V. Avrutin, S. J. Cho, H. Morkoc, *J. Appl. Phys.* **98** 041301 (2005).
31. E. C. Lee and K. J. Chang, *Phys. Rev. B* **70**, 115210 (2004).
32. X. Li, Y. Yan, T. A. Gessert, C. L. Perkins, D. Young, C. DeHart, M. young, and T. J. Coutts, *J. Vac. Sci. Technol. A* **21**, 1342 (2003).
33. H. Matsui, H. Saeki, T. Kawai, H. Tabata, and B. Mizobuchi, *J. Appl. Phys.* **95**, 5882 (2004).
34. W. Z. Xu, Z. Z. Ye, T. Zhou, B. H. Zhao, L. P. Zhu, and J. Y. Huang, *J. Cryst. Growth* **265**, 133 (2004).
35. Z. Z. Ye, J. G. Lu, H. H. Chen, Z. Zhang, L. Wang, B. H. Zhao, and J. Y. Huang, *J. Cryst. Growth* **253**, 258 (2003).
36. Y. Yan, S. B. Zhang, and S. T. Pantelides, *Phys. Rev. Lett.* **86**, 5723 (2001).

37. J. Wang, G. Du, B. Zhao, X. Yang, Y. Zhang, Y. Ma, D. Liu, Y. Chang, H. Wang, H. Yang, and S. Yang, *J. Cryst. Growth* **255**, 293 (2003).
38. Y. I. Alivov, E. V. Kalinina, A. E. Cherenkov, D. C. Look, B. M. Ataev, A. K. Omaev, M. V. Chukichev, and D. M. Bagnall, *Appl. Phys. Lett.* **83**, 4719 (2003).
39. A. Kobayashi, O. F. Sankey, and J. D. Dow, *Phys. Rev.* **28**, 949 (1983).
40. T. Yamamoto, *Thin Solid Films* **420-421**, 100 (2002).
41. M. Joseph, H. Tabata, and T. Kawai, *Jpn. J. Appl. Phys., Part 2* **38**, L1205 (1999).
42. N. Nakahara, H. Takasu, P. Fons, A. Yamada, K. Iwats, K. Matsubara, R. Hunger and S. Ni ki, *Appl. Phys. Lett.* **79**, 4139 (2001).
43. A. Tsukazaki, H. Saito, K. Tamura, M. Ohtani, H. Koinuma, M. Sumiya, S. Fuke, T. Fukumura and M. Kawasaki, *Appl. Phys. Lett.* **81**, 235 (2002).
44. X. L. Guo, H. Tabata, and T. Kawai, *J. Cryst. Growth* **223**, 135 (2001).
45. D. C. Look, D. C. Reynolds, C. W. Litton, R. L. Jones, D. B. Eason, and G. Cantwell, *Appl. Phys. Lett.* **81**, 1830 (2002).
46. K. Minegishi, Y. Koiwai, Y. Kikuchi, K. Yano, M. Kasuga, and A. Shimizu, *Jpn. J. Appl. Phys. Part 2* **36**, L1453 (1997).
47. A. B. M. A. Ashrafi, I. Suemune, H. Kumano, and S. Tanaka, *Jpn. J. Appl. Phys. Part 2* **41**, L1281 (2002).
48. J. Lu, Y. Zhang, Z. Ye, I. Wang, B. Zhao, and J. Huang, *Mater. Lett.* **57**, 3311 (2003).
49. X.-L. Guo, H. Tabata, and T. Kawai, *J. Cryst. Growth* **237-239**, 544 (2002).
50. X. Li, Y. Yan, T. A. Gessert, C. L. Perkins, D. Young, C. DeHart, M. Young, and T. J. Coutts, *J. Vac. Sci. Technol. A* **21**, 1342 (2003).
51. X. Li, Y. Yan, T. A. Gessert, C. DeHart, C. L. Perkins, D. Young, and T. J. Coutts, *Electrochem. Solid-State Lett.* **6**, C56 (2003).
52. C.-C. Lin, S.-Y. Chen, S.-Y. Cheng, and H.-Y. Lee, *Appl. Phys. Lett.* **84**, 5040 (2004).
53. K. Nakahara, H. Takasu, P. Fons, A. Yamada, K. Iwata, K. Matsubara, R. Hunger, and S. Ni ki, *J. Cryst. Growth* **237-239** 503 (2002).
54. T. Ohshima, T. Ikegami, K. Ebihara, J. Asmessen, and R. Thareja, *Thin Solid Films* **435**, 49 (2003).

55. M. Sumiya, A. Tsukazaki, S. Fuke, A. Ohtomo, H. Koinuma, and M. Kawasaki, *Appl. Surf. Sci.* **223**, 206 (2004).
56. Y. I. Alivov, D. C. Look, B. M. Ataev, M. V. Chukichev, V. V. Mamedov, V. I. Zinenko, Y. A. Agafonov, and A. N. Pustovit, *Solid-State Electron* **48**, 2343 (2004).
57. J. M. Bian, X. M. Li, X. D. Gao, W. D. Yu, and L. D. Chen, *Appl. Phys. Lett.* **84**, 541 (2004).
58. Z.-Z. Ye, Z.-G. Fei, J.-G. Lu, Z.-H. Zhang, L.-P. Zhu, B.-H. Zhao, and J.-Y. Huang, *J. Cryst. Growth* **265**, 127 (2004).
59. K. K. Kim, H. S. Kim, D. K. Hwang, J. H. Lim, and S. J. Park, *Appl. Phys. Lett.* **83**, 63 (2003).
60. V. Vaithianathan, B. T. Lee, and S. S. Kima, *J. Appl. Phys.* **98**, 043519 (2005).
61. T. Aoki, Y. Hatanaka, and D. C. Look, *Appl. Phys. Lett.* **76**, 3257 (2000).
62. S. Y. Lee, E. S. Shim, H. S. Kang, S. S. Pang, and J. S. Kang, *Thin Solid Films* **473**, 31 (2005).
63. S. Limpijumnong, S. B. Zhang, S.-H. Wei, and C. H. Park, *Phys. Rev. Lett.* **92**, 155504 (2004).
64. W. J. Lee, J. G. Kang, and K. J. Chang, *Phys. Rev. B* **73**, 024117 (2006).
65. Y. R. Ryu, T. S. Lee and H. W. White, *Appl. Phys. Lett.* **83**, 87 (2003).
66. Y. R. Ryu, J. A. Lubguban, T. S. Lee, H. W. White, Y. S. Park, and C. J. Youn, *Appl. Phys. Lett.* **87**, 153504 (2005).
67. G. Braunstein, A. Muraviev, H. Saxena, N. Dhere, V. Richter, and R. Kalish, *Appl. Phys. Lett.* **87**, 192103 (2005).
68. F. X. Xiu, Z. Yang, L. J. Mandalapu, D. T. Zhao, J. L. Liua, and W. P. Beyermann, *Appl. Phys. Lett.* **87**, 152101 (2005).
69. Y. Yan, M. M. Al-Jassim, and S.-H. Wei, *Appl. Phys. Lett.* **89**, 181912 (2006).
70. H. S. Kang, B. D. Ahn, J. H. Kim, G. H. Kim, S. H. Lim, H. W. Chang, and S. Y. Lee, *Appl. Phys. Lett.* **88**, 202108 (2006).
71. A. Y. Polyakov, N. B. Smirnov, A.V. Govorkov, M. Shin, M. Skowronski, and D. W. Greve, *J. Appl. Phys.* **84**, 870 (1998).

72. A. Y. Polyakov, N. B. Smirnov, A.V. Govorkov, M. G. Mill'vidskii, J. M. Redwing, M. Shin, M. Skowronski, D. W. Greve, and R. G. Wilson, *Solid-State Electron.* **42**, 627 (1998).
73. A. Dissanayake, M. Elahi, H. X. Jiang, and J. Y. Lin, *Phys. Rev. B* **45**, 13996 (1992)
74. J. Y. Lin, A. Dissanayake, G. Brown, and H. X. Jiang, *Phys. Rev. B* **42** 5855 (1990)
75. D. H. Zhang, *J. Phys. D* **28**, 1273 (1995).
76. V. Tudose, P. Horvath, M. Sucheai, S. Christoulakis, Kitsopoulos, and G. Kiriakidis, *Appl. Phys. A* **89** 57 (2007).
77. P. Sharma, A. Mansingh, K. Sreenivas, *Appl. Phys. Lett.* **80**, 553 (2002).
78. P. Sharma, K. Sreenivas, and K. V. Rao, *J. Appl. Phys.* **93**, 3963 (2003).
79. Y. Takahashi, M. Kanamori, A. Kondoh, H. Minoura, and Y. Ohya, *Jpn. J. Appl. Phys. Part 1* **33**, 6611 (1994).
80. S. A. Studenikin, N. Golego, and M. Cocivera, *J. Appl. Phys.* **87**, 2413 (2000).
81. S. Mridha and D. Basak, *Chem. Phys. Lett.* **427**, 62 (2006).
82. K. Moazzami, T. E. Murphy, J. D. Phillips, M. C.-K. Cheung, and A. N. Cartwright, *Semicond. Sci. Technol.* **21**, 717 (2006).
83. J. Reemts and A. Kittel, *J. Appl. Phys.* **101**, 013709 (2007).
84. S. Lany and A. Zunger, *Phys. Rev. B* **72**, 035215 (2005).
85. M. Salis, A. Anedda, F. Quarati, A. J. Blue, and W. Cunningham, *J. Appl. Phys.* **97**, 033709 (2005).
86. D. Seghier, H. P. Gislason, *Physica B* **401**, 404 (2007).
87. B. Claflin, D. C. Look, S. J. Park, and G. Cantwell, *J. Cryst. Growth* **287**, 16 (2006).
88. A. Y. Polyakov, N. B. Smirnov, A. V. Govorkov, A. I. Belogorokhov, A. Osinsky, J. W. Dong, and S. J. Pearton, *Appl. Phys. Lett.* **90**, 132103 (2007).
89. Y. J. Zeng, Z. Z. Ye, Y. F. Lu, J. G. Lu, W. Z. Xu, L. P. Zhu, B. H. Zhao, and Y. Che, *Chem. Phys. Lett.* **441** 115 (2007).
90. Z. Yan, Z. Tang, W. L. Liu, Q. Wan, F. M. Zhang, and S. L. Feng, *Thin Solid Films* **492**, 203 (2005).

91. H. L. Porter, A. L. Cai, J. F. Muth, and J. Narayan, *Appl. Phys. Lett.* **86**, 211918 (2005).
92. Y. W. Heo, K. Ip, S. J. Pearton, and D. P. Norton, *Phys. Stat. Sol. (a)*, **201** 1500 (2004).
93. A. Y. Polyakov, N. B. Smirnov, A. V. Govorkov, E. A. Kozhukhova, A. I. Belogorokhov, A. V. Markov, H. S. Kim, D. P. Norton, and S. J. Pearton, *J. Electrochem. Soc.* **154**, H825 (2007).
94. R. Ghosh and D. Basak, *J. Appl. Phys.* **101**, 113111 (2007).
95. C. H. Seager and S. M. Myers, *J. Appl. Phys.* **94**, 2888 (2003).
96. E. V. Lavrov and J. Weber, *Phys. Rev. B* **73**, 035208 (2006).
97. D. C. Look, H. L. Mosbacker, Y. M. Strzhemechny, and L. J. Brillson **38**, 406 (2005).
98. M. S. Oh, D. K. Hwang, J. H. Lim, Y. S. Choi, and S. J. Park, *Appl. Phys. Lett.* **91** 212102 (2007).
99. Y. L. Wang, F. Ren, H. S. Kim, S. J. Pearton, and D. P. Norton, *Appl. Phys. Lett.* **90**, 092116 (2007).
100. Y. L. Wang, H. S. Kim, D. P. Norton, S. J. Pearton, and F. Ren, , *J. Electrochem. Soc.* **11**, H88 (2008).
101. K. Ip, M. E. Overberg, Y. W. Heo, D. P. Norton, S. J. Pearton, C. E. Stutz, B. Luo, F. Ren, D. C. Look, and J. M. Zavada, *Appl. Phys. Lett.* **82**, 385 (2003)
102. K. Ip, M. E. Overberg, Y. W. Heo, D. P. Norton, S. J. Pearton, S. O. Kucheyev, C. Jagadish, J. S. Williams, R. G. Wilson, J. M. Zavada, *Appl. Phys. Lett.* **81**, 3996 (2002).
103. K. C. Hui, H. C. Ong, P. F. Lee, and J. Y. Dai, *Appl. Phys. Lett.* **86**, 152116 (2005).
104. O. Schmidt, A. Geis, P. Kiesel, C. G. Van de Walle, N. M. Johnson, A. Bakin, A. Waag, G. H. Dohler, *Superlatt. Microstr.* **39**, 8 (2006).
105. W. Liu, S. Gu, S. Zhu, J. Ye, F. Qin, S. Liu, X. Zhou, L. Hu, R. Zhang, Y. Shi, and Y. Zheng , *J. Crystal Growth*, **277**, 416 (2005).
106. K. Koike, G. Takada, K. Fujimoto, S. Sasa, M. Inoue, and M. Yano, *Physica E*, **32**, 191 (2006).
107. J. Bian, W. Liu, J. Sun, and H. Liang, *J. Mater. Processing Technol.* **184**, 451 (2007).
108. Y.M. Ye, Z.Z. Ye, L.L. Chen, B.H. Zhao, and L.P. Zhu, *Appl. Surf. Sci.* **253**, 2345 (2006).

109. Y.J. Li, Y.W. Heo, Y. Kwon, K. Ip, S.J. Pearton, and D.P. Norton, *Appl. Phys. Lett.* **87**, 072101 (2005).
110. X. Pan, J. Li, Y. Zeng, X. Gu, L. Zhu, B. Zhao, and Y. Che, *Appl. Surf. Sci.* **253**, 6060 (2007).
111. O. Vigil, L. Vaillant, F. Cruz, G. Santana, A. Morales-Acevedo, and G. Contreras-Puente, *Thin Solid Films* **361-362**, 53 (2000).
112. H. Ohta, K. Kawamura, M. Orita, M. Hirano, N. Sarukura, and H. Hosono, *Appl. Phys. Lett.* **77**, 475 (2000).
113. Y. I. Alivov, J. E. V. Nostrand, D. C. Look, M. V. Chukichev, and B. M. Ataev, *Appl. Phys. Lett.* **83**, 2943 (2003).
114. A. Osinsky, J. W. Dong, M. Z. Kauser, B. Hertog, A. M. Dabiran, P. P. Chow, S. J. Pearton, O. Lopatiuk, and L. Chernyak, *Appl. Phys. Lett.* **85**, 4272 (2004).
115. X. L. Guo, J. H. Choi, H. Tabata, and T. Kawai, *Jpn. J. Appl. Phys., Part 2* **40**, L117 (2001).
116. J. G. Lu, Z. Z. Ye, G. D. Yuan, Y. J. Zeng, F. Zhuge, L. P. Zhu, B. H. Zhao, and S. B. Zhang, *Appl. Phys. Lett.* **89**, 053501 (2006).
117. T. Aoki, Y. Shimizu, A. Miyake, A. Nakamura, Y. Nakanishi, and Y. Hatanaka, *Phys. Status Solidi B* **229**, 911 (2002).
118. S. Jang, J. J. Chen, B. S. Kang, F. Ren, D. P. Norton, S. J. Pearton, J. Lopata, and W. S. Hoatson, *Appl. Phys. Lett.* **87**, 222113 (2005).
119. M. Fujita, N. Kawamoto, T. Tatsumi, K. Yamagishi, and Y. Horikoshi, *Jpn. J. Appl. Phys.* **42**, 67 (2001).
120. N. Izyumskaya, V. Avrutin, W. Schoch, A. El-Shaer, F. Reuss, Th. Gruber, and A. Waag, *J. Cryst. Growth* **269**, 356 (2004).
121. K. Sakurai, D. Iwata, Sz. Fujita, Sg. Fujita, *Jpn. J. Appl. Phys.* **38**, 2606 (1999).
122. A. El-Shaer, A. Bakin, A.C. Mofor, J. Blasing, A. Krost, J. Stoimenos, B. Pecz, M. Kree, M. Heuken, and A. Waag, *Phys. Stat. Sol. (b)* **243**, 768 (2006).
123. J. Dai, H. Su, L. Wang, Y. Pu, W. Fang, F. Jiang, *J. Cryst. Growth* **290**, 426 (2006).
124. S. H. Kim, C. S. Hwang, S. Park, S. J. Yun, *Thin Solid Films* **478**, 103 (2005).

125. J. Ye, S. Gu, S. Zhu, T. Chen, L. Hu, F. Qin, R. Zhang, Y. Shi, Y. Zhen, *J. Cryst. Growth* **243**, 151 (2002).
126. L. Wang, Y. Pu, W. Fang, J. Dai, C. Zheng, C. Mo, C. Xiong, and F. Jiang, *Thin Solid Films* **491**, 323 (2005).
127. B. X. Lin, Z. X. Fu, Y. B. Jia, and G. H. Liao, *J. Electrochem. Soc.* **148**, G110 (2001).
128. W. S. Shi, O. Agyeman, and C. N. Xu, *J. Appl. Phys.* **91**, 5640 (2002).
129. X. Liu, X. H. Wu, H. Cao, and R. P. Chang, *J. Appl. Phys.* **95**, 3141 (2004).
130. E. C. Lee, Y. S. Kim, Y. G. Jin, and K. J. Chang, *Phys. Rev. B*, **64**, 085120 (2001).
131. F. A. Kröger, *The Chemistry of Imperfect Crystals*, North-Holland publishing Co., Amsterdam, 1964.
132. A.F. Kohan, G. Ceder, D. Morgan, and C. G. Van de Walle, *Phys. Rev. B* **61**, 15019 (2000).
133. D. C. Look, G. C. Farlow, P. Reunchchan, S. Limpijumnong, S. B. Zhang, and K. Nordlund, *Phys. Rev. Lett.* **95**, 225502 (2005).
134. A. Janotti, C. G. Van de Walle, *J. Cryst. Growth* **287**, 58 (2006).
135. F. Oba, S. R. Nishitani, S. Isotani, H. Adachi, I. Tanaka, *J. Appl. Phys.* **90**, 824 (2001).
136. Y. W. Heo, D. P. Norton, S. J. Pearton, *J. Appl. Phys.* **98**, 073502 (2005).
137. S. A. Studenikin, N. Golego, and M. Cocivera, *J. Appl. Phys.* **84**, 2287 (1998).
138. X. L. Wu, G. G. Siu, C.L. Fu, and H. C. Ong, *Appl. Phys. Lett.* **78**, 2285 (2001).
139. M. Koyano, P. Quocbao, L. T. Thanhbinh, L. Hongha, N. Ngoclong, and S. Katayama, *Phys. Stat. Sol. (a)* **193**, 125 (2002).
140. A. Y. Polyakov, N. B. Smirnov, A. V. Govorkov, K. Ip, M. E. Overberg, Y. W. Heo, D. P. Norton, S. J. Pearton, B. Luo, F. Ren, and J. M. Zavada, *J. Appl. Phys.* **94**, 400 (2003).
141. Y. W. Heo, S. J. Park, K. Ip, S. J. Pearton, and D. P. Norton, *Appl. Phys. Lett.* **83**, 1128 (2003).
142. H. S. Kim, J.-M. Erie, S. J. Pearton, D. P. Norton, and F. Ren (submitted)
143. A. Y. Polyakov, N. B. Smirnov, E. A. Kozhukhova, V. I. Vdovin, K. Ip, Y. W. Heo, D. P. Norton, and S. J. Pearton, *Appl. Phys. Lett.* **83**, 1575 (2003).

144. H. S. Kang, J. S. Kang, J. W. Kim, and S. Y. Lee, *J. Appl. Phys* **95**, 1246 (2004).
145. A. N. Gruzintsev and E. E. Yakimov, *Inorganic Materials* **41**, 828 (2005).
146. K. Tamura, A. Ohtomo, K. Saikusa, Y. Osaka, T. Makino, Y. Segawa, M. Sumiya, S. Fuke, H. Koinuma, and M. Kawasaki, *J. Cryst. Growth* **214**, 59 (2000).
147. Z. Q. Zeng, Y. Z. Liu, H. T. Yuan, Z. X. Mei, X. L. Du, J. F. Jia, Q. K. Xue and Z. Zhang, *Appl. Phys. Lett.* **90**, 081911 (2003).
148. J.-Y. Oh, J.-H. Lim, D.-K. Hwang, H.-S. Kim, R. Navamathavan, K.-K. Kim, and S.-J. Park, *J. Electrochem. Soc.* **151**, G623 (2004).
149. K. Miyamoto, M. Sano, H. Kato, and T. Yao, *J. Cryst. Growth* **265**, 34 (2004).
150. A. Tsukazaki, A. Ohtomo, S. Yoshida, M. Kawasaki, C. H. Chia, T. Makino, Y. Segawa, T. Koida, S. F. Chichibu, and H. Koinuma, *Appl. Phys. Lett.* **83** 2784 (2003).
151. A. Tsukazaki, A. Ohtomo, and M. Kawasaki, *Appl. Phys. Lett.* **88** 152106 (2006).
152. J. Dai, H. Liu, W. Fang, L. Wang, Y. Pu, Y. Chen, and F. Jiang, *J. Cryst. Growth* **283**, 93 (2005).
153. L. Wang, Y. Pu, W. Fang, J. Dai, Y. Chen, C. Mo, and F. Jiang, *J. Cryst. Growth* **283**, 87 (2005).
154. J. Han, T. B. Ng, R. M. Biefeld, M. H. Crawford, and D. M. Follstaedt, *Appl. Phys. Lett.* **71**, 3114 (1997).
155. V. Craciun, J. Perriere, N. Bassim, R. K. Singh, D. Craciun, and J. Spear, *Appl. Phys. A* **69**, S531 (1999).
156. Y. Chen, N.T. Tuan, Y. Segawa, H.-H. Ko, S.-K. H, and T. Yao, *Appl. Phys. Lett.* **78**, 1469 (2001).
157. S.-J. An, W. I. Park, G.-C. Yi, and S. Cho, *Appl. Phys. A* **74**, 509 (2002).

158. D.C. Look, B. Claflin, Y.I. Alivov, and S.J. Park, *Physica Status Solidi A* **201**, 2203 (2004).
159. Z. P. Wei, Y. M. Lu, D. Z. Shen, Z. Z. Zhang, B. Yao, B. H. Li, J. Y. Zhang, D. X. Zhao, X. W. Fan, and Z. K. Tang, *Appl. Phys. Lett.* **90**, 042113 (2007).
160. M. Pan, J. Nause, V. Rengarajan, R. Rondon, E. H. Park, and I. T. Ferguson, *J. Electronic Mater.* **36**, 457 (2007).
161. Y. Miao, Z.Z. Ye , W.Z. Xu, F.G. Chen, X.C. Zhou, B.H. Zhao, L.P. Zhu, and J.G. Lu, *Appl. Surf. Sci.* **252**, 7953 (2006).
162. K. Ip, Y. W. Heo, D. P. Norton, S. J. Pearton, J. R. LaRoche, and F. Ren, *Applied Phys. Lett.* **85**, 1169 (2004).
163. C.-H. Choi, and S.-Y. Kim, *J. Cryst. Growth*, **283**, 170 (2005).
164. X. Yang, J. Zhang, Z. Bi, Y. He, Q. Xu, H. Wang, W. Zhang, and X. Hou, *J. Cryst. Growth*, **284**, 123 (2005).
165. Y. W. Heo, K. Ip, S. J. Park, S. J. Pearton, D. P. Norton, *Applied Physics A* 78, 53 (2004).
166. Z. G. Yu, H. Gong, and P. Wu, *Appl. Phys. Lett.* **86**, 212105 (2005).
167. D.-K. Hwang, M.-S. Oh, J.-H. Lim, C.-G. Kang and S.-J. Park, *Appl. Phys. Lett.* **90**, 021106 (2007).
168. Y. Kwon, Y. Li, Y. W. Heo, M. Jones, P. H. Holloway, D. P. Norton, Z.V. Park and S. Li, *Appl. Phys. Lett.* **84**, 2685 (2004).
169. Y.W. Heo, L.C. Tien, Y. Kwon, D.P. Norton, S.J. Pearton, B.S. Kang, and F. Ren, *Appl. Phys. Lett.* **85**, 2274 (2004).
170. Y.W. Heo, L.C. Tien, D.P. Norton, B.S. Kang, F. Ren, B.P. Gila, and S.J. Pearton, *Appl. Phys. Lett.* **85**, 2002 (2004)
171. H. Yang, Y. Li, D. P. Norton, S. J. Pearton, S. Jung, F. Ren, and L. A. Boatner, *Appl. Phys. Lett.* **86**, 172103 (2005).
172. J. W. Dong, A. Osinsky, B. Hertog, A. M. Dabiran, P. P. Chow, Y. W. Heo, D. P. Norton, and S. J. Pearton, *Journal of Electronic Materials* **34**, 416 (2005).
173. H. S. Yang, S. Y. Han, Y. W. Heo, K. H. Baik, D. P. Norton, S. J. Pearton, F. Ren, A. Osinsky, J. W. Dong, B. Hertog, A. M. Dabiran, P. P. Chow, L. Chernyak, T. Steiner, C. J. Kao, G. C. Chi, *Japanese Journal of Applied Physics Part 1-Regular Papers Brief Communications & Review Papers* **44**, 7296 (2005).

174. Z. Z. Ye, J. G. Lu, Y. Z. Zhang, Y. J. Zeng, L. L. Chen, F. Zhuge, G. D. Yuan, H. P. He, L. P. Zhu, J. Y. Huang and B. H. Zhao, *Appl. Phys. Lett.* **91**, 113503 (2007).
175. K. Ip, Y. W. Heo, K. H. Baik, D. P. Norton, S. J. Pearton, and F. Ren, *Appl. Phys. Lett.* **84**, 544 (2004).
176. S. Kim, B. S. Kang, F. Ren, Y. W. Heo, K. Ip, D. P. Norton, and S. J. Pearton, *Appl. Phys. Lett.* **84**, 1904 (2004).
177. K. Ip, K. H. Baik, M. E. Overberg, E. S. Lambers, Y. W. Heo, D. P. Norton, S. J. Pearton, F. Ren, and J. M. Zavada, *Appl. Phys. Lett.* **81**, 3546 (2002).

## BIOGRAPHICAL SKETCH

Hyun-Sik Kim was born on March 14, 1978, in Seoul, South Korea. After graduating from high school in 1996, he attended Hanyang University and earned a bachelor's degree in materials science and engineering in February 2002. He then began to pursue a master degree in Gwangju Institute of Science and Technology. He received his master's degree in the summer of 2004. He conducted his research for master's degree on the growth of ZnO materials for optoelectronic applications under the supervision of Dr. Seong-Ju Park.

In August 2004, he enrolled at the University of Florida in the Department of Materials Science and Engineering to pursue Ph.D under the advisement of Dr. David P. Norton. His main research involved growth and characterization of ZnO thin films for light emitting diodes. He is co-author of more than 25 journal and conference papers.